

SMIP09

SMIP09 SEMINAR ON UTILIZATION OF STRONG-MOTION DATA

San Francisco, California
November 19, 2009

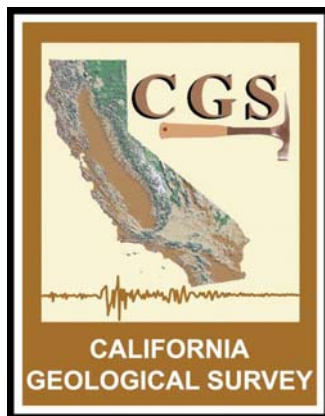
PROCEEDINGS

Sponsored by

California Strong Motion Instrumentation Program
California Geological Survey
California Department of Conservation

Co-Sponsors

California Seismic Safety Commission
California Emergency Management Agency
California Department of Transportation
Office of Statewide Health Planning and Development



The California Strong Motion Instrumentation Program (CSMIP), a program within the California Geological Survey (CGS) of the California Department of Conservation, records the strong shaking of the ground and structures during earthquakes for analysis and utilization by the engineering and seismology communities through a statewide network of strong motion instruments (www.conservation.ca.gov/CGS/smip). CSMIP is advised by the Strong Motion Instrumentation Advisory Committee (SMIAC), a committee of the California Seismic Safety Commission. Major program funding is provided by an assessment on construction costs for building permits issued by cities and counties in California, with additional funding from the California Emergency Management Office (CalEMA, formerly California Office of Emergency Services), the California Department of Transportation (Caltrans) and the Office of Statewide Health Planning and Development (OSHPD).

In July 2001, the California Office of Emergency Services (OES) began funding for the California Integrated Seismic Network (CISN), a newly formed consortium of institutions engaged in statewide earthquake monitoring that grew out of TriNet, funded by FEMA, and includes CGS, USGS, Caltech and UC Berkeley. The goals are to record and rapidly communicate ground shaking information in California, and to analyze the data for the improvement of seismic codes and standards (www.cisn.org). CISN produces ShakeMaps of ground shaking, based on shaking recorded by stations in the network, within minutes following an earthquake. The ShakeMap identifies areas of greatest ground shaking for use by OES and other emergency response agencies in the event of a damaging earthquake.

The Center for Engineering Strong Motion Data (CESMD) is operated by the CSMIP Program of the CGS in cooperation with the National Strong-Motion Project (NSMP) and the Advanced National Seismic System (ANSS) of the U.S. Geological Survey (USGS). The CESMD builds on and incorporates the CISN Engineering Data Center and will continue to serve the California region while expanding to serve other ANSS regions. The Data Center provides strong-motion data rapidly after a significant earthquake in the United States. Users also have direct access to data from previous earthquakes and detailed information about the instrumented structures and sites. The Data Center is co-hosted by CGS and USGS at www.strongmotioncenter.org

DISCLAIMER

Neither the sponsoring nor supporting agencies assume responsibility for the accuracy of the information presented in this report or for the opinions expressed herein. The material presented in this publication should not be used or relied upon for any specific application without competent examination and verification of its accuracy, suitability, and applicability by qualified professionals. Users of information from this publication assume all liability arising from such use.

SMIP09

SMIP09 SEMINAR ON UTILIZATION OF STRONG-MOTION DATA

San Francisco, California
November 19, 2009

PROCEEDINGS

Edited by

Moh Huang

Sponsored by

California Strong Motion Instrumentation Program
California Geological Survey
California Department of Conservation

Co-Sponsors

California Seismic Safety Commission
California Emergency Management Agency
California Department of Transportation
Office of Statewide Health Planning and Development

PREFACE

The California Strong Motion Instrumentation Program (CSMIP) in the California Geological Survey of the California Department of Conservation established a Data Interpretation Project in 1989. Each year CSMIP Program funds several data interpretation contracts for the analysis and utilization of strong-motion data. The primary objectives of the Data Interpretation Project are to further the understanding of strong ground shaking and the response of structures, and to increase the utilization of strong-motion data in improving post-earthquake response, seismic code provisions and design practices.

As part of the Data Interpretation Project, CSMIP holds annual seminars to transfer recent research findings on strong-motion data to practicing seismic design professionals, earth scientists and post-earthquake response personnel. The purpose of the annual seminar is to provide information that will be useful immediately in seismic design practice and post-earthquake response, and in the longer term, useful in the improvement of seismic design codes and practices. Proceedings and individual papers for each of the previous annual seminars are available in PDF format at <http://www.consrv.ca.gov/CGS/smip/proceedings.htm> The SMIP09 Seminar is the twentieth in this series of annual seminars.

The SMIP09 Seminar is divided into two sessions in the morning and two sessions in the afternoon. The sessions in the morning include three presentations on CSMIP-funded projects. These include analysis of the Turkey Flat ground motion prediction experiment and two presentations on utilizing recorded response data from buildings. The afternoon sessions include an invited presentation by Chris Poland on observation of structural performance during the recent earthquake in Italy, presentations by two investigators of CSMIP-funded projects on utilization of recorded data from highway bridges and design ground motions for tall buildings in the Tall Building Initiative, and an update and new features of the Center for Engineering Strong Motion Data.

Moh J. Huang, Ph.D., P.E.
CSMIP Data Interpretation Project Manager

**Appreciation to Members of the
Strong Motion Instrumentation Advisory Committee**

Main Committee

Chris Poland, Chair, Degenkolb Engineers
Arul Arulmoli, Seismic Safety Commission, Earth Mechanics, Inc.
Norman Abrahamson, Pacific Gas & Electric Company
Anil Chopra, UC Berkeley
Bruce Clark, Leighton & Associates
Martin Eskijian, California State Lands Commission
Wilfred Iwan, California Institute of Technology
Michael Keever/Paul Chung, Caltrans
Farzad Naeim, John A. Martin & Associates
Maurice Power, AMEC Geomatrix
Daniel Shapiro, SOHA Engineers
Robert Anderson (ex-officio), Seismic Safety Commission

Ground Response Subcommittee

Maurice Power, Chair, AMEC Geomatrix
Abbas Abghari, Caltrans
Yousef Bozorgnia, PEER
Brian Chiou, Caltrans
Marshall Lew, MACTEC Engineering & Consulting
Geoffrey Martin, Univ. of Southern California
Ben Tsai, Pacific Gas & Electric Company

Buildings Subcommittee

Farzad Naeim, Chair, John A. Martin & Associates
Lucie Fougner, Degenkolb Engineers
Kenneth Honda, URS Corporation
Donald Jephcott, Structural Engineer
David Leung, City of San Francisco
Bret Lizundia, Rutherford & Chekene
Eduardo Miranda, Stanford University
John Robb, Structural Engineer
Daniel Shapiro, SOHA Engineers
Chris Tokas, Office of Statewide Health Planning and Development
Chia-Ming Uang, UC San Diego

Lifelines Subcommittee

Martin Eskijian, Chair, California State Lands Commission
David Gutierrez, DWR Division of Safety of Dams
Michael Keever/Paul Chung, Caltrans
Stuart Nishenko, Pacific Gas & Electric Company
Vern Persson, DWR Division of Safety of Dams (retired)

Data Utilization Subcommittee

Wilfred Iwan, Chair, California Institute of Technology
Representatives from each Subcommittee

TABLE OF CONTENTS

Seminar Program v

Analysis of Turkey Flat Ground Motion Prediction Experiment – Lessons Learned and Implications for Practice 1
Steven Kramer

Schemes for Reconstructing the Seismic Response of Instrumented Buildings 23
Dionisio Bernal and Arash Nasser

Seismic Analysis of Buildings to Recorded Motions: Modeling and Software Challenges 39
Rakesh Goel and Karen Nishimoto

Observation of Structural Performance near Strong-Motion Stations during the Italy L’Aquila Earthquake..... 61
Chris Poland

Utilization of Strong-Motion Data for Assessment of Structural Integrity in Instrumented Highway Bridges 65
Virginia Mosquera, Andrew Smyth and Raimondo Betti

Comparison of Recorded and Simulated Ground Motions for Tall Buildings 85
Jonathan Stewart, Lisa Star and Robert Graves

Update and New Features of the Center for Engineering Strong Motion Data (CESMD) 89
Hamid Haddadi, Christopher Stephen, Anthony Shakal, Moh Huang,
David Oppenheimer, William Savage, William Leith and John Parrish

**SMIP09 SEMINAR ON
UTILIZATION OF STRONG-MOTION DATA**

November 19, 2009

Hiram Johnson State Building
455 Golden Gate Ave., San Francisco, California

PROGRAM

8:00 am **REGISTRATION**

9:15 am **WELCOMING REMARKS**

Chris Poland, Strong Motion Instrumentation Advisory Committee (SMIAC)
John Parrish, State Geologist, California Geological Survey

INTRODUCTION

Anthony Shakal, Manager, California Strong Motion Instrumentation Program
Moh Huang, California Strong Motion Instrumentation Program

Session I

Moderator: *Maurice Power*, AMEC Geomatrix and SMIAC

9:30 am **Analysis of Turkey Flat Ground Motion Prediction Experiment – Lessons Learned and Implications for Practice**

Steven Kramer, University of Washington, Seattle

10:30 am Break

Session II

Moderator: *Farzad Naeim*, John A. Martin & Associates and SMIAC

11:00 am **Schemes for Reconstructing the Seismic Response of Instrumented Buildings**

Dionisio Bernal and Arash Nasser, Northeastern University, Boston

11:30 am **Seismic Analysis of Buildings to Recorded Motions: Modeling and Software Challenges**

Rakesh Goel and Karen Nishimoto, California State University, San Luis Obispo

12:00 pm **Lunch**

Box lunch will be provided

Session III

Moderator: *Martin Eskijian*, California State Lands Commission and SMIAC

1:00 pm **Observation of Structural Performance near Strong-Motion Stations during the Italy L'Aquila Earthquake**

Chris Poland, Degenkolb Engineers, San Francisco

1:30 pm **Utilization of Strong-Motion Data for Assessment of Structural Integrity in Instrumented Highway Bridges**

Virginia Mosquera, Andrew Smyth and *Raimondo Betti*, Columbia University, New York

2:00 pm Break

Session IV

Moderator: *Wilfred Iwan*, Caltech and SMIAC

2:30 pm **Tall Building Initiative: Comparison of Recorded and Simulated Ground Motions for Tall Buildings**

Jonathan Stewart, Lisa Star, and Robert Graves, UC Los Angeles and URS Corporation, Pasadena

3:00 pm **Update and New Features of the Center for Engineering Strong Motion Data (CESMD)**

Hamid Haddadi, Christopher Stephens, Anthony Shakal, Moh Huang, David Oppenheimer, William Savage, William Leith and John Parrish, CGS and USGS

3:30 pm **Adjourn**

**ANALYSIS OF TURKEY FLAT GROUND MOTION PREDICTION EXPERIMENT –
LESSONS LEARNED AND IMPLICATIONS FOR PRACTICE**

Steven L. Kramer

Department of Civil and Environmental Engineering
University of Washington, Seattle, Washington

Abstract

This paper describes an investigation of the ground motions recorded at the Turkey Flat test site, and of the predictions of those motions in the blind prediction symposium that took place in 2006. The two-phase prediction experiment attracted numerous participants using several approaches to ground motion modeling and site data interpretation. The results of the Phase 1 predictions showed strong consistency in the predicted motions, but significant differences between the predicted and recorded motions. The Phase 2 predictions were also consistent and were also quite accurate. The paper reviews the basic experiment, summarizes the results of the Phase 1 and 2 predictions, examines potential explanations for the differences between the predicted and observed motions, and comments on lessons learned and implications for site response practice.

Introduction

The California Geological Survey Strong Motion Instrumentation Program (CSMIP) established an instrumented site effects array in a shallow valley at Turkey Flat, located 8 km southeast of the town of Parkfield about 5 km east of the San Andreas Fault in central California. The array was intended to provide data with which to investigate the accuracy and consistency of current methods for estimating the effects of site conditions on ground surface motions (Tucker and Real, 1986). The array became operational in 1987 and was subjected to numerous episodes of weak shaking; a weak-motion blind prediction exercise was conducted in 1989 (Real and Cramer, 1989; Cramer and Real, 1990a, b; Cramer, 1991). On September 28, 2004, the M6.0 Parkfield earthquake occurred producing much higher levels of ground shaking than the array had previously experienced. This event provided the ground motion records required to conduct the long-anticipated strong motion blind prediction test. In the two-phase test, recorded rock motions were provided to predictors in March, 2005 with predictions due in October, 2005, then additional motions were provided in October, 2005 with predictions due in February, 2006. A symposium was held in September, 2006 to reveal and discuss the measured and predicted surface motions.

Following the prediction symposium, a project was initiated to (a) investigate recorded ground response at the Turkey Flat array at different levels of shaking in multiple events, (b) evaluate equivalent linear and nonlinear blind predictions of site response in the September 28, 2004 Parkfield earthquake, (c) investigate differences between predicted and recorded motions at

the various instrument locations, and (d) summarize lessons learned, recommended practices, and beneficial uses of strong motion records in site response prediction. This paper summarizes the results of that project.

Turkey Flat

The Turkey Flat site is located in a northwest-trending valley within the central California Coastal Range. The valley is filled with a relatively thin layer of stiff alluvial sediments with basement rock outcrops at the south and north ends of the valley (Figure 1). The valley is about 6.5 km long and 1.6 km wide, and is bounded on the north and east by the Maxim fault at the western flank of Table Mountain and on the south and west by a gentle topographic high (Real, 1988) near the Gold Hill fault. The valley is aligned with the southwest-plunging Parkfield syncline in which approximately 1 km of Upper Cretaceous and Tertiary strata overlying Franciscan basement are folded into a U-shape that dip at about 50° and 70° on the southwest and northwest flanks, respectively. The rock immediately underlying the valley sediments is sandstone of the Etchegoin formation.

Instrumentation Array

The Turkey Flat test site includes four recording sites – Rock South (labeled as R1 in Figure 1), Valley Center (V1), Valley North (V2), and Rock North (R2). Surface instruments were installed at each of these sites, and downhole instruments were also installed at the Rock South and Valley Center sites. Downhole instrument D1 was located at a depth of approximately 24 m at the Rock South site, and downhole instruments D2 and D3 were located at depths of approximately 10 m and 24 m, respectively, at the Valley Center site. Instrument D3 was located about 1 m below the soil/rock boundary at the Valley Center site. Each instrument location included a three-component forced-balance accelerometer and a velocity transducer with 12-bit solid-state digital recording. CSMIP also established and maintained a 45-station wide-aperture strong-motion array across the Parkfield segment of the San Andreas fault several km from the Turkey Flat test site (McJunkin and Shakal, 1983).

Subsurface Conditions

The Etchegoin sandstone formation underlies the alluvial sediments and outcrops at the borders of the valley. 25-m-deep boreholes at the southern outcrop showed medium brown to tan, highly friable sandstone with subangular to rounded, well-sorted grains composed of about 50% quartz (Real, 1988). Sandstone velocities (p- and s-wave) were measured by downhole, crosshole, and suspension logging tests; the results were interpreted as indicating two primary zones – an approximately 2.4-m-thick upper zone with $V_s = 200 - 800$ m/sec, and a lower zone with $V_s = 700 - 1,500$ m/sec.

The valley sediments were investigated by seismic reflection and refraction profiling, and by the installation of a dozen borings with sampling and insitu testing. The collective information was interpreted as indicating three primary soil units (Real, 1988). The upper unit consists of dark brown silty clay (at the Valley Center) to sandy clay (at Valley North). The middle unit consists predominantly of clayey sand that contains more gravel and sandy clay at

the Valley North site than at the Valley Center. The lower unit is fine to medium clayey sand with gravel. Shear wave velocities ranged from about 150 m/sec (Valley Center) to 135 m/sec (Valley North) in the upper unit, 460 m/sec (Valley Center) to 275 m/sec (Valley North) in the middle unit, and about 610 m/sec across the valley in the lower unit. The measured shear wave velocity data was used to construct “standard” profiles at the Rock South and Valley Center sites (Figure 2). Participants in the strong motion prediction exercise were required to make a prediction based on the standard profile, and encouraged to make another prediction using a “preferred” velocity profile based on their own interpretation of the field and laboratory velocity data.

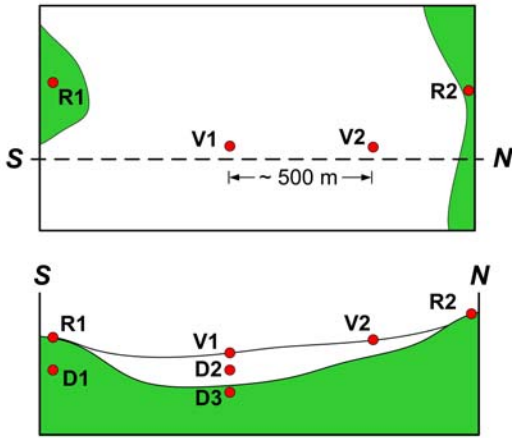


Figure 1. Schematic illustration of Turkey Flat instrumentation layout (after Tucker and Real, 1986).

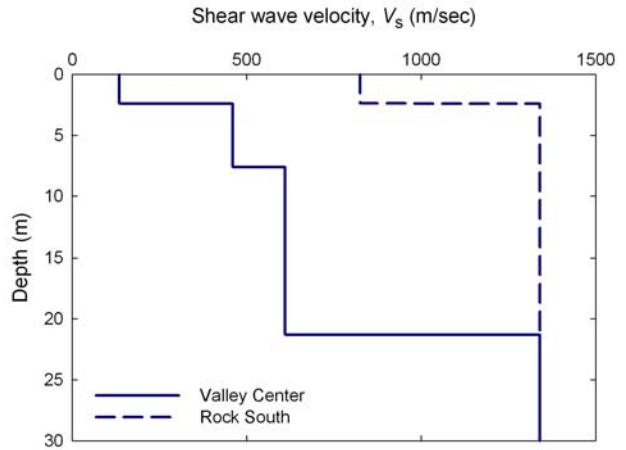


Figure 2. Standard shear wave velocity profiles for Valley Center and Rock South locations (after Real, 1988).

The September 28, 2004 Parkfield Earthquake

After some 17 years of operation, the Turkey Flat test site was subjected to strong ground shaking in the September 28, 2004 Parkfield earthquake. The earthquake was very well-documented and produced an extensive, dense set of near-fault strong motion records with measured peak accelerations of 2g or higher (Shakal et al., 2006a,b). The peak accelerations at the distance of the Turkey Flat test site were generally 0.3g or less.

Recorded Ground Motions

The acceleration time histories recorded at the Rock South and Valley Center arrays are shown in Figure 3. The time histories suggest a modest degree of amplification within the sandstone at the Rock South site; the NS component of the rock surface has a peak acceleration of 0.24g compared with a NS peak acceleration of 0.19g at the 24-m-deep R1 instrument. They also suggest a high degree of amplification at the Valley Center site; the NS peak accelerations at the ground surface (V1), mid-depth (D2), and rock (D3) instruments 0.29g, 0.12g, and 0.06g, respectively. Response spectra for the EW and NS components of the motions were consistent with each other.

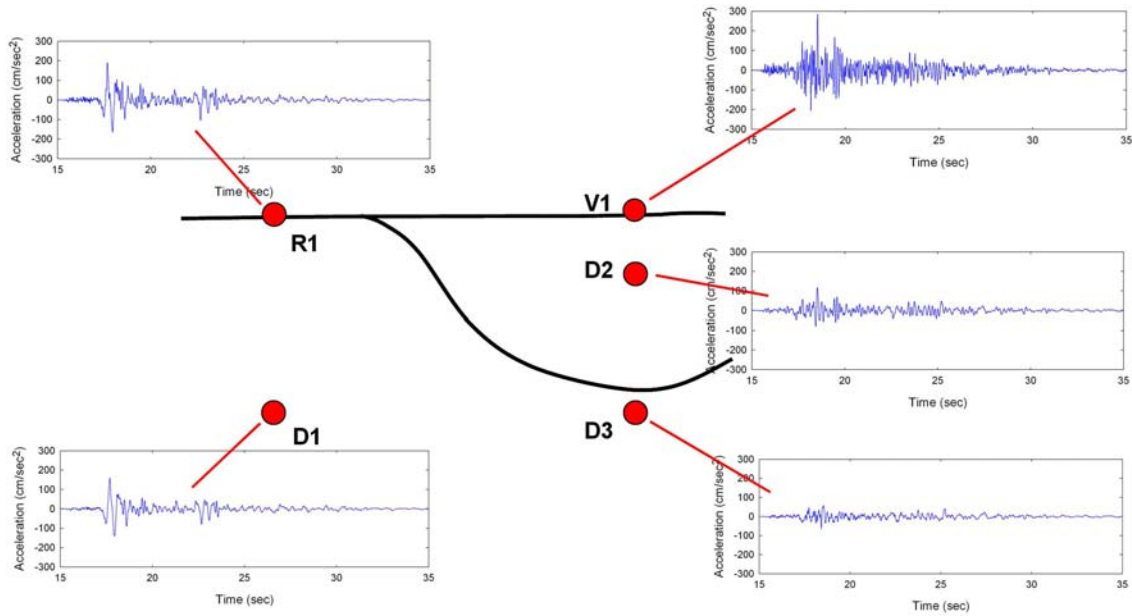


Figure 3. Time histories of North-South accelerations recorded at Rock South and Valley Center downhole arrays in September 28, 2004 Parkfield earthquake.

Other Events

A set of Turkey Flat ground motions produced by eight earthquakes (Table 1) was collected and provided to the earth science community by CSMIP. The 2004 Parkfield earthquake is part of this set, identified as Event 3 in Table 1. Five of the motions are aftershocks of the Parkfield mainshock with magnitudes ranging from 3.7 to 5.0. Other independent events include a 1993 M_w 4.2 event (Event 1) located about 14 km from Turkey Flat, and the more distant M_w 6.5 San Simeon earthquake from 2003.

Table 1 Events producing moderate to strong motion at Turkey Flat (after Haddadi et al., 2008).

Event No.	Event Name	Date	Time	M_w	Epicenter		Distance from Epicenter to:				PGA @ Surface			
					Lat	Lon	RS	VC	VN	RN	RS	VC	VN	RN
1	Apr-93	4/3/1993	21:21:24	4.2	35.942	120.493	14.1	14.5	14.3	13.9	0.026	0.033	0.081	0.047
2	San Simeon	12/22/2003	11:15:56	6.5	35.710	121.100	69.6	70.4	70.6	70.6	0.035	0.036	0.031	0.023
3	Parkfield	9/28/2004	10:15:24	6.0	35.810	120.370	7.6	8.2	8.6	9.2	0.245	0.300	0.260	0.110
4	Aftershock	9/28/2004	10:19:24	4.2	35.844	120.402	5.5	6.3	6.6	7.0	0.052	0.170	0.072	0.034
5	Aftershock	9/28/2004	10:24:15	4.7	35.810	120.350	7.6	8.0	8.4	9.1	0.046	0.074	0.053	0.013
6	Aftershock	9/28/2004	10:33:56	3.7	35.815	120.363	7.0	7.5	8.0	8.6	0.016	0.026	0.026	0.006
7	Aftershock	9/28/2004	12:31:27	4.0	35.840	120.390	5.1	5.9	6.3	6.7	0.012	0.049	0.024	0.008
8	Aftershock	9/29/2004	10:10:04	5.0	35.954	120.502	15.5	15.9	15.7	15.2	0.016	0.042	0.037	0.030

Predicted Ground Motions

The strong motion prediction exercise was conducted in two phases. In the first phase, participants were provided with all available subsurface data and the recorded R1 motions, and asked to predict the response of the Valley Center profile (i.e., the D3, D2, and V1 motions). In the second phase, which was not initiated until all first-phase predictions had been received, participants were provided with the D3 motions and asked to predict the D2 and V1 motions. The first phase was therefore intended to represent the common situation in which recorded bedrock outcrop motions are used as input to ground response analyses, and the second to the much less common situation in which a downhole record is used excite a profile. Differences in

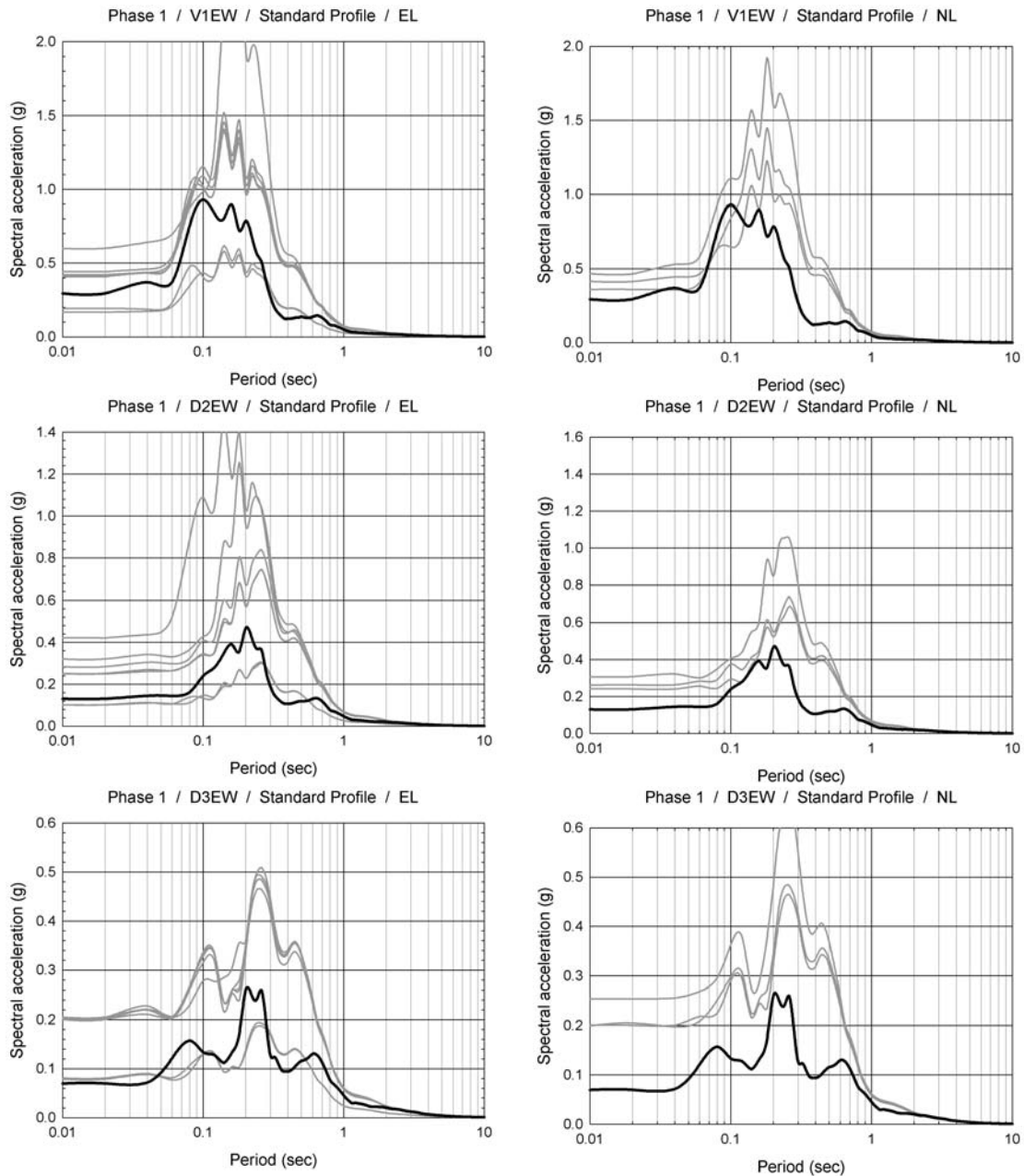


Figure 4. EW response spectra from Phase 1 predicted (gray) and recorded (black) motions.

the motions predicted by the two approaches depend on the extent to which the recorded downhole motion is similar to the “within profile” motion inferred from the rock outcrop motion.

Phase 1 Predictions

The range of predicted motions from equivalent linear and nonlinear analyses using the standard soil model in the first phase are shown for the EW components of the V1, D2, and D3 instruments in Figure 4. The motions can be seen to agree with each other reasonably well, particularly at periods exceeding about 0.3 sec, although there were a number of outliers in different categories. The predicted spectra from both the equivalent linear and nonlinear analyses can be seen to greatly overpredict the recorded motions over a significant range of periods. This overprediction occurs at all three depths within the Valley Center profile.

Phase 2 Predictions

The second phase analyses were performed using the measured bedrock motions at the Valley Center site (D3) as the inputs to the Valley Center profile. The range of predicted EW motions from equivalent linear and nonlinear analyses in the second phase are shown in Figure 5. As in the case of the Phase 1 analyses, the predicted motions can be seen to agree with each other quite well over a wide range of frequencies. The Phase 2 predicted spectra can be seen to match the recorded motions well over a much broader range of periods than the Phase 1 predictions.

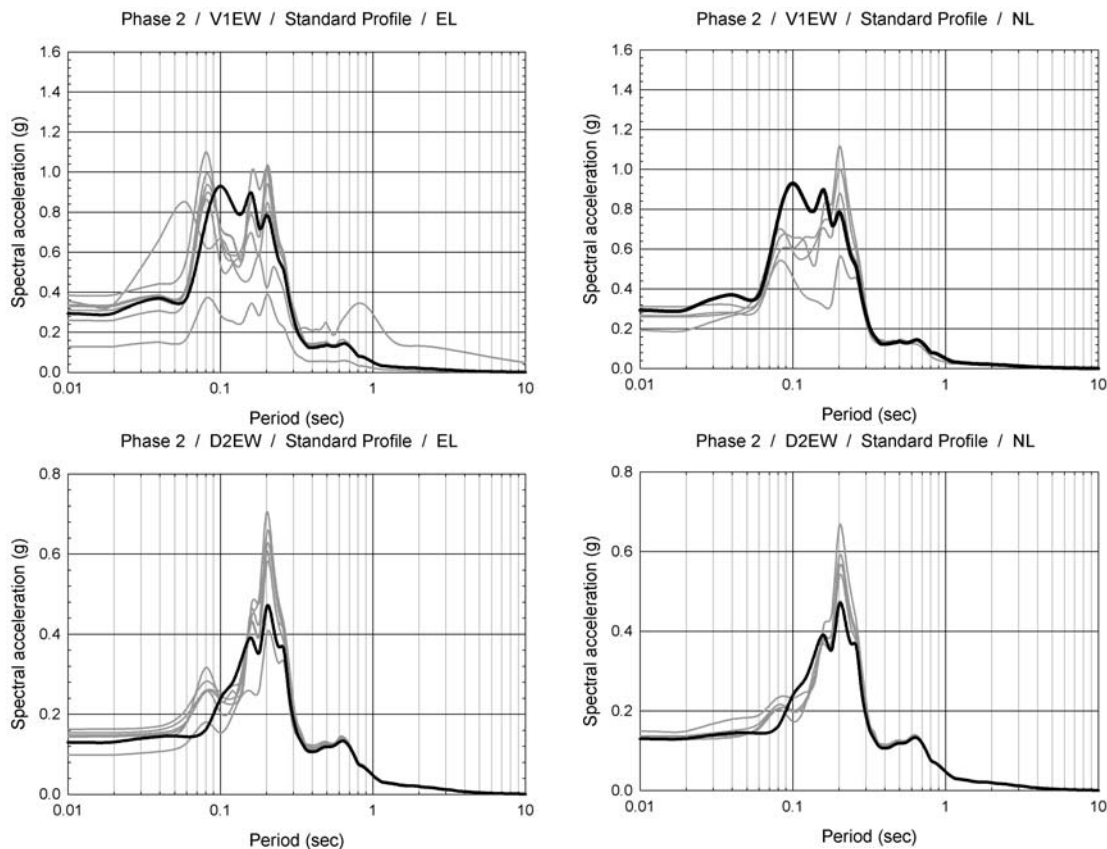


Figure 5. EW response spectra from Phase 2 predicted (gray) and recorded (black) motions.

Comparison of Phase 1 and Phase 2 Predictions

Both the equivalent linear and nonlinear standard analyses with the standard soil model tended to overpredict the response spectra computed from the recorded motions in Phase 1 of the Turkey Flat blind prediction exercise. The overprediction was consistent and systematic. To quantify the prediction errors, residuals defined as

$$R(T) = \ln S_a^{\text{recorded}}(T) - \ln S_a^{\text{predicted}}(T) \quad (1)$$

were computed for all predictions. Note that the residuals are defined in terms of the logarithm of spectral acceleration, and that a high value of $R(T)$ corresponds to an underprediction and a low value of $R(T)$ to an overprediction of the recorded spectral acceleration.

Residuals were computed for all of the Phase 1 and 2 predictions. Figure 6 presents the residuals for the EW components of the equivalent linear and nonlinear standard model predictions of the V1 instrument response. The residuals can be seen to be small at periods greater than about 0.7 sec in the EW direction (and were small below 1.3 sec in the NS direction). At lower periods, however, the residuals are strongly negative, indicating systematic overprediction of spectral accelerations at the Valley Center rock level. The residuals are particularly low, in all cases, for periods of about 0.3-0.7 sec. This overprediction was more pronounced in the NS direction than the EW direction. It should be noted that, due to their logarithmic definition, a mean residual of α corresponds to a median overprediction ratio of $e^{-\alpha}$.

The results point to a fundamental issue with the Phase 1 predictions – the recorded D3 motions are inconsistent with those inferred from the recorded R1 (and, as discussed subsequently, D1) motions, as interpreted in the context of one-dimensional site response. The mean residuals are generally smaller for the equivalent linear predictions than for the nonlinear predictions, but the nature of the prediction errors, as evidenced by the shapes of the residual curves, are quite similar. The value of $\sigma_{\ln R}$ provides an indication of the variability within a given class of predictions. For the standard model predictions, $\sigma_{\ln R}$ essentially represents the model uncertainty since the other most significant variables (i.e., the velocity profile and soil models) are held constant. For preferred profile predictions, $\sigma_{\ln R}$ also includes variability associated with different shear wave velocity profiles and soil models. The variability in the equivalent linear predictions can be seen to be significantly greater than that in the nonlinear predictions. The values of $\sigma_{\ln R}$ for the equivalent linear case, however, are strongly affected by the long-period outliers shown in Figure 5.

In order to quantify the level of overall error in a given prediction using a single, scalar parameter, a “misfit index” for a given prediction was defined as a root-mean-square residual, i.e.,

$$M = \sqrt{\frac{1}{\log(T_{\max}) - \log(T_{\min})} \int_{T_{\min}}^{T_{\max}} [R(T)]^2 d(\log T)} \quad (2)$$

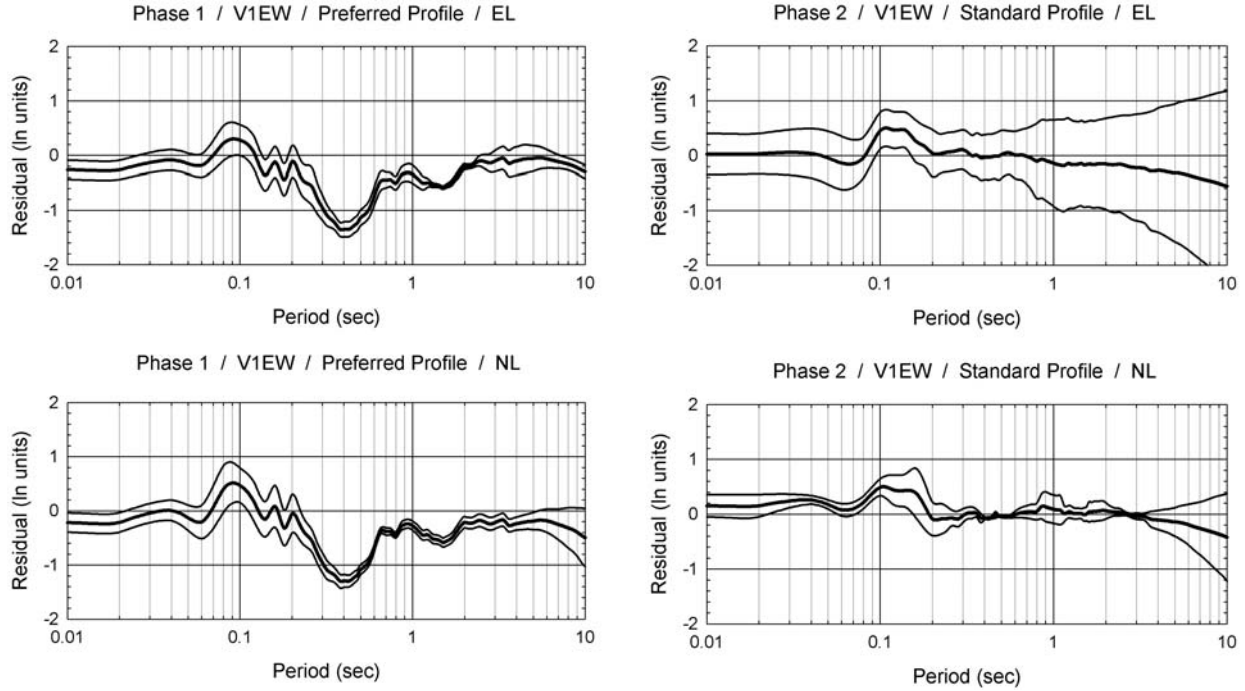


Figure 6. Residuals for Phase 1 and 2 equivalent linear and nonlinear analyses of V1 ground motions using preferred soil models. Bold line indicates mean and lighter lines indicate mean $\pm \sigma_{\ln R}$.

which was computed numerically using $T_{\min} = 0.01$ sec and $T_{\max} = 2.0$ sec as

$$M = \sqrt{\frac{1}{2.301} \sum_{j=1}^{N-1} \frac{1}{2} [R(T_j) + R(T_{j+1})]^2 \cdot (\log T_{j+1} - \log T_j)} \quad (3)$$

where N is the number of periods (57 for the results presented herein) at which spectral accelerations are computed. The upper bound of 2.0 sec in the misfit index definition was selected to focus the index on the period range of greatest interest for Valley Center site response, and to eliminate the effects of prediction errors for long periods at which amplitudes are low and essentially rigid body motion is occurring.

The computed misfit indices are much higher for the Phase 1 predictions (Table 2) than for the Phase 2 predictions (Table 3). Because of the presence of outlier predictions in many cases, the median misfit indices give a better indication of central tendency than the mean values. The misfit indices show that the equivalent linear and nonlinear analyses produced results of similar accuracy, and that the results of analyses based on the standard soil model were generally more accurate, and less variable, than those based on the preferred models.

Table 2 Misfit index statistics for Phase 1 predictions.

Group	Standard Model			Preferred Model		
	Median	Mean	St. Dev.	Median	Mean	St. Dev.
Equivalent linear	1.158	1.070	0.201	1.117	1.190	0.147
Linear	--	--	--	0.916	0.916	0.562
Nonlinear	1.174	1.217	0.207	1.127	1.110	0.134

Table 3 Misfit index statistics for Phase 2 predictions.

Group	Standard Model			Preferred Model		
	Median	Mean	St. Dev.	Median	Mean	St. Dev.
Equivalent linear	0.025	0.432	0.776	0.032	0.044	0.030
Linear	--	--	--	0.250	0.250	0.180
Nonlinear	0.023	0.037	0.031	0.075	0.165	0.254

Comments

The high quality of the Phase 2 predictions (both equivalent linear and nonlinear), in which the Valley Center profiles selected by the participants were excited by the actual bedrock motions, indicates that (a) the site responded essentially one-dimensionally, as intended by the site developers, (b) the site responded essentially linearly in the 2004 Parkfield event, and (c) one-dimensional equivalent linear and nonlinear analyses were able to predict the measured surface response very well when the input motion was known accurately. Nevertheless, uncertainty in the predicted motions still existed. The nature of the predictions were not such that these uncertainties could be estimated in the optimal manner. However, one predictor used a set of five nonlinear analyses for Phase 2 predictions and the Phase 2 equivalent linear predictions were made predominantly using programs that were derivatives of SHAKE (Schnabel et al., 1972). Uncertainties in the Phase 2 standard model predictions (leaving out two equivalent linear predictions with obvious errors) are shown in Figure 7.

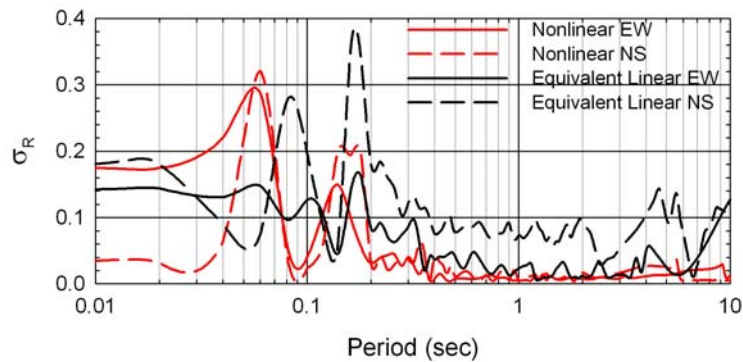


Figure 7. Estimated model-to-model uncertainty for equivalent linear and nonlinear predictions of ground surface motions.

Investigation of Site Response Inconsistencies

Of significant interest is the reason for the difference in accuracy between the Phase 1 and Phase 2 predictions. Developing an understanding of the measured response requires a close look at the responses of both the Rock South and Valley Center profiles. Equivalent linear analyses of the Rock South site response showed a high level of consistency between the R1 and D1 motions, i.e., the recorded R1 motion could be predicted accurately in a one-dimensional analysis of the Rock South profile using the recorded D1 motion as input. The Phase 2 analyses showed that the recorded V1 motion could be predicted accurately using the standard soil model with the recorded D3 motion used as input. These results show that the poor performance of the Phase 1 predictions was due to the inconsistency between the D1 (and R1) and D3 rock motions.

In order to determine the consistency of the Rock South and Valley Center rock motions with the motions measured or inferred at other sites, rock outcrop motions for all four sites were developed. For the Rock South and Rock North sites, the recorded rock outcrop motions were used. For the Valley Center site, the recorded motion at the D3 instrument was corrected to obtain a consistent rock outcrop motion. The inferred rock outcrop motion at the Valley North site was obtained by deconvolving the recorded Valley North surface motion down to bedrock level. The resulting motions are shown in Figure 8.

The degree to which any of the rock outcrop motions could be considered unusual with respect to ground motions at similar distances in similar earthquake can be evaluated using the parameter “epsilon.” To account for both components of ground motion, a value of epsilon was computed using the SRSS spectral accelerations, i.e., as

$$\varepsilon = \frac{\ln S_a^{SRSS}(T) - \ln \hat{S}_a(T)}{\sigma_{\ln S_a}} \quad (4)$$

where $\ln S_a^{SRSS}(T) = \sqrt{(\ln S_a^{EW}(T))^2 + (\ln S_a^{NS}(T))^2}$ and $\hat{S}_a(T)$ is the median spectral acceleration predicted by the Campbell and Bozorgnia (2008) attenuation relationship. The epsilon value indicates the number of (logarithmic) standard deviations above or below the median value of a ground motion parameter. Figure 9 shows the epsilon values for the four rock outcrop motions. The epsilon values indicate that the spectral accelerations in the period range of 0.3 – 0.8 sec at the Rock South site were well above the median values and that the Valley Center rock spectral accelerations in the 0.3 – 0.5 sec period range were well below the median values. These results are consistent with the very large apparent differences in the Rock South and Valley Center rock motions at periods of about 0.3 – 0.5 sec.

Shallow Rock Weathering Effects

At the 2006 Blind Prediction Symposium, considerable discussion centered on the potential for weathering of the upper portion of the rock to cause the discrepancy between the Rock South and Valley Center rock motions. This potential was investigated by an extensive series of one-dimensional, equivalent linear analyses which found no remotely feasible

weathering-related velocity profile that would produce the observed inconsistency. As a result, shallow weathering effects were ruled out as a significant cause of the inconsistency.

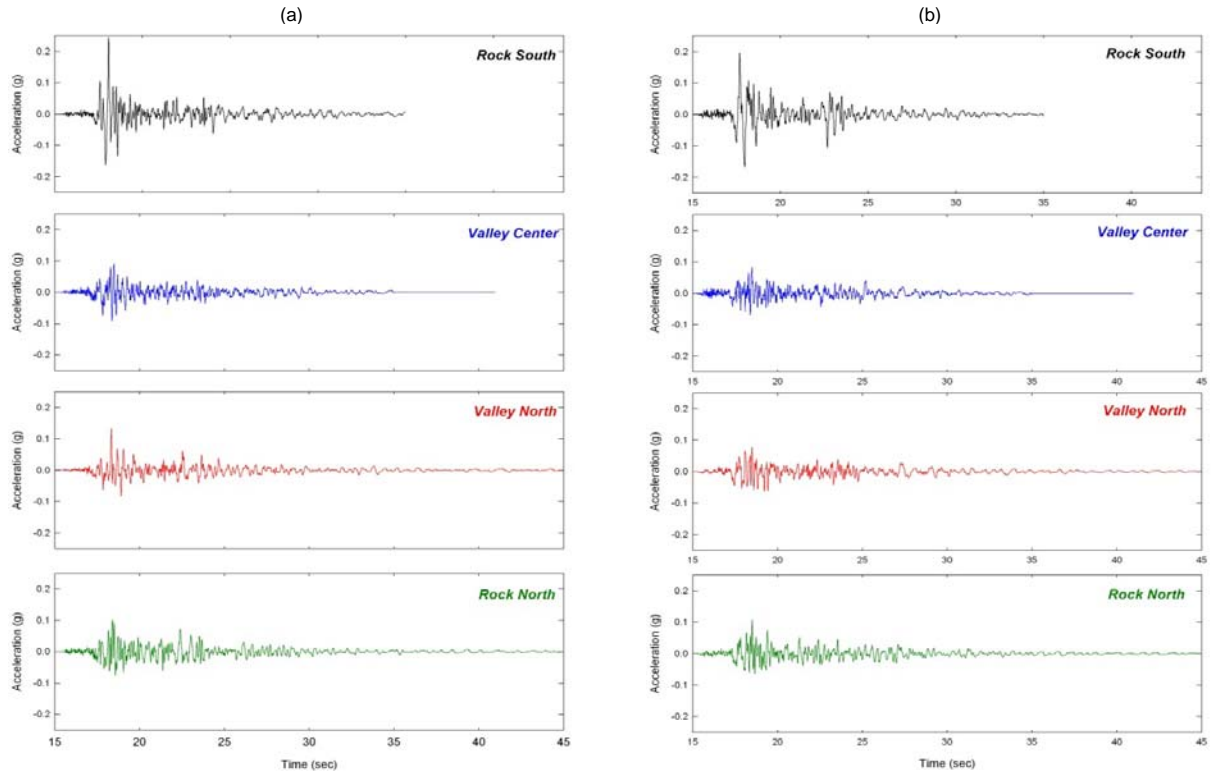


Figure 8. Rock outcrop time histories at all four Turkey Flat sites (a) EW components, and (b) NS components.

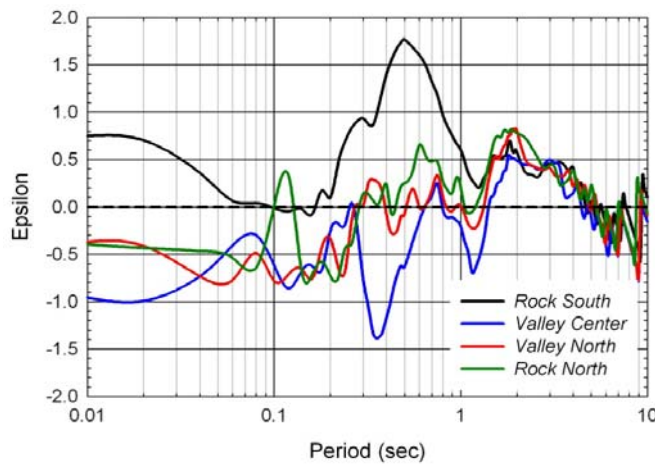


Figure 9. Epsilon values for four Turkey Flat rock outcrop motions. Median spectral accelerations calculated using Campbell and Bozorgnia (2009) with $V_{s,30} = 1,276$ m/sec, $Z_{2.5} = 0.27$ km, $M_w = 6.0$, and $R = 7.6, 8.2, 8.6,$ and 9.2 km.

Deep Velocity Anomaly Effects

Another potential explanation of the inconsistency between the D1 and D3 motions is the presence of an anomalous velocity zone at depths greater than those explored in the Turkey Flat subsurface investigation. The potential existence of such an anomaly is suggested by data from downhole studies in the Varian No. 1 well, a 1,500-m deep well located north of the Turkey Flat test. Sonic logging data (Real, 1988) from the well showed a zone of reduced shear wave velocity at a depth of approximately 600 – 720 m. Furthermore, a series of seismic refraction tests performed at the Turkey Flat test array site showed evidence of a low-velocity layer at about the mid-depth (900 – 1100 m deep) of the Etchegoin formation. The persistence of this layer suggests that it also exists beneath the Turkey Flat test array. The potential for such an anomaly to cause differences consistent with those observed in the 2004 Parkfield earthquake were investigated in a series of equivalent linear analyses.

To investigate the potential effects of a deeper velocity anomaly, deep one-dimensional profiles were developed for both the Rock South and Valley Center sites. The deep profiles extended to depths of 1 km. The goal of this investigation was to determine whether a single anomaly located at the same depth below the top of bedrock could produce the observed D1 and D3 motions when subjected to the same motion at a depth of 1 km. A velocity multiplier function was used to modify the standard velocity profile at large depths. The multiplier function could describe a depth-dependent anomaly of variable depth, amplitude, and shape. Site response analyses using the computer program SHAKE91 were implemented into a numerical optimization analysis. The parameters defining the velocity multiplier function were then optimized to identify the characteristics of the deep velocity anomaly that produced rock motions that were most consistent with both components of the recorded Rock South and Valley Center rock motions.

The first optimization analyses were performed with a velocity anomaly equivalent to that suggested in previous subsurface investigations, and were repeated many times with different initial velocity anomaly profiles. The lowest value of the objective function in numerous optimization analyses was obtained for a profile with the velocity multiplier function that had values greater than 1.0, indicating that a zone of increased velocity between depths of approximately 450 m and 800 m provided the best fit between the Rock South and Valley Center rock motions. The level of agreement with the optimized function was poor, and the inferred spectra had amplitudes that could not realistically be expected at a depth of 1 km. As a result, a deep velocity anomaly was ruled out as a significant cause of the observed inconsistency in the Rock South and Valley Center rock motions.

Higher Dimensional Effects

Local multi-dimensional subsurface and topographic features can also cause focusing, or amplified shaking, at some orientations and frequencies. Seismic refraction surveys in the vicinity of the Rock South site produced the inferred subsurface velocity profile shown in Figure 10. The nature of the contact between the materials with shear wave velocities of 1,520 m/sec and 3,350 m/sec could potentially lead to some focusing of vertically propagating shear waves that would cause locally increased motions at some frequencies at the Rock South site.

Depending on the three-dimensional nature of that contact, which is not known, this local amplification could be stronger in some directions than others.

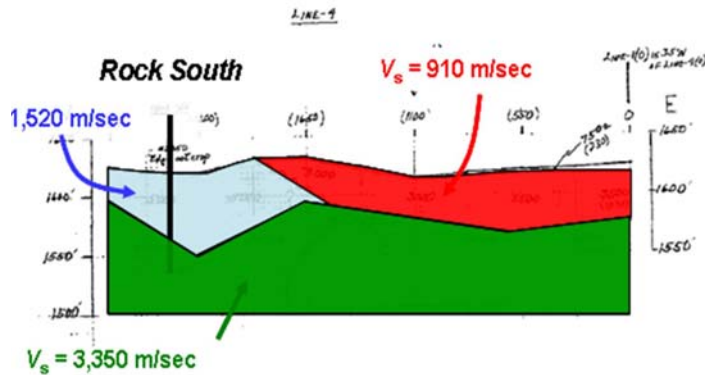


Figure 10. Inferred velocity profile in vicinity of Rock South recording instrument (after Real, 1988).

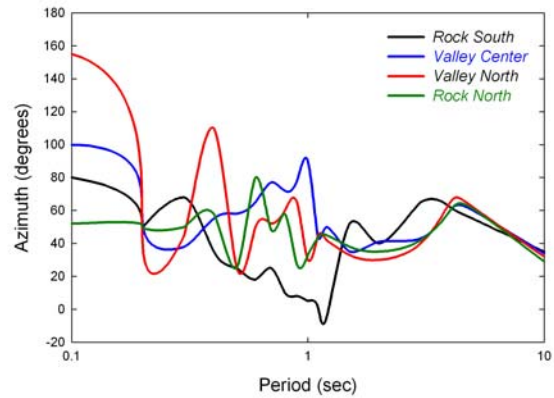


Figure 11. Azimuthal orientation of maximum spectral acceleration. Azimuthal angle is measured clockwise from north-south direction.

The orientation of the maximum response of all of the rock motions was also examined. Figure 11 shows the azimuthal orientation of the maximum spectral acceleration at different periods for all four sets of rock motions. Since the Turkey Flat array is located near the epicenter of the 2004 Parkfield earthquake, the maximum response would be expected in the fault-normal direction, which would be at about 48 degrees in Figure 10, and most of the maximum response is oriented in that general direction. The azimuthal directions at all four locations are quite consistent at periods greater than 2 sec, and much more variable at shorter periods. The Rock South and Valley Center rock motions show relatively consistent orientations at periods lower than about 0.3 sec, but have substantially different orientations at periods of about 0.5 – 1.2 sec. In this period range, the strongest Rock South motions tend to be in the NS direction and the strongest Valley Center motions are aligned in a more EW direction. Such differences could potentially be associated with three-dimensional subsurface geometry, and possibly associated with the geometry of the rock surface at the location of the Rock South instrument. Hence, higher dimensional effects could be a potential contributor to the inconsistency between the Rock South and Valley Center rock motions.

Path Effects

In order to investigate the extent to which path effects may have affected the inconsistency between the Rock South and Valley Center rock motions, the average $\ln S_a(T)$ values for both recorded components of all four rock outcrop motions between $T = 0.4$ sec and $T = 0.5$ sec were computed. These values were then used to compute a relative rock motion parameter defined as the difference between the value computed from the RS motion and the average of the values computed for all four motions, i.e.

$$R_{RS} = \ln[\bar{S}_{a,RS}(0.4 - 0.5)] - \overline{\ln[\bar{S}_{a,all}(0.4 - 0.5)]} \quad (5)$$

where $\overline{\ln[\bar{S}_{a,all}(0.4-0.5)]}$ is the average of the average (natural) logarithmic spectral acceleration for all four pairs of rock outcrop motions. Positive values of R_{RS} , therefore, indicate cases where the Rock South motion is stronger than average and negative values indicate cases in which it is weaker.

The values of R_{RS} for each of the eight events are listed and shown graphically in Figure 12. The azimuthal variation of the relative degree to which the Rock South motion exceeds the other rock outcrop motions is notable. The R_{RS} value for Event 3 is the highest, but the values for the other events initiating nearly due south of the Turkey Flat array are the next highest. The three events located west and southwest of the array have intermediate values, and the R_{RS} values for the two events located northwest of the Turkey Flat array have very low and even negative values, indicating that the 0.4 – 0.5 sec spectral accelerations at Rock South for these events ranged from about 2% weaker to only 5% stronger than the average at all four sites. The exponentials of the R_{RS} values, which represent ratios of the Rock South value to the mean value, are shown with azimuth (measured clockwise from due north) in Figure 13.

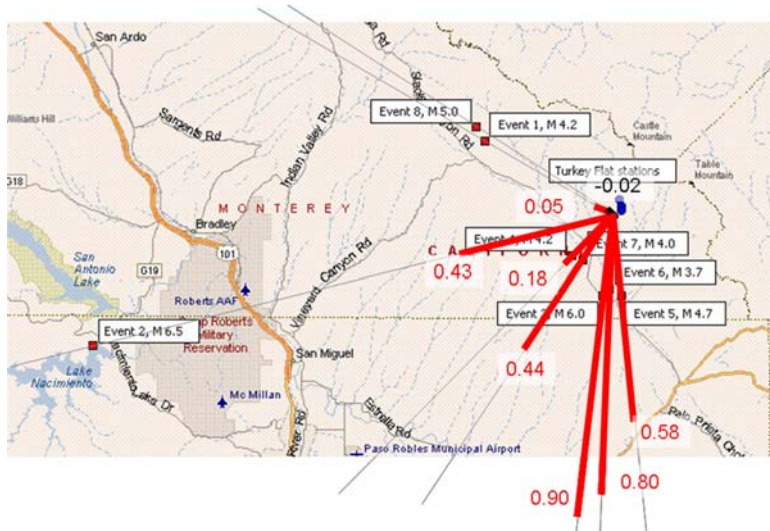


Figure 12. Variation of RRS with azimuthal direction for each of eight events producing strong ground motion at Turkey Flat.

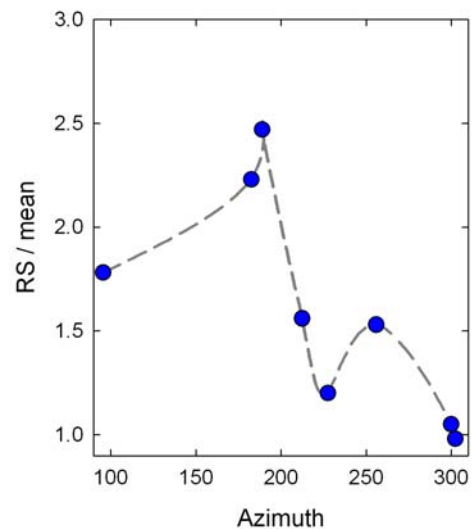


Figure 13. Variation of ground motion intensity ($\exp(R_{RS})$) with azimuth (clockwise from due north).

Thus, this relatively small dataset suggests strong variability of ground motion intensity in the 0.4 – 0.5 sec period range at Turkey Flat. Such variability has been observed in previous earthquakes. The Northridge earthquake, for example, produced localized areas of higher damage in certain areas. Studies of aftershock data (e.g., Gao et al., 1996; Davis et al., 2000) showed that amplification factors were quite sensitive to the path between the epicenter and the recording instrument (Boore, 2004), a result attributed to critical refractions. Of interest for Turkey Flat is the fact that the path for all but Events 1 and 8 crossed the Gold Hill fault, located just northeast of the San Andreas fault near Turkey Flat, before reaching the Turkey Flat array. The fact that these motions exhibited significantly stronger Rock South response than those that

did not cross the Gold Hill fault suggests that path effects may have played a significant role in the inconsistency between the Rock South and Valley Center rock motions.

Observations

A number of observations relevant to the estimation of ground motion hazards can be made from the ground motions that have been recorded by the Turkey Flat strong motion array and from the attempts at predicting those motions. These observations are made from the perspective of site response analyst charged with making the types of predictions that form the basis for seismic design of various infrastructure elements.

Observations of Site Response

Observations about site response, which are based on interpretation of recordings from multiple events, are divided into those associated with source, path, and site effects.

Source Effects

Source effects can have important effects on the motions recorded by a spatially distributed array, particularly when rupture occurs over a length of fault that is large with respect to the distances of the array stations from the fault and from each other. In the case of the 2004 Parkfield earthquake, rupture occurred over a length of approximately 20 km located mostly northwest of the hypocenter. As discussed previously, the earthquake produced spatially variable ground motions in the near-fault region. Some of this variability is attributable to source effects, such as the slip distribution and locations of asperities on the rupture surface. Other aspects of the variability could be due to three-dimensional fault zone effects such as lateral refraction, fault zone guided waves (Jongmans and Malin, 1995), and other three-dimensional multipathing effects (Kim and Dreger, 2008). In a source inversion investigation, Kim and Dreger (2008) excluded a number of recorded motions from a zone generally within about 4-5 km northeast of the rupture surface due to complexity associated with fault structure. That zone extended to the location of the Turkey Flat array, and suggests that the motions recorded by the array could potentially have been influenced by such effects.

Path Effects

The path from the source of the 2004 Parkfield earthquake to the Turkey Flat strong motions stations is complicated. The geology shows a significant syncline beneath Turkey Flat (between the Gold Hill and Maxim faults), and a steeply dipping boundary between the granitic Salinian block (on the west) and the softer Franciscan rock (on the east) of the Gold Hill fault. Deep explorations to the north of Turkey Flat revealed three flower structures, i.e., groups of nested rupture surfaces along the San Andreas fault (Rymer et al., 2004; Thayer and Arrowsmith, 1995a,b). Given the reduced stiffnesses of materials encountered along such rupture surfaces and along the Gold Hill fault, waves crossing portions of the flower structure could be refracted or otherwise affected by those structures. Also, the distances from the rupture surface to the Turkey Flat instruments were relatively short compared with the distances between the instruments, so waves traveled to the instruments along different paths. As a result, path effects could have led to significant differences between the rock motions at the four Turkey Flat sites.

The Turkey Flat array has also recorded motions from other earthquakes and from aftershocks of the 2004 Parkfield earthquake. These events occurred at a number of locations, some of which were near that of the 2004 Parkfield event and some of which were at different locations. Analyses of the recorded motions from these other events showed that the relationship between the rock motions at the Rock South and Valley Center sites was similar to that of the 2004 Parkfield earthquake for the events located at about the same azimuthal angle from that earthquake, but were considerably different for those at different azimuthal angles. The events located to the north of the Turkey Flat array, for which waves did not have to cross the Gold Hill fault, produced rock motions at the Rock South and Valley Center sites that were quite consistent with each other. Events for which waves did have to cross the Gold Hill fault to reach Turkey Flat produced significantly inconsistent Rock South and Valley Center rock motions. These observations help illustrate the important influence of path effects on motions at the Turkey Flat array.

Site Effects

The Turkey Flat test site (specifically, the Valley Center site) was selected so that the common one-dimensional idealization would be as appropriate as possible. The edges of the valley, however, may have been more susceptible to two- or three-dimensional effects. Topographic contours and subsurface conditions in the vicinity of the Rock South station indicate some potential three-dimensional effects, although the flat nature of the ground suggests that they should be relatively subtle.

The measured site response at the Valley Center profile was consistent with expectations given the recorded rock motions beneath the valley sediments. The ground motion amplitudes increased from the rock level through the soil profile and up to the ground surface. Because the Turkey Flat region was between the lobes of strongest shaking closer to the ends of the fault rupture, the ground motions did not induce high strains, and consequent significant nonlinearity, in the relatively stiff, unsaturated Valley Center sediments.

Observations of Predicted Response

The Turkey Flat Blind Prediction test provided an opportunity to evaluate the predictive capabilities of both computer programs and people. The predictors were generally quite experienced engineers and earth scientists who were very familiar with, and in quite a few cases developers of, the site response codes used to make their predictions. Nevertheless, there was still a significant degree of variability in the predicted ground motions.

The predictors used a range of analytical techniques, and a range of specific computer programs, to make their predictions. Most prediction groups used one or possibly two site response models within a given model category, but one group used five nonlinear models with consistent application protocols. Analysis of that group's predictions offers insight into the model-to-model component of prediction variability. Unfortunately, no single specific model was used by a sufficient number of predictors to allow direct evaluation of predictor-to-predictor variability.

Phase 1 Predictions

The Phase 1 predictions tested, in addition to the ability to predict soil profile response given a rock input motion, the ability to predict the rock motion beneath the soil profile from a rock outcrop motion recorded some 800 m away. These predictions were made using both standard and preferred soil models.

The primary observation in all of the Phase 1 predictions is the strong and consistent overprediction of site response, particularly in the period range of 0.3 - 0.6 sec. This prediction error, which was consistently produced by virtually all of the Phase 1 predictors, dominated the Phase 1 results. The error was so large as to reduce the significance of some of the observations and conclusions that could be drawn from the Phase 1 predictions.

Phase 2 Predictions

The Phase 2 predictions were based on the recorded rock (D3) motions beneath the Valley Center soil profile; as a result, the error in predicting the D3 motion from the R1 motion was eliminated. The predictions in the Phase 2 analyses, using both standard and preferred soil models, were much better than those from the Phase 1 analyses. The recorded response was generally predicted quite accurately at periods as low as 0.2-0.3 sec, which was much closer to the extended characteristic site period and helps validate the one-dimensional assumption inherent in the great majority of the predictions.

Lessons Learned from Observations

The Turkey Flat Blind Prediction test required a tremendous effort by many people, ranging from the planning, design, installation, and monitoring of the array itself to the performance of the ground motion predictions. A number of lessons can be learned from the observed site response and efforts at its prediction. Those lessons are tabulated below:

1. While Turkey Flat itself is relatively simple and was a good choice for testing the earth science and geotechnical professions' ability to predict one-dimensional response, the area between Turkey Flat and the source of the 2004 Parkfield earthquake (i.e., the San Andreas fault) is quite complicated. This type of complexity can lead to significant variability in rock motions.
2. The extent to which nearby rock motions can be used to predict site response is affected by proximity of the site to the rock motion and on source-site distance. In Phase 1 of the Turkey Flat Blind Prediction test, as-yet-unexplained inconsistencies between rock motions at sites located 800 m apart caused poor predictions of soil profile response.
3. Path effects can be important, particularly in areas with complicated geologic conditions and in the presence of intermediate faults or fault zones. Fault zones can give rise to waveguide effects and can refract waves in a complicated manner that can lead to spatial variability of rock motions. At Turkey Flat, motions from events in which waves did not have to cross the Gold Hill fault appeared to produce much more consistent rock motions than events located on the other side of that fault.
4. The extensive site characterization program undertaken at Turkey Flat involved several different types of tests and produced a number of different subsurface velocity profiles.

Analyses based on individual velocity profiles were not, in general, as accurate as those based on the standard profile, which approximated the average velocities from all of the tests.

5. Site response is most sensitive to the shear wave velocity profile. Shear wave velocities at shallow depths, while difficult to measure accurately, can have a strong effect on spectral response, particularly at low periods.
6. Even for cases in which substantial consistency in ground motion predictions were expected (e.g., standard model predictions using equivalent linear analyses), outlier predictions were found.
7. The availability of downhole soil records is extremely useful for validation of site response analyses. Some predictions produced reasonably good fits to the recorded ground surface spectra while making relatively poor predictions of the recorded motion at 10 m depth. Ideally, a good prediction would be good at all depths.
8. The general consistency of the predictions suggest that differences in predictions have more to do with different interpretations of site characteristics than with differences in methods of analysis. There are many available software packages that, when used with appropriate site characterization, can produce accurate ground motion predictions.
9. Both average prediction error (bias) and dispersion of a group of ground motion predictions were observed to vary with depth. In Phase 2, where the input motion was known much more accurately than in Phase 1, the average error and dispersion both decreased with depth, although the variability in Phase 2 standard model predictions was unexpectedly (and inexplicably, given the available information) high.
10. Some predictors made use of the results of available weak-motion data to “tune” their preferred models prior to making their predictions. The most common approach was to adjust the shear wave velocity profile until the periods of computed local spectral peaks matched those of the recorded motions, and then to adjust the low-strain damping until the amplitudes agreed. The use of this data did appear to produce some benefits with respect to prediction accuracy.
11. For the previously discussed reasons, the Phase 1 predictions were all inaccurate at periods below about 0.6 – 1.5 sec in the EW and NS directions. The Phase 2 predictions, which were not affected by the inconsistency between the R1 and D3 motions, showed good accuracy in an average sense. The level and patterns of the errors in average equivalent linear and nonlinear predictions were similar, indicating that nonlinear analyses can predict response consistent with equivalent linear analyses when nonlinearity is modest.
12. The nonlinear analyses had a tendency to underpredict both the recorded response and the equivalent linear predictions at low periods. While some of the difference between the predicted and recorded response could be due to errors in assumed shallow shear wave velocities, the differences between the mean nonlinear and equivalent linear predictions suggest that other factors may also have contributed. The nonlinear models are not able to independently control stiffness and damping behavior, so attempts at matching both usually result in damping ratios that are higher than would be expected for the modeled stiffness behavior. Also, most of the nonlinear codes use Rayleigh damping, which is inherently frequency-dependent. Modified Rayleigh damping formulations render the effective

damping ratio relatively constant over a certain frequency range, but frequencies above that range are still highly damped.

13. Interpretation of the results of the Turkey Flat Blind Prediction test showed that better (i.e., more accurate) average predictions were made using the standard soil model than the preferred models. While some preferred models produced predictions that were superior to the standard model predictions, on average they did not. The standard model was developed by consensus of a group of experts who were quite familiar with the site and the results of the extensive site characterization work. As a consensus-based profile, it was relatively simple in comparison to most of the referred profiles; nevertheless, it worked quite well.

Recommended Practices

The lessons learned from the Turkey Flat Blind Prediction test can be used to formulate some recommendations for site response analysis practice. The following paragraphs describe recommendations related to the results of the Turkey Flat Blind Prediction test, and should not be considered an exhaustive set of recommendations for site response practice.

1. Site response analysts should recognize that accurate site characterization is required for accurate prediction of site response. More attention should, in nearly all cases, be paid to the manner in which subsurface data is obtained and interpreted than to which particular method of site response analysis is utilized. For sites softer than that at Turkey Flat and/or for stronger levels of shaking, larger differences between different classes of analysis (e.g., equivalent linear or nonlinear) and different site response computer programs will be observed, but differences in site characterization will usually dominate differences in computational methods.
2. Different insitu and laboratory tests provide different types and levels of information on subsurface conditions. The acquisition of extensive amounts of subsurface data, and of different types of subsurface data, is recommended whenever possible.
3. Evaluation and interpretation of subsurface data for the purpose of developing a standard site model proved to be beneficial for estimation of site response at Turkey Flat. When possible, collaborative development of a site model by a panel of experts should be used. In some cases, the site model may include more than one soil profile for analysis.
4. Development of a standard site model should include consideration of the level of nonlinearity expected to be induced in the soils by the ground motions of interest. For the ground motions produced at Turkey Flat by the 2004 Parkfield earthquake, nonlinearity in the Valley Center soil profile was modest. Under such conditions, analysis of a single, consensus-based average soil profile can produce results that are consistent with the average of analyses of profiles that span the range of potential input parameter values. For sites or ground motions where greater levels of nonlinearity are expected, however, consideration of the range of results may require analyses of multiple soil profiles that span the range of input parameter values. Averaging the results of the multiple analyses will produce a better indication of the expected response than the results of a single analysis of an average profile.
5. When available, the use of recorded weak motion response can help confirm or improve a standard site model. Measurement of ground motions from small earthquakes or ambient

vibration, interpreted in terms of H/V ratios if only surface motions are possible, can be used to estimate the fundamental period of a soil profile; that information can be used to tune a shear wave velocity profile used in a site response analysis for design-level ground motions.

6. The method of site response analysis should be appropriate for the problem at hand. For cases involving stiff sites and/or weak motions, soil strains will be small, hence nonlinear effects will be modest. In such cases, both equivalent linear and nonlinear analyses can produce very similar response. Attention must be paid to the manner in which nonlinear analyses treat stiffness and damping when nonlinear response occurs. The inability of nonlinear models to independently control stiffness and damping behavior means that one or both will generally be modeled inaccurately. Given the sensitivity of site response to stiffness, modeling the stiffness correctly is more important than modeling the damping behavior correctly. With most nonlinear models, matching the stiffness behavior will lead to overpredicted damping.
7. Many nonlinear models, particularly those based on lumped-mass models of the soil profile, use some form of Rayleigh damping. The basic form of Rayleigh damping has a strong tendency to overdamp high frequency motions; extended Rayleigh damping formulations have been shown to be effective in controlling damping over a desired range of frequencies and to provide improved predictive capabilities.
8. The expected results of a site response analysis should be estimated before performing the analysis. The analyst should recognize the range of periods expected to be influenced by the local soil conditions. Site response will be low at periods beyond the characteristic (fundamental) site period, so analyses with multiple motions should produce very similar amplification behavior at periods longer than the characteristic site period – if they don't, an error may be the cause. By the same token, consistent results at periods beyond the characteristic site period should not be taken as evidence that the site profile has been modeled correctly. After performing the site response analysis, the results should be checked against the expected results to confirm their general validity or to expose potential modeling problems. Discrepancies should be resolved or rationalized before the analytical results are used for design or evaluation purposes.
9. Site response analysts should strive to understand the relationship between the various soil units in a particular profile and the different regions of a response spectrum. Shallow zones will be excited by short wavelengths, which generally correspond to higher frequencies. Similarly, deeper zones will respond most strongly to longer wavelengths which depend on the characteristics of a deeper zone of soil. If high frequencies are of particular interest at a given site, more attention may need to be paid to accurate measurement of shear wave velocities of shallow soils.
10. Uncertainty exists and design site response studies should explore and accommodate it. Studies at numerous sites, including Turkey Flat, have shown that uncertainty in the shear wave velocity profile contributes much more strongly to total uncertainty than other significant sources. With the availability of convenient, Windows-based site response programs, sensitivity analyses can be performed quickly and conveniently, and should nearly always be performed. When possible, response analyses with randomized velocity profiles should be performed to allow the analyst to understand and accommodate, as necessary, the uncertainty in site response.

Acknowledgments

The author would like to acknowledge the support of the California Strong Motion Instrumentation Program of the California Geological Survey. In particular, Tony Shakal, Hamid Haddadi, and Moh Huang were very helpful with the provision and interpretation of data. Feedback from the CSMIP Advisory Committee was also very helpful.

References

- Cramer, C.H. (1991). "Turkey Flat, USA Site Effects Test Area – Report 6, Observations and Modeling," California Division of Mines and Geology, ESAU Technical Report No. 91-1, 92 pp.
- Real, C.R. and Cramer, C.H. (1989). "Turkey Flat, USA Site Effects Test Area – Report 3, Weak Motion Test: Prediction Criteria and Input Rock Motions," California Division of Mines and Geology, ESAU Technical Report No. 89-1, 48 pp.
- Cramer, C.H. and Real, C.R. (1990a). "Turkey Flat, USA Site Effects Test Area – Report 4, Weak Motion Test: Observed Seismic Response," California Division of Mines and Geology, ESAU Technical Report No. 89-1, 28 pp.
- Cramer, C.H. and Real, C.R. (1990b). "Turkey Flat, USA Site Effects Test Area – Report 5, Weak Motion Test: Statistical Analysis of Submitted Predictions and Comparison to Observations," California Division of Mines and Geology, ESAU Technical Report No. 90-2, 57 pp.
- Jongmans, D. and Malin, P.E. (1995). "Microearthquake S-wave observations from 0 to 1 km in the Varian well at Parkfield, California," *Bulletin of the Seismological Society of America*, Vol. 85; No. 6; pp. 1805-1820.
- Kim, A. and Dreger, D.S. (2008). "Rupture process of the 2004 Parkfield earthquake from near-fault seismic waveform and geodetic records," *Journal of Geophysical Research*, 113, B07308, doi:10.1029/2007JB005115, 16 pp.
- McJunkin, R.D. and Shakal, A.F. (1983). "The Parkfield Strong-Motion Array," *California Geology*, Vol. 36, No. 2, pp. 27-34.
- Real, C.R. (1988). "Turkey Flat, USA Site Effects Test Area – Report 2: Site Characterization," California Division of Mines and Geology, ESAU Technical Report No. TR 88-2, 39 pp.
- Real, C.R., Shakal, A.F., and Tucker, B.E. (2006). "Turkey Flat, U.S.A. Site Effects Test Area: Anatomy of a Blind Ground-Motion Prediction Test," Third International Symposium on the Effects of Surface Geology on Seismic Motion, Grenoble, France, Paper Number KN 3, pp. 1-19
- Rymer, M. J., R. D. Catchings, M. Thayer, and J R. Arrowsmith (2004). Structure of the San Andreas fault zone and SAFOD drill site as revealed by surface geologic mapping and seismic profiling near Parkfield, California, *EOS Trans. Am. Geophys. Union* **85**, no. 47, Fall Meet. Suppl., Abstract T11F-08.

Shakal, A., H. Haddadi, V. Graizer, K. Lin and M. Huang (2006a). Some key features of the strong motion data from the M6.0 Parkfield, California, earthquake of 28 September 2004, *Bulletin of the Seismological Society of America*, Vol. 96, No. 4B, S90-S118.

Shakal, A., H. Haddadi and M. Huang (2006b). Note on the very high-acceleration Fault Zone 16 record from the 2004 Parkfield earthquake, *Bulletin of the Seismological Society of America*, Vol. 96, No. 4B, S119-S142.

Thayer, M. R., and J R. Arrowsmith (2005a). Fault zone structure of Middle Mountain, Central California, *EOS Trans. Am. Geophys. Union*, **86**, no. 52, Fall Meet. Suppl., Abstract T21A-0458.

Thayer, M. R., and J R. Arrowsmith (2005b). Geology and geomorphology of the San Andreas fault near Parkfield, California, geologic mapping and structural synthesis, <http://activetectonics.la.asu.edu/Parkfield/structure.html>.

Tucker, B. and Real, C.R. (1986). "Turkey Flat, USA Site Effects Test Area – Report 1: Needs, Goals, and Objectives," TR 86-1, California Department of Conservation, Division of Mines and Geology, 16 pp.

SCHEMES FOR RECONSTRUCTING THE SEISMIC RESPONSE OF INSTRUMENTED BUILDINGS

Dionisio Bernal¹ and Arash Nasser²

¹Civil and Environmental Engineering Department, Center for Digital Signal Processing, Northeastern University, Boston, MA.

² Graduate Student, Northeastern University, Boston, MA,

Abstract

Methodology for reconstructing the seismic response of buildings from measured accelerations is examined. The popular cubic spline (CS) interpolation is shown to be equivalent to fitting the measured response on a basis whose dimension is equal to the number of sensors and whose span is determined by the sensor positions. The basis fitting perspective makes clear that a necessary condition for accuracy is that the number of sensors be no less than the number of modes that contribute substantially to the estimated quantity. It is shown that low pass filtering of the measured response, using a cutoff frequency in the proximity of the frequency of mode $(m-1)$, where m is the number of sensors, is advisable. Reconstruction by blending the measurements with a nominal model is examined using the Kalman Filter, the RTS Smoother and a new approach designated as the Minimum Norm Response Corrector (MIRC). Results obtained using 3 nonlinear building models and an ensemble of 30 bi-directional earthquake motions suggest that, for the conditions that prevail in practice, (i.e., relatively poor nominal models and possible nonlinearity in the measured response) the MIRC estimator is the most accurate. The gains in accuracy offered by MIRC over the CS are modest for inter-story drift but are significant in story shears. Specifically, the mean of predictions normalized to the true result (based on 1560 story shear histories) proved to be 1.48 for the CS and 1.00 for MIRC.

Introduction

The need to reconstruct the response of systems given a limited number of measurements arises in many fields. In earthquake engineering, in particular, data from instrumented buildings has been used for validating seismic design codes, improving analytical models and evaluating how a motion may have affected the integrity of a structure (Li et al. 1997, De la Llera and Chopra 1995, Ventura et al. 2000 and 2003). The traditional scheme used in building seismic response reconstruction approximates the accelerations at unmeasured levels using interpolation; linear interpolation and cubic splines being two common choices (Lui, Mahin and Mohele 1990, De la Llera and Chopra 1995, Limongelli 2003, Naeim 1997, Naeim et al., 2006). A key limitation of all interpolation schemes, as shall be shown, is the fact that the dimension of the fitting basis is limited by the number of sensors, m . If there are q modes that contribute significantly to a quantity, and $q > m-1$, the results from interpolation will be poor. In this regard it's worth noting that while $q < m-1$ is necessary, it is not a sufficient condition for reconstruction accuracy because the location of the sensors and the nature of the interpolating functions also play a role.

An advantage of model based estimation over basis fitting is the fact that the basis dimension is not determined by the number of sensors. In model based estimation the discrepancies between model predictions and measurements are used to adjust the estimated response at unmeasured coordinates. Model based estimators differ depending on what is known (or assumed) about the source of the observed discrepancies. In control, for example, uncertainties are assumed to come from unmeasured inputs (typically referred to as process noise) and the model is presumed accurate. For these conditions the optimal estimator, if the disturbances are broad band, is the much celebrated Kalman Filter (Kalman 1960). The situation in the seismic response reconstruction problem, however, is one where the majority of the discrepancies come from approximation in the model itself.

An observer designed with the seismic response problem in mind, presented by Hernandez and Bernal (2008), operates by forcing the response to follow the measurements using fictive forces that are collocated with the sensor positions. A generalization of this approach designated as the Minimum Norm Response Corrector (MIRC) was developed in this project. The MIRC algorithm uses fictive forces applied at all coordinates and selects them, from the set of all the possible solutions, as those for which a certain metric related to their magnitude is minimal. An issue that arises when one considers model-based estimation research is deciding on the level of disparity between the “truth model” used to generate the data and the nominal model in the estimator. A realistic simulation of this discrepancy is particularly important in the seismic response reconstruction scenario because model error is likely the main source of uncertainty. In this project it was decided that practicality required the use of linear models, independently of whether the true response was linear or nonlinear.

Reconstruction via Basis Fitting

Let y_m and y_u be the measured and the unmeasured coordinates and let m and u represent the number of coordinates in each set, the total number of coordinates is $n=m+u$. The response can be expressed as

$$\begin{Bmatrix} y_m(t) \\ y_u(t) \end{Bmatrix} = \begin{bmatrix} \Phi_{mm} & \Phi_{mu} \\ \Phi_{um} & \Phi_{uu} \end{bmatrix} \begin{Bmatrix} Y_1(t) \\ Y_2(t) \end{Bmatrix} \quad (1)$$

from where it is a simple matter to show that

$$y_u(t) = \Phi_{um} \Phi_{mm}^{-1} \cdot y_m(t) + (\Phi_{uu} - \Phi_{um} \Phi_{mm}^{-1} \Phi_{mu}) Y_2(t) \quad (2)$$

Since $Y_2(t)$ cannot be computed, the common assumption is to take it equal to zero and predict the response at the unmeasured coordinates using the first term in eq.1. In this approach error is restricted to the unmeasured coordinates and is equal to the second term in Eq.2. As one gathers, the error is anticipated to be of high frequency and to vary along the height of the building according to the norm of the rows of the matrix in the parenthesis. When the second part of Eq.2 is negligible the estimate from part one is sufficiently accurate and all is well. In many

cases, however, error in the accelerations in the upper floors is not negligible and results can be improved notably by low pass filtering the measurements. Adding an f to the subscript of the measurements to indicate that they may be filtered one has

$$y(t) \cong \Psi \cdot y_{mf}(t) \quad (3)$$

where

$$\Psi = \begin{bmatrix} I \\ \Phi_{um} \Phi_{mm}^{-1} \end{bmatrix} \quad (4)$$

If the response is essentially linear the first $m-1$ mode shapes (plus the rigid body mode) provide a “good” fitting basis. A practical approach to estimate these shapes without the need to formulate a detailed model, for buildings with reasonably uniform properties along the height, is to use the mode shapes of a flexural-shear continuum (Miranda and Taghavi 2005; Alimoradi et al. 2006). These shapes are determined by a single parameter that can be estimated from the ratio of natural periods or, with some practice, from experience.

The Cubic Spline

Schemes that reconstruct the response using prescribed interpolating functions are particular versions of the basis fitting approach. We illustrate the matter using the cubic spline interpolator, generalization to other interpolators is apparent from the derivation. The cubic spline interpolation states that the position of points in a building segment defined by any two subsequent sensors is

$$y(z, t) = e(t) + f(t)z + g(t)z^2 + h(t)z^3 \quad (5)$$

where z is the distance measured upwards from the lower sensor and the quadruple $\{e(t), f(t), g(t), h(t)\}$ are time dependent coefficients. Let m be the number of sensors in a given direction; the number of segments is then $m-1$ and the number of constants to be identified at each time station $4(m-1)$. Imposing continuity up to the second derivative at interior points one has $3(m-2)$ constraints, plus the m measurements, yielding a total of $4m-2$ constraints. Counting unknowns and equations one concludes that two additional constraints are needed. These constraints are typically taken as a first derivative = 0 at the base and the roof or first derivative = 0 at the base and second derivative = 0 at the roof, approximations that are reasonable for shear dominated or flexure dominated structures, respectively. Note that discontinuity in the third derivative of the cubic spline at interior nodes is reasonable given that the third derivative is related to shear forces and these suffer abrupt jumps at story levels. Needless to say, discontinuity in the 3rd derivative at the levels located within a segment is not realized.

Let $a(t)$ be the vector of all the coefficients of the cubic spline, namely $\{e(t), f(t), g(t), h(t)\}$ for segment 1 followed by $\{e(t), f(t), g(t), h(t)\}$ for segment 2 etc. Eliminating explicit reference to time for notational simplicity we designate the entries in this vector as a_1, a_2 , etc, with a_1 - a_4 corresponding to the first segment, a_5 - a_8 to the second, and so on. The m equations that relate these coefficients to the measurements can be written as

$$A_1 \cdot a = y_m \quad (6)$$

Note that at interior points one can take the upper or the lower segment to formulate the entries in the A_1 matrix. Selecting the upper segment is simplest since the row entries are zero except for a single value of 1. Needless to say, for the roof measurement one has to use the lower segment so the last row of A_1 has 4 non-zero terms.

Continuity leads to equations of the form $f(a) = 0$. To illustrate assume that there are 3 sensors (base roof and 1 intermediate) so there are two segments. Continuity in displacement, slope and curvature at the interior point gives

$$a_1 + a_2 \ell_1 + a_3 \ell_1^2 + a_4 \ell_1^3 - a_5 = 0 \quad (7)$$

$$a_2 + 2a_3 \ell_1 + 3a_4 \ell_1^2 - a_6 = 0 \quad (8)$$

$$2a_3 + 6a_4 \ell_1 - 2a_7 = 0 \quad (9)$$

where ℓ_1 is the height of the first segment. The $3(m-2)$ continuity equations can be grouped and written as

$$A_2 \cdot a = 0 \quad (10)$$

The boundary conditions are two equations of the form $g(a) = 0$, for example, in the case of zero slope at the roof and the base one has (with notation for the case of two segments)

$$a_2 = 0 \quad (11a)$$

$$a_6 + 2a_7 \ell_2 + 3a_8 \ell_2^3 = 0 \quad (11b)$$

The equations describing the boundary conditions are, therefore

$$A_3 \cdot a = 0 \quad (12)$$

Finally, the response at all floors is linearly related to the coefficients in the vector a so one can write

$$y = A_4 \cdot a \quad (13)$$

Equations 10 and 12 can be combined into

$$\begin{bmatrix} A_2 \\ A_3 \end{bmatrix} \{a\} = \{0\} \quad (14)$$

or, with obvious notation

$$A_{2,3} \cdot a = 0 \quad (15)$$

from where it follows that

$$a = Q \cdot v \quad (16)$$

where

$$Q = \text{null}(A_{2,3}) \quad (17)$$

Substituting the result of Eq.16 into Eq.6 and solving for v one gets

$$v = [A_1 \cdot Q]^{-1} \cdot y_m \quad (18)$$

where it can be shown that the matrix in the bracket is full rank and square. Substituting Eq.18 into Eq.16 and the result into Eq.13 yields

$$y(t) = A_4 Q \cdot [A_1 \cdot Q]^{-1} y_m(t) \quad (19)$$

which shows that the cubic spline interpolation is a particular case of the basis fitting where the matrix $A_4 Q \cdot [A_1 Q]^{-1}$ plays the role of Ψ (see Eq.3). Note that the basis of the CS is dictated by the interpolating function and the position of the sensors so there is no “adaptability” in the scheme. The result in Eq.19 clarifies the CS interpolation scheme and is computationally significant since it shows that there is no need to solve a set of simultaneous equations at each time step (the traditional approach) but it suffices to compute the matrix in Eq.19 (once) and the reconstruction at any time follows from a simple matrix multiplication.

Error Measures

To compare the accuracy of reconstructions obtained with various methods we define the following metrics where y is the true and y_p is the predicted response.

Peak Response Indicators

PRP = $\max [y_p(t)] / \max [y(t)]$ (Peak Response Positive)

PRN = $\min [y_p(t)] / \min [y(t)]$ (Peak Response Negative)

PRA = $\max (\text{PRP}, \text{PRN})$ (Absolute Maximum)

Time History Indicator

Taking $t_0, t_1 =$ as the times when $I_n = 0.1$ and $I_n = 0.9$ are reached, where I_n is

$$I_n(t) = \frac{\int_0^t (\ddot{x}(\tau))^2 d\tau}{\int_0^{t_{\max}} (\ddot{x}(\tau))^2 d\tau} \quad (20)$$

we define a metric that measures the quality of the prediction along the time axis as

$$NRMS = \frac{\sqrt{\frac{1}{t_1 - t_0} \int_{t_0}^{t_1} (y(\tau) - y_p(\tau))^2 d\tau}}{|y(t)|_{\max}} \quad (21)$$

Numerical Illustration of the CS Performance

We illustrate two situations, one where results obtained without filtering are adequate and one where they are not. In both cases we focus on the base shear estimation, which is particularly difficult since it depends on accelerations and these are most affected by higher modes. In the first case we consider a 6 story model with sensors at the base, the roof, and level 3. The fundamental period is 0.65 secs and the excitation is the Parkfield 2004 record (Fault Zone 14). The exact base shear is compared with the CS prediction in Fig.1. As can be seen, the result is accurate.

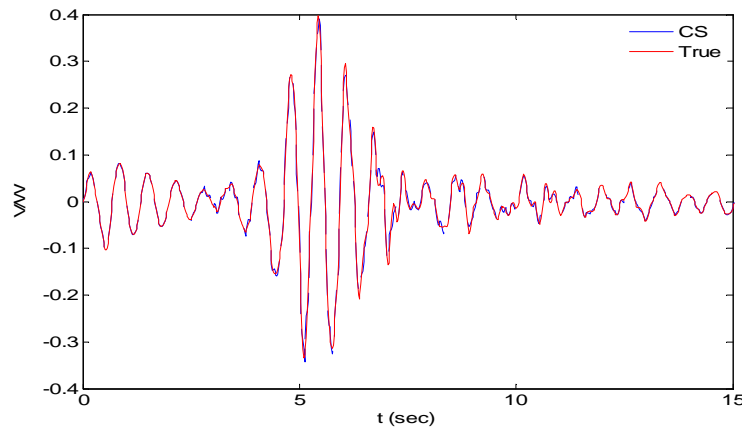


Figure 1. Comparison of the cubic spline estimates base shear and the true values for the 6 story structure under Parkfield 2004

The second example is a 24 story building with sensors at levels 8 and 16 in addition to the base and the roof. The fundamental period is 3 sec and the excitation is the same as before. Fig.2, which compares the exact base shear with the unfiltered CS prediction shows that the results are in this case inaccurate. The high frequency error from the truncated part in Eq.2 is evident.

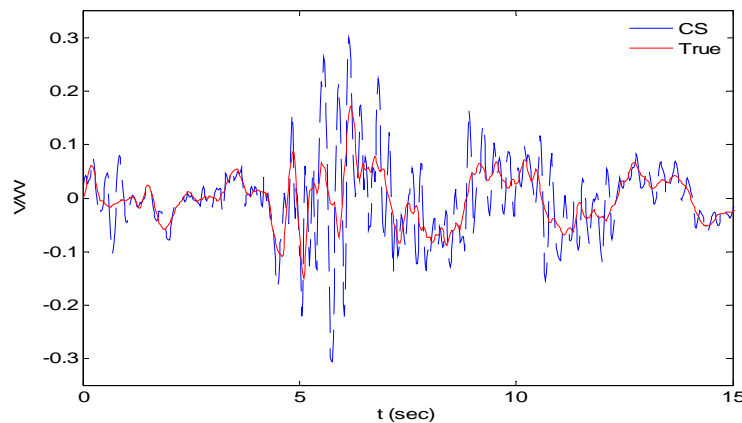


Figure 2. Comparison of the unfiltered cubic spline estimates base shear and the true values for the 24 story structure under Parkfield 2004

Results when a low pass filter with a cutoff frequency at 3 Hz is applied to the measurements are depicted in Fig.3 (the frequency of the 5th mode is 3.07Hz). The post-filter answer is acceptable.

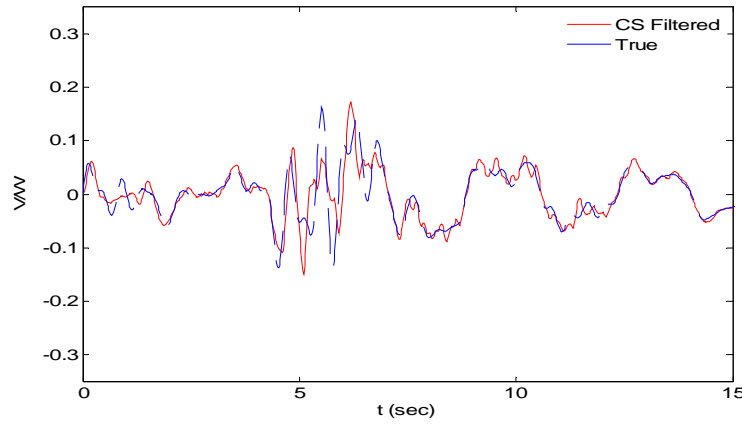


Figure 3. Comparison of the filtered cubic spline estimates base shear and the true values for the 24 story structure under Parkfield 2004

Model Based Estimation

The Kalman Filter

The Kalman Filter (Kalman 1960) is the optimal estimator for linear dynamics and measurement processes with Gaussian unmeasured disturbances and measurement noise. The methodology consists of a forecast step and an updating step in which parameters are adjusted to honor the observations. Let the state and output equations for a linear system be given by

$$x_{k+1} = Ax_k + Bu_k + w_k \quad (22)$$

$$y_k = Cx_k + v_k \quad (23)$$

where x is the state, u is a deterministic input, w are unmeasured disturbances, y is the measured output, v is measurement noise and the triplet $\{A, B, C\}$ are the system matrix, the input to state matrix, and the state to output matrices; w and v are assumed white with covariance matrices $Q_k = E(w_k w_k^T)$ and $R_k = E(v_k v_k^T)$. The expected value of the state at $k=0$ is x_0 and the covariance of the state error at the origin is P_0 . The algorithm proceeds as follows:

1. Move forward

$$\hat{x}_{k+1}^- = A\hat{x}_k^+ + Bu_k \quad (24)$$

2. Compute the covariance of the state error prior to incorporating the information from the measurement

$$P_{k+1}^- = AP_k^+ A^t + Q_k \quad (25)$$

3. Compute the Kalman gain

$$K_{k+1} = P_{k+1}^- C^t (A P_{k+1}^- A^t + R_{k+1})^{-1} \quad (26)$$

4. Update the state using the measurement

$$\hat{x}_{k+1}^+ = \hat{x}_{k+1}^- + K_{k+1} (y_{k+1} - C_{k+1} \hat{x}_{k+1}^-) \quad (27)$$

5. Update the covariance of the state error

$$P_{k+1}^+ = (I - K_{k+1} C) P_{k+1}^- \quad (28)$$

6. Repeat from step#1.

The relation between the system mass, damping and stiffness matrices and the state-space matrices $\{A, B, C\}$ in the previous equations is presented subsequently in Eqs.35-37. As can be seen, in the Kalman filter the discrepancies between the measurements and the model predictions come from the response of the system to the unmeasured input ω_k (and the measurement noise v_k). Note that to apply a Kalman filter the covariance of the process and measurement noise, Q_k and R_k have to be specified. In the seismic reconstruction problem the bulk of the error comes from model approximation and there is no clear basis for selecting Q_k and R_k , indicating that the conditions are not those of the standard Kalman filter problem. In the numerical section we use an ad hoc implementation of the Kalman filter based on $Q = I$ and $R = 0$.

The RTS Smoother

The Kalman filter provides an estimate of the state at time t using measurements up to time t . When one is operating offline it is possible to also use measurements after time t . The schemes that use not only past but also future measurements to estimate the state at time t are known as smoothers. Fixed interval smoothers are smoothers that estimate the state at every time station using the same set of data (a fixed time interval). The RTS smoother is a fixed interval smoother introduced by Rauch et al (1965). The algorithm proceeds as follows:

- Perform a standard Kalman filter estimation and store: $x_{k,f}^-$, $x_{k,f}^+$, $P_{k,f}^-$ and $P_{k,f}^+$, where the subscript f is added to indicate that these are results from the *forward* pass of the Kalman filter.
- Compute the smooth estimate of the state, $x_{k,s}$, as

$$x_{k,s} = x_{k,f}^+ + G_k (x_{k+1,s} - x_{k+1,f}^-) \quad (29)$$

where

$$G_k = P_{k,f}^+ A^T [P_{k+1,f}^-]^{-1} \quad (30)$$

The Minimum Norm Response Corrector (MIRC)

The algorithm presented next is a deterministic scheme that uses pseudo-forces to enforce the measurements. The approach falls in the category of smoothers because the predictions at time t are based on all the measurements (past and future). Let m be the number of measurements, n be the number degrees of freedom and ℓ the number of time steps. Assuming linear behavior the equations of equilibrium for an accurate representation of the structure can be written as

$$(M + \Delta M)\ddot{q} + (C_{dam} + \Delta C_{dam})\dot{q} + (K + \Delta K)q = b_{2d}P_d(t) + b_{2u}P_u(t) \quad (31)$$

where the matrices in the parenthesis are the true matrices and the triple $\{M, C_{dam}, K\}$ are matrices the analyst has selected to represent the system. Implicit in Eq.31 is the fact that we assume the error to be parametric, i.e., that the order of the model is correct. The applied loading is expressed as the sum of two parts: $P_d(t)$, which is known, and a possibly unmeasured component $P_u(t)$, b_{2d} and b_{2u} are the spatial distributions of the known and unmeasured loads and q is a vector containing the response at the degrees of freedom. From Eq.31 one has

$$M\ddot{q} + C_{dam}\dot{q} + Kq = b_{2d}P_d(t) + g(t) \quad (32)$$

where the true corrector $g(t)$ is

$$g(t) = b_{2u}P_u(t) - (\Delta M\ddot{q} + \Delta C_{dam}\dot{q} + \Delta Kq) \quad (33)$$

For any estimated corrector $\hat{g}(t)$ one has

$$M\hat{q} + C_{dam}\hat{q} + K\hat{q} = b_{2d}P_d(t) + \hat{g}(t) \quad (34)$$

If one neglects measurement error it is evident that the corrector $\hat{g}(t)$ must be such that the response from Eq.34 matches the measurements. From inspection of Eq.33 one does not expect the corrector to be zero at any particular coordinate so in MIRC $\hat{g}(t)$ is taken to be potentially non-zero at all coordinates. Since the number of coordinates is larger than the number of measurements infinite corrector loads can be formulated. In MIRC, as shown next, the corrector sequence is selected such that $[\hat{g}_0 \ \hat{g}_1 \ \dots \ \hat{g}_\ell]$ has minimum norm (smallest singular value).

MIRC Algorithm

Here we show only the computational steps on the basis that the measurements are relative velocities, for a more detailed description of the derivation see (Bernal and Nasserri 2009).

1) Form the matrices

$$A = \begin{bmatrix} 0 & I \\ -M^{-1}K & -M^{-1}C_{dam} \end{bmatrix} \quad (35)$$

$$B = \begin{bmatrix} 0 \\ M^{-1}b_{2f} \end{bmatrix} \quad (36)$$

$$C = [0 \quad C_v] \quad (37)$$

where $C \in R^{m \times 2n}$ and $C_v \in R^{m \times n}$ is a matrix of zeros with a 1 in each row at the column position corresponding to the measured coordinate. For example, in a 10 story building with sensors in levels 3 6 and 10

$$C_v = \begin{bmatrix} 0 & 0 & 1 & 0 & 0 & 0 & 0 & 0 & 0 & 0 \\ 0 & 0 & 0 & 0 & 0 & 1 & 0 & 0 & 0 & 0 \\ 0 & 0 & 0 & 0 & 0 & 0 & 0 & 0 & 0 & 1 \end{bmatrix}$$

b_{2f} gives the spatial distribution of the corrective forces, which, the typical MIRC applications is taken as the identity.

2) Compute

$$A_d = e^{A\Delta t} \quad (38)$$

$$B_d = (A_d - I)^2 A^{-2} B \frac{1}{\Delta t} \quad (39)$$

$$D_d = -CA^{-1} \left[I - A^{-1}(A_d - I) \frac{1}{\Delta t} \right] B \quad (40)$$

$$Y_j = CA_d^{j-1} B_d \quad j = 1, 2, \dots, k \quad (41a)$$

$$Y_0 = D_d \quad (41b)$$

and form

$$H_l = \begin{bmatrix} Y_0 & 0 & \dots & 0 \\ Y_1 & Y_0 & \dots & 0 \\ \dots & \dots & \dots & \dots \\ Y_l & Y_{l-1} & \dots & Y_0 \end{bmatrix} \quad (42)$$

with $\Delta t =$ time step.

3) Compute the difference between the measurements and the predictions of the model z_2 (in this presentation assumed to be relative velocities) and place them as columns of the matrix Z , namely

$$Z_l = \text{vec}[z_2(0) \ z_2(1) \ z_2(2) \dots z_2(l)] \quad (43)$$

where vec is an operator that stacks the column of a matrix in a single one.

4) Calculate the corrective loads as

$$F = H_l^{-*} . Z_l \quad (44)$$

where

$$F = \text{vec}[\hat{g}_1 \ \hat{g}_2 \ \hat{g}_3 \ \dots \ \hat{g}_l] \quad (45)$$

Numerical Illustration

Consider the 24 story structure use in the plots of Figs 2 and 3. To reflect error in the model we formulate a nominal model based on a shear-flexural idealization (Miranda and Taghavi 2005) and treat the frame structure as the “truth model”. We adjust the properties of the nominal model so the period of the first mode is correct. The left side of Fig.4 compares the base shear predicted by the model with the true values and the right side illustrates the comparison with the MIRC estimate. In this case the error in the nominal model is not large but the improvement realized by MIRC is evident.

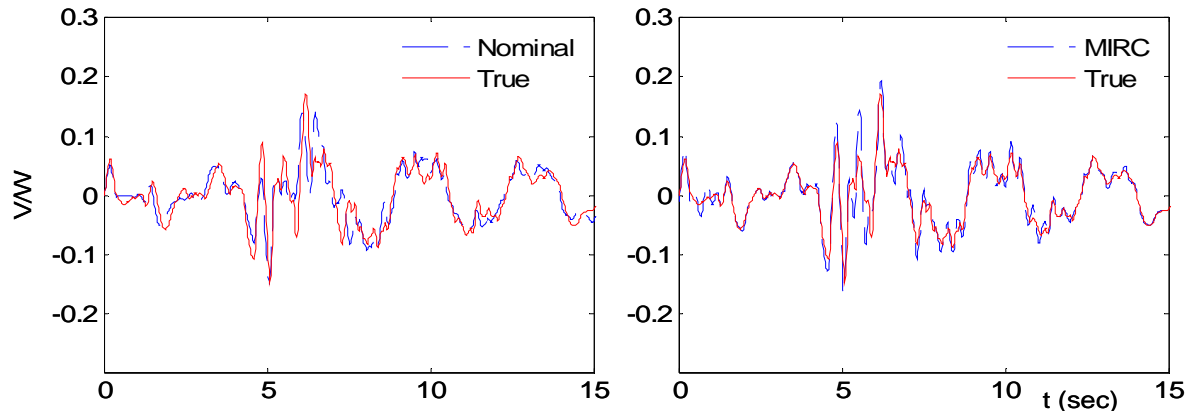


Figure 4. Comparison of the MIRC estimates of the base shear and the true values for the 24 story structure under Parkfield 2004 earthquake

Observation

A consistent approach to compute the story shears when MIRC is used is to take them as the sum of the forces (from the top down) compatible with the displacement response. This procedure is equivalent to computing the shears as the sum of the inertial forces plus the contribution of the fictive corrective forces. Numerical experience has shown, however, that the story shears computed exclusively using the accelerations are generally more accurate and this is how they are computed in the numerical section.

Nonlinear Response

The effect of nonlinearity on the quality of the response reconstruction depends on the estimation method and on whether the nonlinearity produces drastic changes in the dominant shape of the response (i.e., if it is highly concentrated) or not.

Basis Fitting

One expects accuracy to diminish more notably if the nonlinearity is strongly localized. To illustrate, suppose that there is a 2-story structure whose roof and base are instrumented. The CS estimate of the 1st floor is in this case the average of the two measurements. If nonlinearity is restricted to the 1st floor the response will be under-predicted but if it takes place only on the second it will be over predicted. Fig.5 depicts results for the drift in the first level of the 6-story structure used previously for two distributions of the nonlinearity: a) nonlinearity restricted to the 1st level and b) nonlinearity spread throughout the frame. As can be seen, the CS interpolator provides a much better estimation when the nonlinearity is distributed.

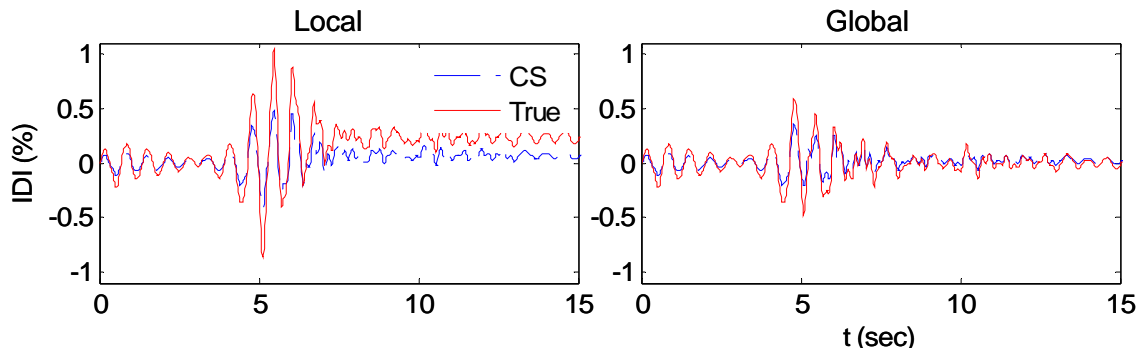


Figure 5. Effects of local and global nonlinearity on the estimation of the 1st story IDI of the 6 story structure.

The MIRC

It is interesting to note that while the MIRC is based on the superposition principle, the response correction based on a linear model can still provide improve estimates of nonlinear response. To illustrate, Fig. 6 shows the MIRC estimates of the 1st floor IDI based on a linear model when the true system response is nonlinear. As can be seen, the MIRC results try to follow the residual displacement.

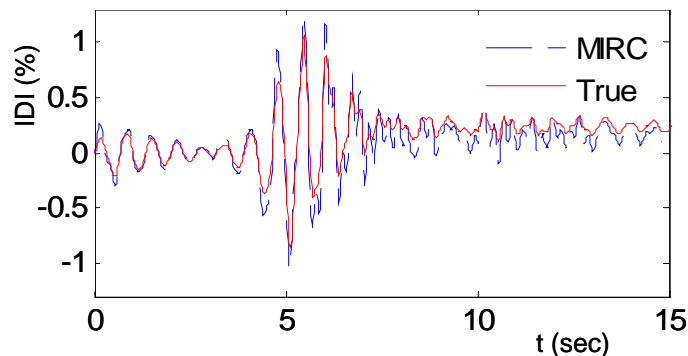


Figure 6: Comparison of the estimates of 1st floor IDI of the 6story nonlinear model using a linear MIRC

Numerical Results

Three dimensional nonlinear models of 3 instrumented buildings were used as surrogates of the real structures. The buildings are the 13 story Sherman Oaks (CSMIP # 24322), the 10 story San Jose building (CSMIP # 57356) and the 6 story Burbank building (CSMIP # 24370). The instrumented levels and other details can be found at (<http://www.strongmotioncenter.org/>). The responses of the nonlinear models to an ensemble of 30 ground motions were treated as the true responses. In the case of model based estimation the nominal model was taken as a linear shear building with properties adjusted to match the first mode period. Since the variation of the error indicators with height is not too significant the data for all floors (for shear and IDI) were treated together. After excluding the shears at the last level (since it is determined by the measured roof acceleration, and the IDI of floors for which there are adjacent sensors) the data set consisted of 1560 histories of story shears and 1260 histories of IDI. The data set was not separated into linear and nonlinear responses because in practice estimators are used without this information. The limits of the range for which the central 80% of the probability distribution function, as defined in Fig.7, are reported in Figs.8 and 9.

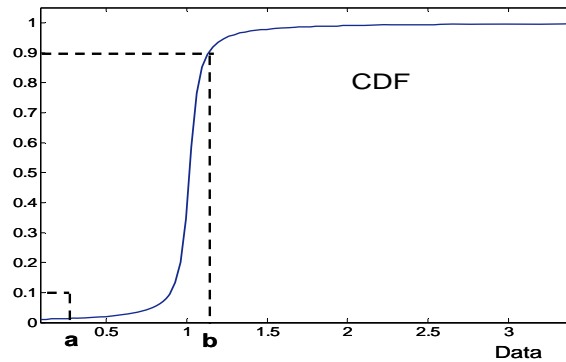


Figure 7: Definition of the parameters a and b that define the central 80% of the probability distribution functions

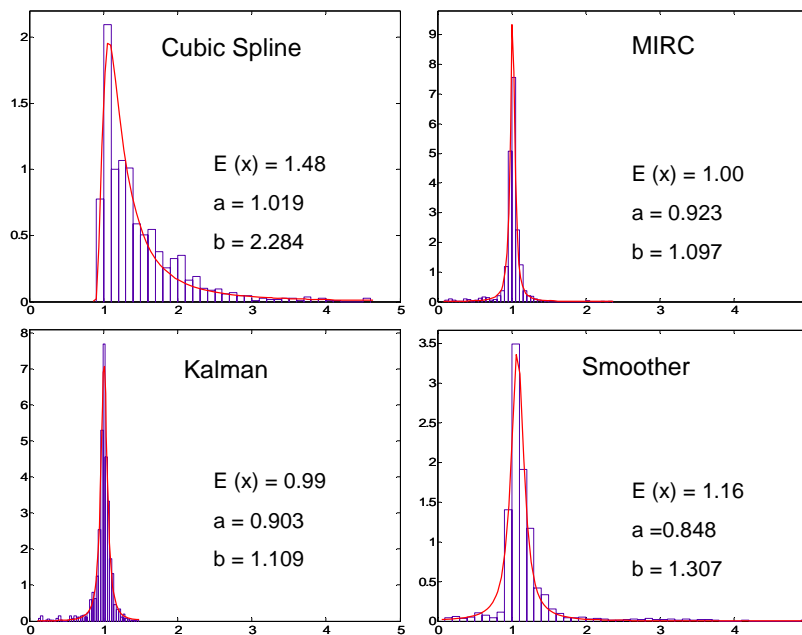


Figure 8: Probability distributions for the PRA of the story shears for various estimators

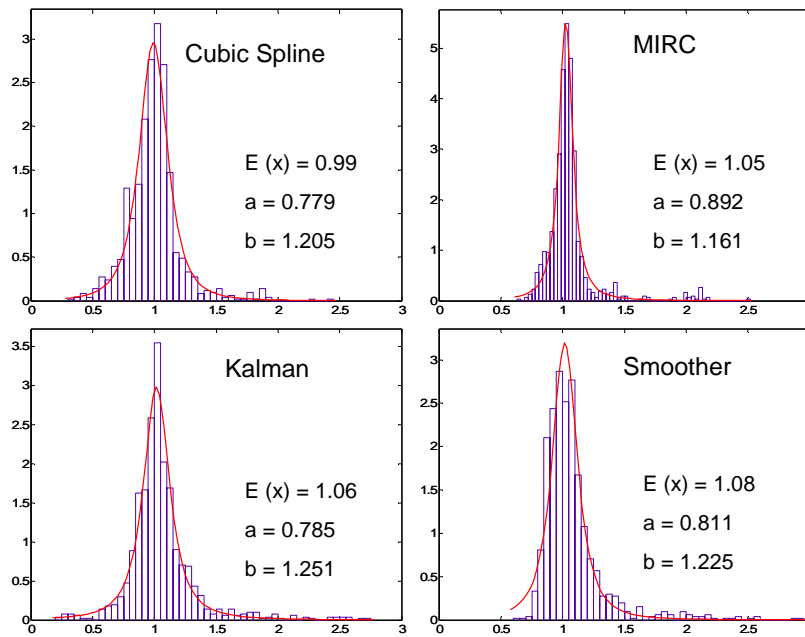


Figure 9: Probability distribution for the PRA of IDI for various estimators

The results shown suggest that the MIRC provides the best estimates. Fig 10 shows the mean and the standard deviation for the NRMS.

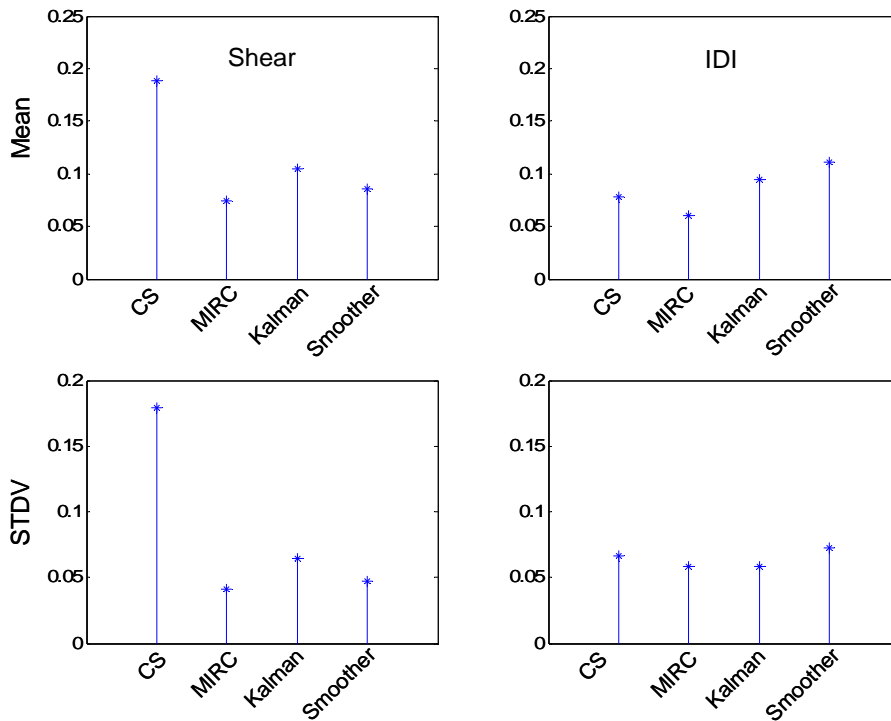


Figure 10: Mean and the STDV of the NRMS of shear and IDI for various estimators

Conclusions

It is shown that the cubic spline reconstruction is a particular case of the basis fitting approach wherein the basis is implicitly selected by the positioning of the sensors. This result clarifies the conditions when the scheme can be expected to give accurate predictions and when it cannot. It is contended, specifically, that the cubic spline interpolation is adequate when the number of modes that contribute to the quantity of interest is less than the number of sensors (not including the base). The result on the basis fitting analogy is computationally significant because it shows that the interpolating coefficients of the spline need not be computed at each time step, as has been done in the traditional implementation. Although not necessary when the contribution of higher modes is negligible, it is shown that low pass filtering of the measurements, prior to obtaining the cubic spline reconstruction, is good practice. Nonlinearity typically reduces the accuracy attained because the truncated basis needed to fit the nonlinear response can differ substantially from the linear one (which is best approximated by the spline basis). Reductions in accuracy are particularly important when the nonlinearity is concentrated in a few levels. When the number of sensors is not sufficient much improved accuracy over the cubic spline can be realized by using estimators that blend the measurements with a nominal model. Of the estimators examined in this study the one that proved most effective reconstructs the response using the nominal model, the ground excitation and a set of fictive forces of minimum norm that enforce the measurements.

The numerical results show that the cubic spline is generally adequate for estimating inter-story drift but tends to over-predict story shears. These observations are anticipated by the theory and derive from the fact that for typical sensor layouts, and typical structures, the number of modes with a significant contribution to drift is smaller than for the accelerations needed to compute story shears. It appears, based on the 1560 histories obtained, that the overestimation of story shears by the spline can be quite significant. Specifically, values in excess of 2 for the ratio of the estimation to the true value were computed in more than 10% of the cases. For the MIRC estimator, in contrast, the threshold separating the largest 10% ratios was only 1.1.

References

- Alimoradi, A., Miranda, E., Taghavi, S. And Naeim, F. (2006). "Evolutionary model identification utilizing coupled shear-flexural response-Implications for multistory buildings. Part 1: Theory", *J. Structural Design of Tall Spec. Buildings*, 15, p.51-65.
- Bernal D., Nasser, A. (2009). "An approach for response reconstruction in seismic applications", *Proceedings of the 3rd International Operational Modal Analysis Conference IOMAC09*, Ancona Italy May 4-6 2009.
- De la Llera, J.C., Chopra, A.K. (1995). "Evaluation of seismic code provisions using strong-motion building records from the 1994 Northridge earthquake.", *SMIP95 Seminar on Seismological and Engineering Implications of Recent Strong-Motion Data*, pp. 25-40.

Hernandez E., and Bernal D. (2008) "State estimation in systems with modal uncertainties", *Journal of Engineering Mechanics*, ASCE , v.134,n.3,pp.1-6. (in press).

Kalman, R.E. (1960), "A new approach to linear filtering and prediction problems", *ASME Journal of Basic Engineering* ,v.82 , n.1, pp. 35-45.

Li, Y. and Mau, S.T., (1997). "Learning from recorded earthquake motion of buildings.", *J. Structural Eng.*, ASCE, v. 123 n. 1, pp. 62-69.

Limongelli, M.P. (2003). "Optimal location of sensors for reconstruction of seismic responses through spline function interpolation", *Earthquake Engineering and Structural Dynamics*, v. 32, pp. 1055-1074.

Lui, R.R., Mahin, S. , Moehle,J. (1990). "Seismic Response and Analytical Modeling of the CSULA Administration Building Subjected to the Whitter Narros Earthquake.", *SMIP 1990 Seminar on Seismological and Engineering Implications of Recent Strong-Motion Data*, pp. 8-1 - 8-10.

Miranda, E. and Taghavi, S., (2005). "Approximate floor acceleration demands in multistory buildings. I:formulations", *J. Structural Eng.*, ASCE, v. 131 n. 2, pp. 203-211.

Naeim, F. (1997), Performance of instrumented buildings during the January 17, 1994 Northridge earthquake—an interactive information system, *Report No. 97-7530.68*, John A. Martin and Associates, Inc..

Naeim, F., Lee, H., Hagie, S., Bhatia, A., Alimoradi, A., and Miranda, E., (2006), "Three dimensional, real time visualization and automated post-earthquake damage assessment of buildings", *Structural Design Tall and Special Buildings*, v.15 , pp. 105-138.

Rauch, H., Tung, F. and Striebel, C., (1965). "Maximum likelihood estimates of linear dynamic systems", *AIAA Journal* v.3, n.8. pp. 1445-1450

Ventura, .C.E. and Ding, Y. 2000. "Linear and nonlinear seismic response of a 52-story steel frame building.", *J. Structural Design of Tall Buildings*, v. 9, n.1, pp. 25-45.

Ventura, C.E. , Laveric, B., Brincker, R. and Andersen, P., 2000. "Comparison of dynamic characteristics of two instrumented tall building." *Proc. 21st Int. Modal Analysis Conference (IMAC)*.

SEISMIC ANALYSIS OF BUILDINGS TO RECORDED MOTIONS: MODELING AND SOFTWARE CHALLENGES

Rakesh K. Goel¹ and Karen Nishimoto²

Department of Civil and Environmental Engineering
California Polytechnic State University, San Luis Obispo

Abstract

This investigation focused on developing an improved understanding of challenges associated with computation of nonlinear response of three-dimensional building to recorded ground motions, and if the inertial base shear is an accurate indicator of the true base shear. For this purpose, three-dimensional models of two buildings – one reinforced-concrete building and one steel building – are developed in *OpenSees* and *Perform3D*. The analysis of these models included pushover analysis for lateral force distribution proportional to the first mode in each of the two principle directions, and RHA to compute response for 30 ground motions recorded during past earthquakes. It was found that modeling assumptions as well as different software may lead to significantly different pushover curves: concentrated plasticity model leads to lower strength, early initiation of yielding, and post yielding strength loss in pushover curves compared to spread plasticity model, strength loss model for beams/columns leads to significant post yielding strength loss in the pushover curve, and differences in solution schemes and convergence criteria available in different software programs also affect the pushover curves. It was also found that there prediction of median peak response from different software can differ from 10% to 40%. Finally, the median inertial base shear exceeds the true base shear by 10% to 20% with the value exceeding by as much as 50% for individual earthquake and even a small time delay between different recording channels may lead to significant error in the inertial base shear. Therefore, inertial base shear should be used with caution as an estimate of the true base shear.

Introduction

Buildings are typically instrumented with accelerometers at selected number of floors: low-rise buildings (1 to 3 stories) at every floor; and mid- and high-rise buildings at base, roof, and a few intermediate floors. The raw (or uncorrected) acceleration recorded during earthquakes from these accelerometers are processed using well-established procedures to obtain base-line corrected (or processed) accelerations, velocity, and displacements. The processed floor accelerations and displacements may be used to estimate additional engineering demand parameters such as inter-story drift ratio defined as the differential displacement between two adjacent floors divided by the story height, and base shear defined as the summation of floor inertial forces above the base; the floor inertial forces are computed as the product of floor acceleration and floor mass. The engineering demand parameters thus estimated from recorded

¹ Professor and Chair

² Former Graduate Student

motions of buildings may be compared to those computed from various analytical procedures, such as nonlinear static pushover and nonlinear response history analysis, to evaluate the accuracy of these analytical procedures. These parameters may also be compared with limiting values to check if the building suffered damage during an earthquake and may need detailed inspection/evaluation.

For buildings with limited number of instrumented floors, estimation of various engineering demand parameters requires that the motions at non-instrumented floors be interpolated from those available at the instrumented floors. Typically, a piece-wise cubic polynomial interpolation procedure is used for conventional buildings (Naeim, 1997; De la Llera and Chopra, 1998; Goel, 2005, 2007; Limongelli, 2003) and a combination of cubic-linear interpolation is recommended for base-isolated buildings (Naeim, et al., 2004). It is generally believed that such interpolation procedures provide reasonable estimates of motions at non-instrumented floors (Naeim, 1997; Naeim et al., 2004; De la Llera and Chopra, 1998).

A recent study by Goel (2008) re-examined the adequacy of the traditionally used cubic polynomial interpolation procedure. It was found that results from the cubic polynomial interpolation procedure are sensitive to location of instrumented floors. While the cubic polynomial interpolation procedure may provide good estimate of floor displacements with proper selection of instrumented floors, this procedure may not accurately predict inter-story drifts and floor accelerations. This finding was also confirmed by Bernal (2007).

Another investigation by Goel and Chadwell (2007) compared the base shear estimated from motions interpolated using the traditional cubic polynomial interpolation procedure with the base shear capacity estimated from nonlinear pushover analysis of buildings. It was found that the base shear estimated from interpolated motions significantly exceeded the base shear capacity for several buildings. However, post earthquake inspection of these buildings did not reveal significant damage. This indicates that such base shear estimates may be questionable and possibly unreliable.

The preceding discussion clearly indicates that there is a need to comprehensively re-evaluate existing interpolation procedures. In particular, it is desirable to establish the level of accuracy that can be achieved in estimates of floor displacements and floor accelerations. Furthermore, it is necessary to examine if the base shear estimated from inertial floor forces is an accurate estimate of the “true” base shear which is defined as summation of shear forces in all columns at the base.

The aforementioned evaluation of interpolation procedures requires that “true” motions of buildings be available at each floor level. Since buildings are rarely instrumented at all floors and thus complete set of recorded responses that is needed for evaluating interpolation procedures is not readily available, response of buildings due to recorded ground motions computed from response history analysis (RHA) offers a viable alternative to recorded motions. However, there are several modeling and software challenges in implementing the RHA for buildings that are expected to be deformed beyond the linear elastic limit during strong ground shaking.

The primary objective of this investigation is to develop an improved understanding of challenges associated with computation of nonlinear response of three-dimensional building to recorded ground motions. Another objective is to evaluate the accuracy of the inertial base shear as an indicator of the true base shear using the results from the RHA. For this purpose, nonlinear response – floor displacements, floor accelerations, and base shear – of two buildings – 20-Story Reinforced Concrete Hotel in North Hollywood, and 19-Story Steel Office Building in Los Angeles – were computed from RHA for 30 ground motions recorded during past earthquakes using two different computer program – *OpenSees* and *Perform3D*. Also computed were the pushover curves of these buildings included pushover analysis for lateral force distribution proportional to the first mode in each of the two principal directions. First, challenges associated in computation of nonlinear response from the two computer programs are documented. Next differences in peak responses from the two programs are examined for effects of modeling and software. Finally, peak values of inertial and true base shears are compared to understand if the inertial base shear can provide accurate estimate of true base shear.

Selected Buildings and Ground Motions

Two buildings – 20-Story Hotel in North Hollywood and 19 Story Office Building in Los Angeles – are selected in this investigation (Table 1). This buildings are selected as representative of instrumented mid- to high-rise reinforced-concrete and steel buildings in California.

Table 1. Five concrete buildings selected.

Buildings name	CSMIP Station	Number of Stories	Structural System
Los Angeles – 19-Story Office Building	24643	19/4	Steel Concentric Brace Frame (Transverse) and Moment Frames (Longitudinal)
North Hollywood – 20-Story Hotel	24464	20/1	Concrete Moment Frames

A suite of 30 ground motions have been selected in this investigation (Table 2). Each ground motion consists of a pair of two horizontal components of ground motion recorded during indicated earthquake. These earthquakes are selected for a wide range of parameters: proximity to the fault, magnitude, peak ground accelerations and velocities. These ground motions were not selected to match any design spectrum but to ensure that they will induce different levels of inelastic behavior in the selected buildings: selected buildings are expected to remain within the linear elastic range for a few earthquakes where as these buildings are expected to be deformed well into the nonlinear range, and possibly collapse, during other earthquakes.

Analytical Models

The three-dimensional analytical models of the selected buildings were developed using the structural analysis software Open System for Earthquakes Engineering Simulation (*OpenSees*) (McKenna and Fenves, 2001) and *Perform3D* (CSI, 2006). Following is a description of the modeling procedures.

SMIP09 Seminar Proceedings

Table 2. Selected ground motions.

Serial No.	Station Name	Earthquake	Mag.	Epic. Dist. (km)	PGA (H1, H2, V) - g	PGV (H1, H2, V) - cm/s
1	Parkfield-Fault Zone 1	Parkfield, September 28, 2004	6.0	9	0.59, 0.82, 0.26	63, 81, 10
2	Parkfield-Fault Zone 14	Parkfield, September 28, 2004	6.0	12	1.31, 0.54, 0.56	83, 42, 23
3	Templeton-1-story Hospital GF	San Simeon, December 22, 2003	6.5	38	0.42, 0.46, 0.26	33, 27, 16
4	Amboy	Hector Mine, October 16, 1999	7.1	48	0.15, 0.18, 0.13	20, 27, 12
5	Taiwan-CHY028	Chi-Chi, September 21, 1999	7.6	7 to fault	0.82, 0.65, 0.34	67, 72, 36
6	Taiwan-TCU129	Chi-Chi, September 21, 1999	7.6	1 to fault	0.63, 1.01, 0.34	36, 60, 35
7	Taiwan-TCU068	Chi-Chi, September 21, 1999	7.6	1 to fault	0.46, 0.56, 0.49	176, 263, 187
8	Taiwan-CHY028	Chi-Chi, September 21, 1999	7.6	10 to fault	0.42, 1.16, 0.34	46, 115, 25
9	Sylmar-County Hospital Lot	Northridge, January 17, 1994	6.7	16	0.59, 0.83, 0.53	77, 129, 19
10	Newhall-LA County Fire Station	Northridge, January 17, 1994	6.7	20	0.57, 0.58, 0.54	75, 95, 31
11	Los Angeles-Rinaldi Rec. Station FF	Northridge, January 17, 1994	6.7	9	0.47, 0.83, 0.83	166, 73, 51
12	Santa Monica-City Hall Grounds	Northridge, January 17, 1994	6.7	23	0.88, 0.37, 0.23	42, 25, 14
13	Lucerne Valley	Landers, June 28, 1992	7.4	1 to fault	0.72, 0.78, 0.82	98, 32, 46
14	Yermo-Fire Station	Landers, June 28, 1992	7.4	84	0.15, 0.24, 0.13	29, 51, 13
15	Big Bear Lake-Civic Center Grounds	Big Bear, June 28, 1992	6.5	11	0.48, 0.55, 0.19	28, 34, 11
16	Petrolia-Fire Station	Cape Mendocino, April 26, 1992	6.6	35	0.59, 0.43, 0.15	61, 30, 13
17	Petrolia-Fire Station	Petrolia, April 25, 1992	7.1	8	0.65, 0.58, 0.16	90, 48, 21
18	Cape Medocino	Petrolia, April 25, 1992	7.1	11	1.04, 1.50, 0.75	41, 126, 60
19	Rio Dell-Hwy101/Painter Street Overpass FF	Petrolia, April 25, 1992	7.1	18	0.39, 0.55, 0.20	45, 43, 10
20	Corralitos-Eureka Canyon Road	Loma Prieta, October 17, 1989	7.0	7	0.48, 0.63, 0.44	48, 55, 19
21	Los Gatos-Linahan Dam Left Abutment	Loma Prieta, October 17, 1989	7.0	19	0.40, 0.44, 0.13	95, 84, 26
22	Saratoga-Aloha Ave.	Loma Prieta, October 17, 1989	7.0	4	0.32, 0.49, 0.35	44, 41, 26
23	El Centro-Imperial County Center Grounds	Superstition Hills, November 24, 1987	6.6	36	0.26, 0.34, 0.12	41, 47, 8
24	Los Angeles-Obregon Park	Whittier, October 1, 1987	6.1	10	0.43, 0.41, 0.13	22, 13, 5
25	Chalfant-Zack Ranch	Chafant Valley, July 21, 1986	6.4	14	0.40, 0.44, 0.30	43, 36, 12
26	El Centro-Array #6	Imperial Valley, October 15, 1979	6.6	1 to fault	0.43, 0.37, 0.17	109, 63, 56
27	El Centro-Array #7	Imperial Valley, October 15, 1979	6.6	1 to fault	0.45, 0.33, 0.50	108, 45, 26
28	El Centro-Imperial County Center Grounds	Imperial Valley, October 15, 1979	6.6	28	0.24, 0.21, 0.24	64, 36, 17
29	El Centro-Hwy8/Meloland Overpass FF	Imperial Valley, October 15, 1979	6.6	19	0.31, 0.29, 0.23	72, 91, 29
30	El Centro-Irrigation District	El Centro, May 18, 1940	6.9	17	0.34, 0.21, 0.21	33, 37, 11

20-Story Hotel in North Hollywood

OpenSees Model

The beams and columns for the North Hollywood Hotel were modeled with *beamWithHinges* element in *OpenSees*. This element used fiber section containing confined concrete, unconfined concrete, and steel reinforcing bars. The stress-strain behavior of concrete, both confined and unconfined, was modeled with several different available concrete materials in *OpenSees*. The first concrete material model used in this investigation is *Concrete01* (Figure 1a) which has residual strength after crushing strain. The second model is a modified version of the *Concrete01* model (Figure 1b) which has no residual strength after reaching crushing strain. Further details of these two material models are available in Mander et al. (1988) and Karson and Jirsa (1969). The third concrete model is *Concrete04* which is similar to the modified *Concrete01* model but uses slightly different parameters (see Popovics, 1973 for details). The crushing strain of the unconfined concrete was selected to be equal to 0.004 and that for confined concrete was selected to be that corresponding to the rupture of confining steel using the well established Mander model (Mander et al., 1988). The stress-strain behavior of steel was modeled with *ReinforcingSteel* material in *OpenSees* (Figure 1c). The strength of concrete and steel was selected based on the values specified in the structural drawings. The P-Delta effects were included in the pushover analysis by applying the gravity loads prior to pushover analysis or RHA.

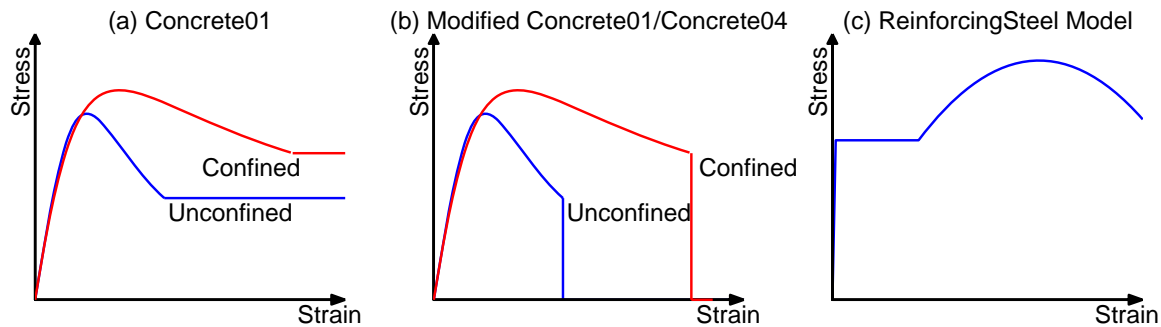


Figure 1. *OpenSees* material models: (a) *Concrete01* model; (b) Modified *Concrete01* and *Concrete04* models; and (c) *ReinforcingSteel* model.

Perfrom3D Model

In the *Perfrom3D* model, beams were modeled with FEMA Concrete Beam with strength loss and unsymmetrical section strength, columns were modeled with FEMA Concrete Column with strength loss and symmetrical section strength, and shear walls were modeled with linear elastic column elements. The FEMA Beam element requires moment-plastic-rotation relationship of Figure 2a. The yield moment of the beam section needed to define the FEMA force-deformation behavior is computed from section moment-curvature analysis using computer program *XTRACT* (TRC, 2008).

The plastic rotation values and the residual strength needed for the FEMA Concrete Beam model in *Perfrom3D* are selected as per FEMA-356 (ASCE, 2000) recommendations: plastic rotations are selected as 0.02 for point U and 0.03 for point X, and the residual strength

for points R and X are selected as 20% of the yield moment (Figure 2a). The plastic rotation value for point R is selected as 0.022 to model gradual strength loss between points U and R.

The FEMA Concrete Column with strength loss element requires moment-plastic-rotation behavior of Figure (2a), P-M interaction diagram for bending about axis-2 and axis-3 (Figure 2b), and M-M interaction diagram between moments about axis-2 and axis-3 (Figure 2c). The yield moment needed to define the force-deformation behavior (Figure 2a) was obtained from *XTRACT* moment-curvature analyses of column sections about axis-2 and axis-3. Similarly, the parameters needed to define P-M interaction diagrams about axis-2 and axis-3 (Figure 2b) were estimated from *XTRACT* P-M interaction analyses of columns sections. The shapes of the P-M interaction diagrams (Figure 2b) and M-M interaction diagram (Figure 2c) were defined using default values of various exponents in *Perform3D*. The material models used for columns in *XTRACT* analysis were the same as for beams.

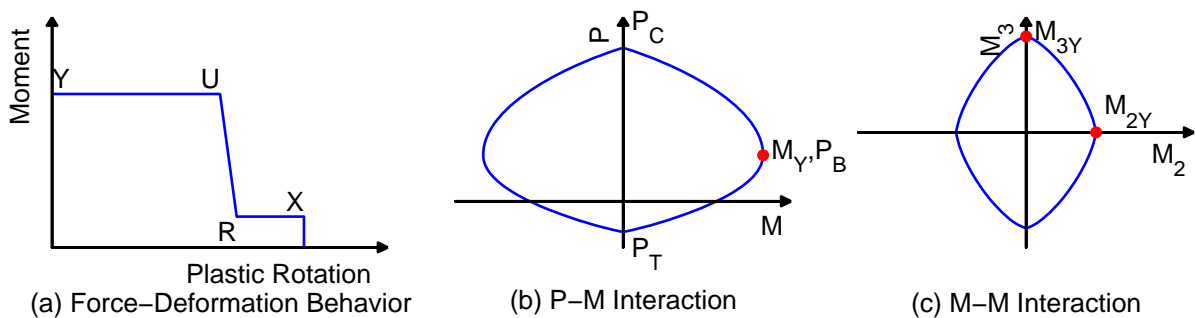


Figure 2. FEMA concrete beam/column element in *Perform3D*: (a) Force-deformation behavior of beam or column, (b) P-M interaction diagram for column; and (c) M-M interaction diagram for column.

Similar to the beams, the plastic rotation values and the residual strength needed for the FEMA Concrete Column model in *Perform3D* are selected as per FEMA-356 recommendations: plastic rotations are selected as 0.02 for point U and 0.03 for point X, and the residual strength for points R and X are selected as 20% of the yield moment (Figure 2a). The plastic rotation value for point R is selected as 0.022 to model gradual strength loss between points U and R.

19-Story Office Building in Los Angeles

OpenSees Model

In *OpenSees* model of the Los Angeles building, the beams and columns were modeled with *nonlinearBeamColumn* elements, and braces were modeled with nonlinear *truss* elements between 1st floor and roof; and beams, columns, and shear walls were modeled with linear *elasticBeamColumn* elements and braces were modeled with linear *truss* elements in the basement. The *nonlinearBeamColumn* element used fiber steel sections with stress-strain behavior of steel fibers modeled with *ReinforcingSteel* material in *OpenSees* (Figure 1c). The nonlinear *truss* elements were modeled with *Hysteretic* material in *OpenSees* (Figure 3). This material model assumed that the stress linearly reduces to zero from the buckling stress at strain value equal to twice the buckling strain; the buckling stress was computed from Euler's Buckling stress formulation. It is useful to note that *OpenSees* does not have an explicit buckling model for steel braces; the buckling options in the *ReinforcingSteel* material are designed only for

reinforcing bars in reinforced-concrete beams and columns and can not be conveniently used for steel braces.

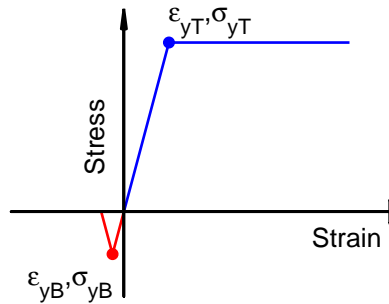


Figure 3. *OpenSees* material model for nonlinear *truss* element.

Perfrom3D Model

In the *Perfrom3D* model of the Los Angeles building, beams were modeled with FEMA Steel Beam with strength loss and symmetrical section strength, columns were modeled with FEMA Steel Column with strength loss and symmetrical section strength, shear walls were modeled with linear elastic column elements, and braces were modeled with Simple Bar element. The material properties for braces were specified by Inelastic Steel Buckling material in *Perfrom3D*. The FEMA Steel Beam element requires moment-plastic-rotation relationship of Figure 4a. The yield moment of the steel beam section was computed automatically by *Perfrom3D* using section properties and steel strength. The plastic rotation values and the residual strength needed for the FEMA Steel Beam model in *Perfrom3D* are selected as per FEMA-356 recommendations: plastic rotations are selected as $9\theta_y$ for point U and $11\theta_y$ for point X in which θ_y is the yield rotation, and the residual strength for points R and X are selected as 60% of the yield moment (Figure 4a). The plastic rotation value for point R is selected as $9.5\theta_y$ to model gradual strength loss between points U and R.

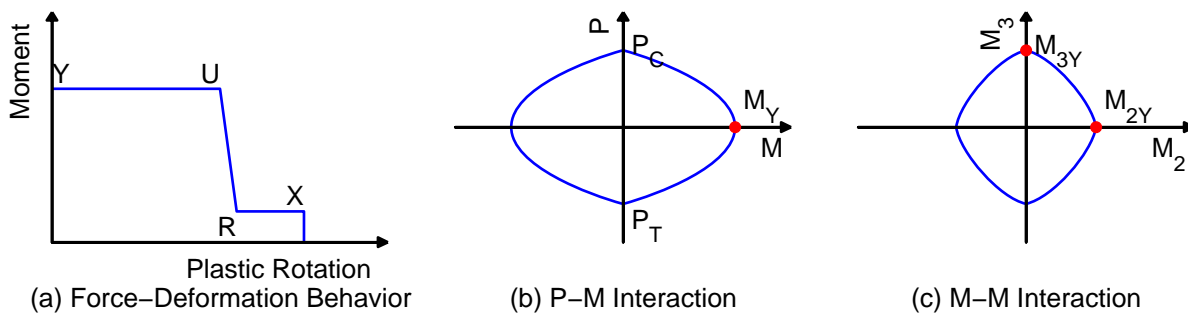


Figure 4. FEMA steel beam/column element in *Perfrom3D*: (a) Force-deformation behavior of beam or column, (b) P-M interaction diagram for column; and (c) M-M interaction diagram for column.

The FEMA Steel Column with strength loss element requires moment-plastic-rotation behavior of Figure (4a), P-M interaction diagram for bending about axis-2 and axis-3 (Figure 4b), and M-M interaction diagram between moments about axis-2 and axis-3 (Figure 4c). The yield moment needed to define the force-deformation behavior (Figure 4a) was automatically

computed by *Perform3D* based on section properties and material strength. Similar to the beams, the plastic rotation values and the residual strength needed for the FEMA Steel Column model in *Perform3D* are selected as per FEMA-356 recommendations: plastic rotations are selected as $9\theta_y$ for point U and $11\theta_y$ for point X in which θ_y is the yield rotation, and the residual strength for points R and X are selected as 60% of the yield moment (Figure 4a). The shapes of the P-M interaction diagrams (Figure 4b) and M-M interaction diagram (Figure 4c) were also automatically generated in *Perform3D* based on the specified section properties and material strength.

Pushover Curves

Pushover curves for the selected buildings were developed for transverse and longitudinal direction using height-wise distribution of lateral loads proportional to the first mode in each direction.

20-Story Hotel in North Hollywood

Figure 5 compares the pushover curves for the North Hollywood Hotel computed from *OpenSees* and *Perform3D*. This comparison indicates that the two programs lead to pushover curves that may differ significantly. The two programs provide essentially identical pushover curves for first transverse and longitudinal modes in the initial elastic region (Figures 5a and 5b). Thereafter, the pushover curves from the two programs differ significantly. The pushover curves from *Perform3D* exhibit early initiation of nonlinear action, much lower yield strength, and significant post yielding strength loss compared to the pushover curves from *OpenSees* (Figures 5a and 5b). This is the case because *Perform3D* used FEMA-356 models for force-deformation behavior of beams and columns with strength loss (see Figure 2a) whereas *OpenSees* used fiber section models for beams and columns with concrete and steel material properties defined by Figure 1a and 1c, respectively. As elements begin to yield and lose strength during pushover analysis, pushover curves from *Perform3D* would begin to yield earlier, would have lower strength, and would show strength loss as more and more elements are deformed beyond point U on the force-deformation relationship (see Figure 2a). On the other hand, the elements in the *OpenSees* model continue to support the load because of gradual spread of plasticity over the member fiber section.

One major concern with the original *OpenSees* model is that the concrete model (*Concrete01*) did not adequately represent concrete crushing, i.e., the concrete fibers continue to support stresses even after crushing strain (see Figure 1a). Therefore, two other material models were considered that adequately address this issue: a modified version of *Concrete01* and *Concrete04* material model with no residual strength after crushing strain (see Figure 1b). The pushover curves were generated from *OpenSees* with these two additional material models and are compared in Figure 6 with those from the original model. These results indicate that the concrete material model has minimal effect on the pushover curves as the pushover curves for all material models are essentially identical.

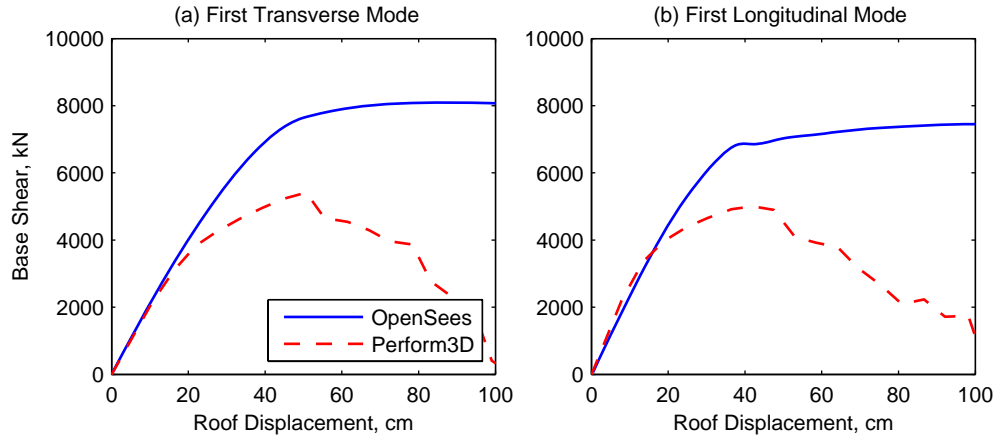


Figure 5. Comparison of pushover curves from *OpenSees* and *Perform3D* for 20-Story Hotel in North Hollywood.

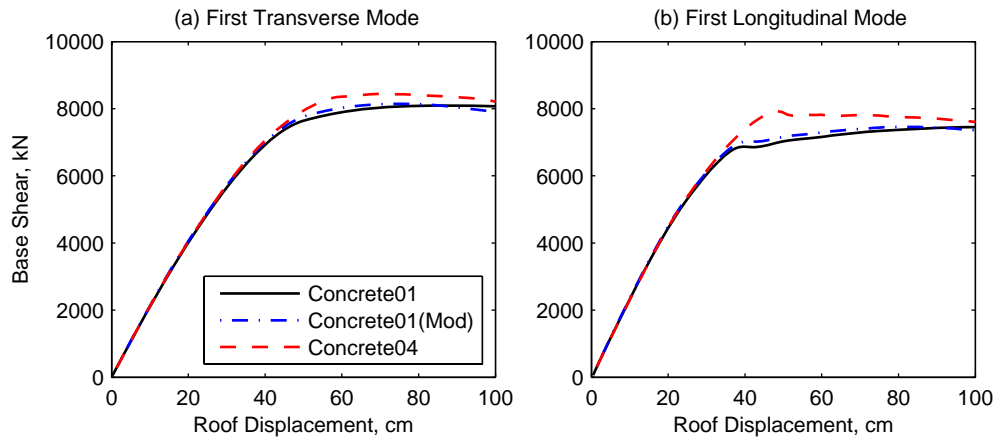


Figure 6. Comparison of “modal” pushover curves from *OpenSees* for three different concrete material models – *Concrete01*, modified *Concrete01*, and *Concrete04* – for 20-Story Hotel in North Hollywood.

Since the original *Perform3D* model modeled beams and columns with strength loss, which is quite different from the *OpenSees* modeling, a second *Perform3D* model was developed in which no strength loss was considered, i.e., the moment in the force-deformation behavior of beams and columns retained the yield moment value even after point *U* (Figure 2a). The pushover curves from the revised *Perform3D* model are compared in Figure 7 with those from the *OpenSees* model. These results indicate that pushover curves from *Perform3D* exhibit lower strength in several modes but no strength loss when compared to pushover curves from *OpenSees* (Figures 7a and 7b).

The results of Figure 7 also lead to another important observation: the models based on concentrated plasticity may lead to lower estimate of building strength than models based on spread plasticity. It is useful to recall that *Perform3D* model is based on concentrated plasticity as it uses a concentrated hinge at the beam-column ends and elastic behavior in-between. The *OpenSees* model on the other hand is a spread plasticity model as the nonlinear action spreads

gradually across the beam-column section as material fibers undergo increasing stresses and strains.

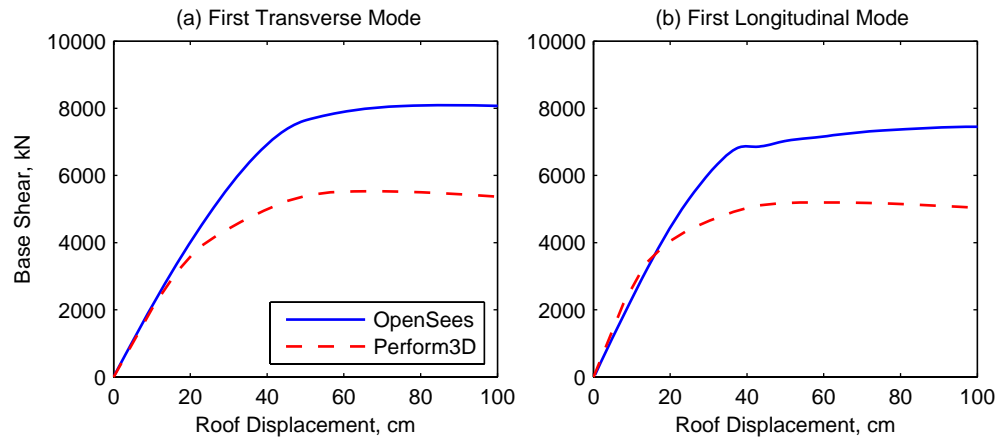


Figure 7. Comparison of pushover curves from *OpenSees* and *Perform3D* for 20-Story Hotel in North Hollywood; *Perform3D* results are using no strength loss model for beams and columns.

19-Story Office Building in Los Angeles

Figure 8 compares the pushover curves for the Los Angeles Office Building computed from *OpenSees* and *Perform3D*. It is useful to recall that the lateral load resisting system in this building consists of steel moment resisting frames in the longitudinal direction and concentric braced frames in the transverse direction. This comparison also indicates that the two programs lead to pushover curves that differ significantly. In the transverse direction, the direction in which lateral load resisting system consists of concentric braced frames, *Perform3D* provides pushover curves that has slightly lower strength and much earlier initiation of nonlinear action compared to the curves from *OpenSees* (Figures 8a). The pushover curve from *Perform3D* also exhibits post yield strength loss whereas that from *OpenSees* does not show strength loss (Figure 8a).

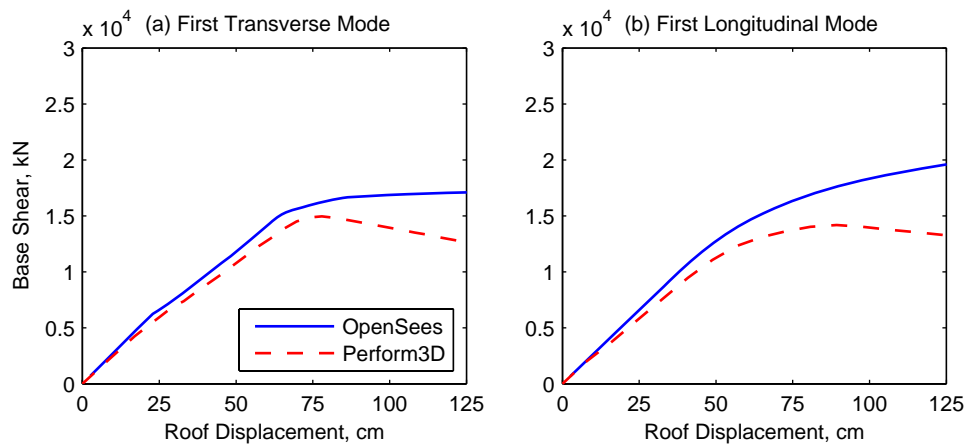


Figure 8. Comparison of “modal” pushover curves from *OpenSees* and *Perform3D* for 19-Story Office Building in Los Angeles.

In the longitudinal direction, the direction in which lateral load resisting system consists of moment resisting frames, *Perform3D* led to pushover curves with lower strength and earlier initiation of nonlinear action compared to *OpenSees* (Figures 8b). The pushover curve from *Perform3D* also exhibits post yielding strength loss (Figure 8b). As noted previously for the North Hollywood building, these differences in the longitudinal pushover curves are due to different modeling assumptions in the two programs: *Perform3D* used FEMA-356 models for force-deformation behavior of beams and columns with strength loss (see Figures 3a) whereas *OpenSees* used fiber section models for beams and columns with concrete and steel material properties defined by Figure 1c, respectively.

Effects of Modeling Assumptions and Software on Pushover Curves

The results presented so far indicate that modeling assumptions may significantly affect the pushover curves: (1) The concentrated plasticity model leads to lower strength, early initiation of yielding, and post yielding strength loss in pushover curves compared to spread plasticity model; and (2) Consideration of strength loss in beam/column model leads to significant strength loss in the pushover curve. The concrete material model, on the other hand, appears to have minimal effect on the pushover curves of reinforced concrete buildings.

The pushover curves may also depend on the software that is used for analysis. While most of the differences may be attributed to differences in modeling options available in different programs (e.g., *OpenSees* does not have an option for modeling FEMA-356 force-deformation behavior with strength loss whereas *Perform3D* does), some differences may also occur due to differences in solution schemes and convergence criteria.

Comparison of Peaks Responses from RHA

Responses – floor displacements, floor accelerations, and base shear – of the two selected buildings were computed for selected ground motions using *OpenSees* and *Perform3D*. It is useful to note that selected buildings experienced excessive deformation due to several of the ground motions in this suite and collapsed for these motions. For example, the North Hollywood Hotel collapsed for ground motions number 7 to 11, 13, 17, 18, 21, and 26, 29. The Los Angeles Buildings collapsed due to ground motions number 5 to 11, 13, 17, 18, and 26 to 29.

The following difficulties were encountered during RHA of the two selected buildings. First, *OpenSees* experienced significantly more convergence problem compared to *Perform3D*. While *Perform3D* failed to converge only for cases where the building collapsed, *OpenSees* failed to converge even for some cases where the building is not expected to collapse. For these cases, *OpenSees* failed to converge even when different solution strategies were used. It is useful to note that *OpenSees* models of the two selected buildings are much more complex compared to *Perform3D* models; *OpenSees* models used fiber section modeling whereas *Perform3D* used concentrated plasticity modeling for beams and columns.

The differences in the peak floor displacements, accelerations, and base shear from the two programs are investigated next by examining height-wise variation of the ratio of peak floor displacements, u_{OS}/u_{P3D} , peak floor accelerations, a_{OS}/a_{P3D} , and peak base shear, V_{OS}/V_{P3D} , from *OpenSees* and *Perform3D*. The results are presented in Figures 12 to 17 for earthquakes for

which the building did not collapse. The results for the North Hollywood Hotel are for the *OpenSees* model which used *Concrete01* material model with residual strength and *Perform3D* model with beams and columns modeled with FEMA-356 force-deformation behavior with strength loss. The other two concrete models – *Concrete01* without residual strength and *Concrete04* model – led to responses similar to the *Concrete01* material model with residual strength when the solution converged. However, *OpenSees* model with these two concrete materials experienced much more convergence problem compared to the model with *Concrete01* material with residual strength. The results for the Los Angeles Building are for the *OpenSees* Model with *Hysteretic* steel material for braces to capture post-buckling strength loss and for the *Perform3D* model with beams and columns modeled with FEMA-356 force-deformation behavior with strength loss.

The presented results include variation of the ratios for individual earthquakes along with the median values and median plus/minus one standard deviation. Median is an indicator of *OpenSees* over or under predicting response compared to *Perform3D* whereas the band formed by median plus/minus one standard deviation is an indicator of the dispersion in the response prediction.

20-Story Hotel in North Hollywood

The median of displacement ratios in Figure 9 for the North Hollywood Hotel indicates that *OpenSees* tends to provide larger estimate of displacements in lower and upper floors and about the same estimates of displacements in middle floors compared to the *Perform3D*. The difference in median value of the displacement ratio in upper and lower floors varies from 1.1 to 1.4 indicating that the response from the two programs can differ by 10% to 40%. The width of the median+ σ or median- σ band is about 0.15 implying that there is about 15% dispersion in the response prediction from the two programs.

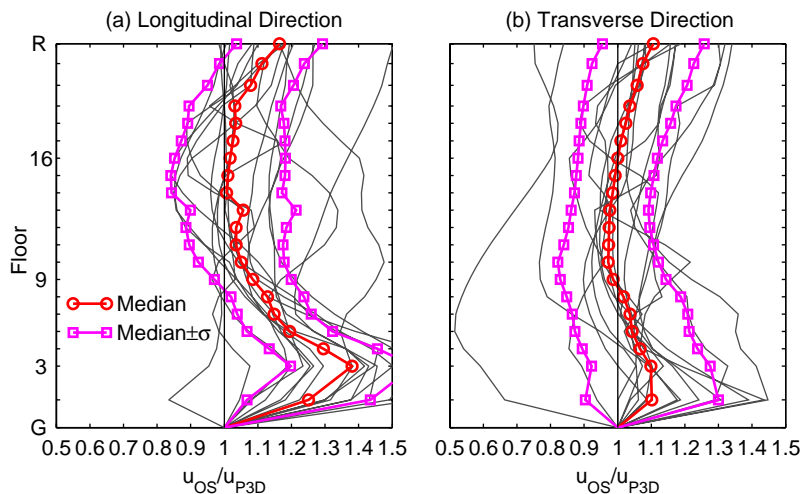


Figure 9. Height wise variation of ratio of peak floor displacements from *OpenSees* and *Perform3D* for North Hollywood Hotel.

The median of acceleration ratios in Figure 10 show that the *OpenSees* generally provides comparable estimates of floor accelerations throughout the building height as those from

Perform3D: the median of the floor accelerations ratio is very close to one. The exception may occur at a few floors where the ratio may differ from one by 0.05 to 0.15, e.g., 2nd floor and roof in the longitudinal direction (Figure 10a). The width of the median+ σ or median- σ band for floor accelerations varies from 0.05 (Figure 10b) to 0.1 (Figure 10a) implying that there is 5% to 10% dispersion in the response prediction from the two programs.

The median of ratio in Figure 11 shows that the *OpenSees* generally provides comparable estimates of base shear to that from *Perform3D*: the median of the base shear ratio is very close to one. The width of the median+ σ or median- σ band is about 0.1 implying that there is 10% dispersion in the response prediction from the two programs.

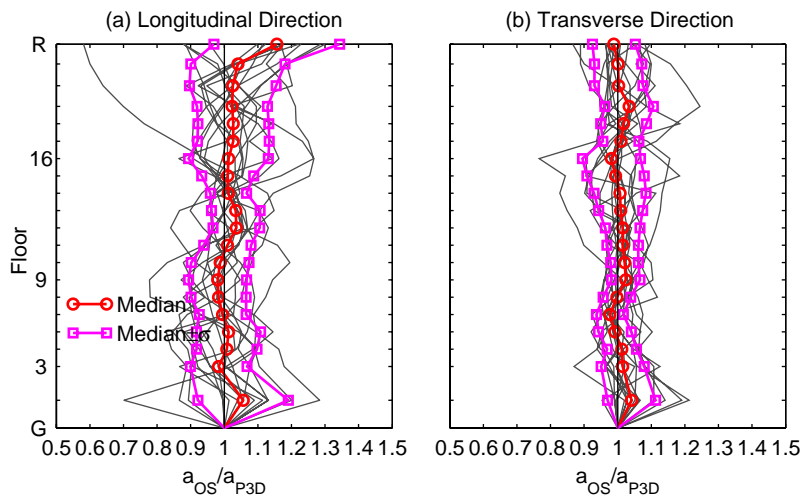


Figure 10. Height wise variation of ratio of peak floor accelerations from *OpenSees* and *Perform3D* for North Hollywood Hotel.

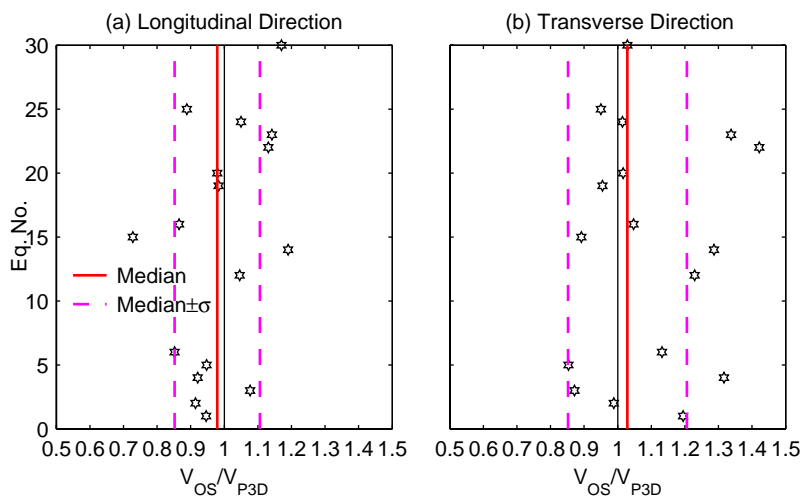


Figure 11. Ratio of base shear from *OpenSees* and *Perform3D* for North Hollywood Hotel.

19-Story Office Building in Los Angeles

The median of displacement ratios in Figure 12 for the Los Angeles Building indicates that *OpenSees* tends to provide larger estimate of displacements throughout the building height

in the longitudinal direction (Figure 12a) and in upper floors in the transverse direction (Figure 12b) compared to the *Perform3D*. The difference in median value of the displacement ratio in upper and lower floors varies from 1.05 to 1.1 indicating that the response from the two programs can differ by 5% to 10%. The width of the median+ σ or median- σ band is about 0.1 implying that there is 10% dispersion in the response prediction from the two programs.

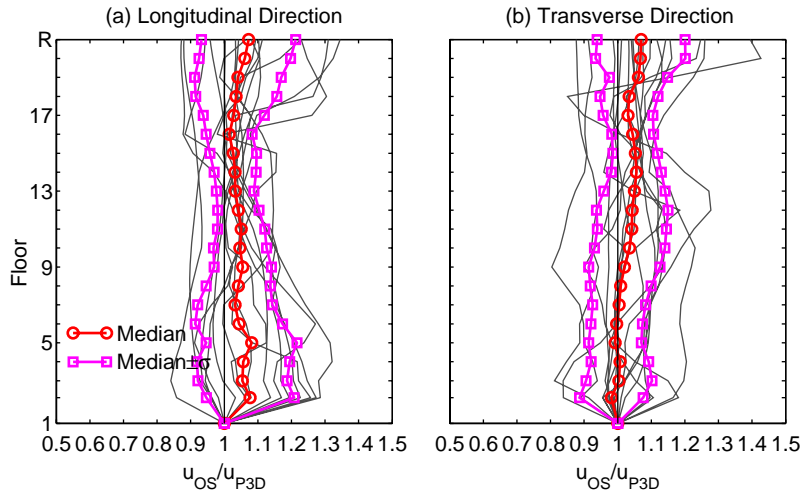


Figure 12. Height wise variation of ratio of peak floor displacements from *OpenSees* and *Perform3D* for Los Angeles Building.

The median of acceleration ratios in Figure 13 show that the *OpenSees* generally provides comparable estimates of upper floor accelerations as those from *Perform3D*: the median of the floor accelerations ratio is very close to one. For lower floors, where a soft story condition occurs in the Los Angeles building due to taller story height, the ratio may differ from one by 0.1 to 0.25, e.g., 2nd floor (Figures 13a and 13b). The width of the median+ σ or median- σ band for floor accelerations varies from 0.05 (Figure 13a) to 0.1 (Figure 13b) implying that there is 5% to 10% dispersion in the response prediction from the two programs.

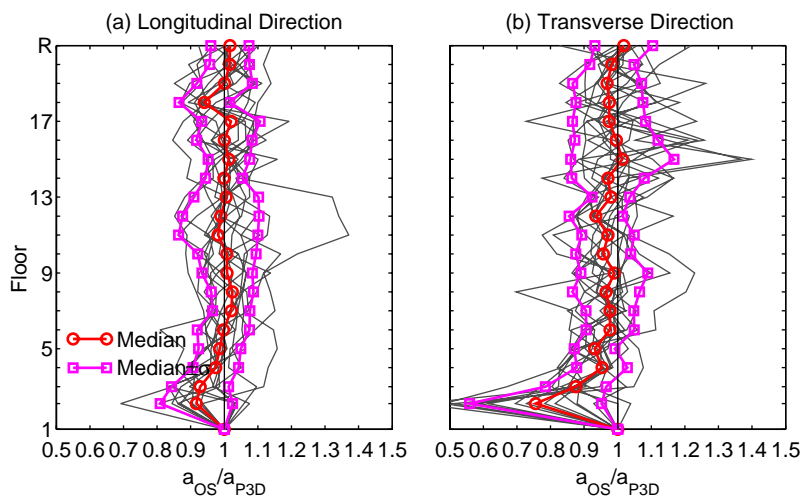


Figure 13. Height wise variation of ratio of peak floor accelerations from *OpenSees* and *Perform3D* for Los Angeles Building.

The median of ratio in Figure 14 show that the *OpenSees* provides lower base shear in the longitudinal direction and comparable base shear in transverse direction than that from *Perform3D*. The width of the median+ σ or median- σ band varies from 0.05 to 0.1 implying that there is 5% to 10% dispersion in the response prediction from the two programs.

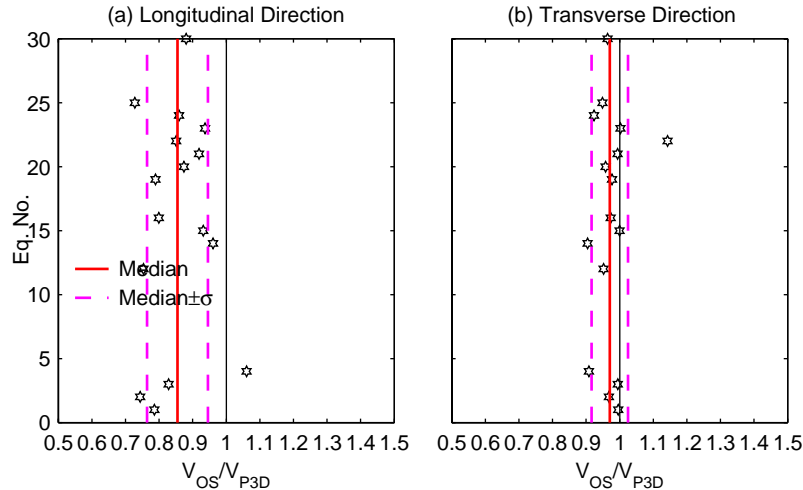


Figure 14. Ratio of peak base shear from *OpenSees* and *Perform3D* for Los Angeles Building.

Effects of Software on Peak Response from RHA

The results presented so far indicate that there can be 10% to 40% difference in prediction of median peak response from different software. The difference is much higher for reinforced concrete building compared to the steel building, and in median prediction of floor displacements compared to prediction of floor accelerations and base shear. It is useful to recall that *OpenSees* used a fiber section model which captured spread of inelastic action over the member section whereas *Perform3D* used a FEMA-356 type concentrated plastic hinge with strength loss. Therefore, larger variability in the response prediction for the reinforced concrete building appears to be due to significant behavior differences in reinforced-concrete beam/columns models available in the two selected computer programs. On the other hand, smaller variability in the response of the steel building appear to be due to less significant differences in the steel beam-column models available in the two programs. Furthermore, there is 10% to 15% dispersion as apparent from median $\pm\sigma$ band. It is useful to emphasize that above observations are for median response ratios only. Response ratio for individual ground motions from the two programs may vary by as much as 50%.

Comparison of Inertial and True Base Shears

As mentioned previously, base shear in buildings with recorded motions is typically estimated from summation of floor inertial forces above the building’s base (Figure 15a). For this purpose, the floor inertial forces are computed by multiplying the floor masses with the total floor accelerations. The base shear thus calculated is designated as the “inertial base shear” in this investigation. This base shear is generally accepted to provide a good estimate of the “true base shear” which is equal to sum of shears in all columns at the building’s base (Figure 15b).

This section re-examines if the inertial base shear, V_{bl} , provides a good estimate of the true base shear, V_{bR} . For this purpose, ratios of the inertial and true base shears for the two buildings were computed from *OpenSees* and *Perform3D*. The accelerations used in computing the inertial base shear were those computed from RHA. The results are presented in Figures 16 to 19 for earthquakes for which the building was deemed not to collapse. The presented results include ratio for individual earthquakes along with the median values and median $\pm\sigma$ values.

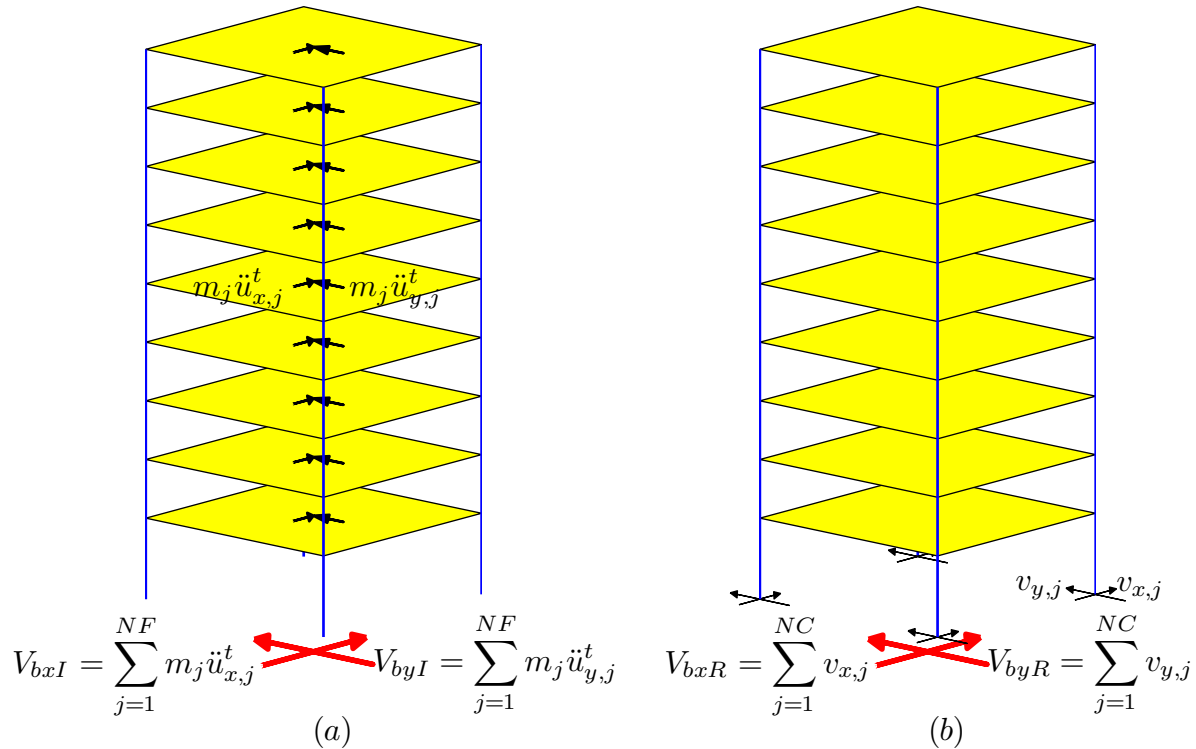


Figure 15. Computation of base shear: (a) Base shear computed from summation of inertial floor forces; and (b) Base shear computed from summation of column base shears.

20-Story Hotel in North Hollywood

The results presented in Figure 16 for the North Hollywood Hotel show that the ratio V_{bl}/V_{bR} from *OpenSees* for some earthquakes can be as high as 1.25. This indicates that inertial base shear may over predict the true base shear by up to 25%. The median value of the ratio is, however, much smaller: the median ratio is from 1.08 (Figure 16a) to 1.12 (Figure 16b). Therefore, it may be expected that the inertial force will over predict the true base shear in the median by about 10%. The width of the median $+\sigma$ or median $-\sigma$ band varies from 0.05 to 0.08 implying that there is 5% to 8% dispersion in the response prediction. The results presented in Figure 17 for *Perform3D* results show trends similar to those for *OpenSees* results in Figure 16 with the variations being slightly smaller for the former program.

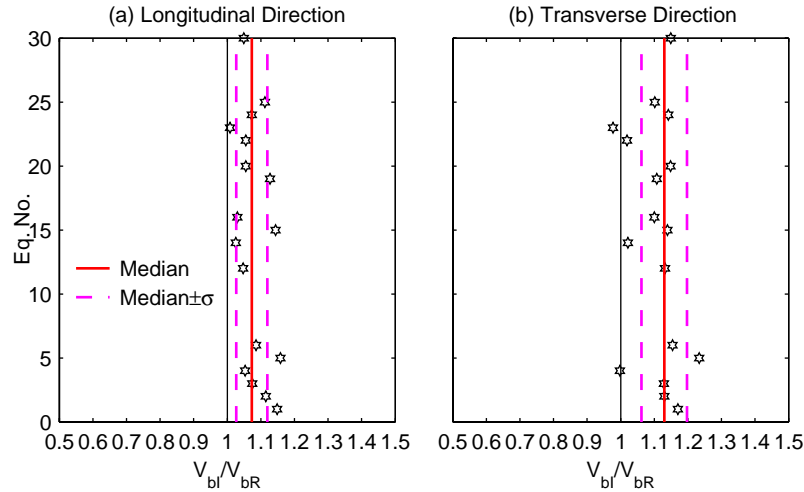


Figure 16. Ratio of peak inertial and true base shears from *OpenSees* for North Hollywood Hotel.

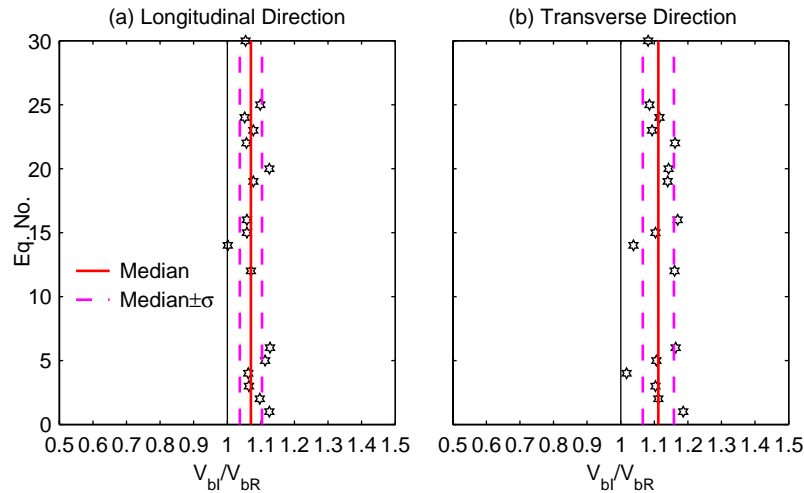


Figure 17. Ratio of peak inertial and true base shears from *Perform3D* for North Hollywood Hotel.

19-Story Office Building in Los Angeles

The results presented in Figure 18 for the Los Angeles building show very little variation in V_{bl}/V_{bR} from *OpenSees*: the median is very close to one (Figures 18a and 18b). The width of the median+ σ or median- σ band is about 0.2 in the longitudinal direction (Figure 18a) and very small in the transverse direction (Figure 18b). The results from *Perform3D* show median value of the ratio to range from 1.05 (Figure 19a) to 1.2 (Figure 19b) with the width of the median+ σ or median- σ band to range from 0.1 (Figure 19b) to 0.2 (Figure 19a). For individual earthquake, however, the inertial base shear may exceed the true base shear by as much as 75% (see Figures 18a and 19a).

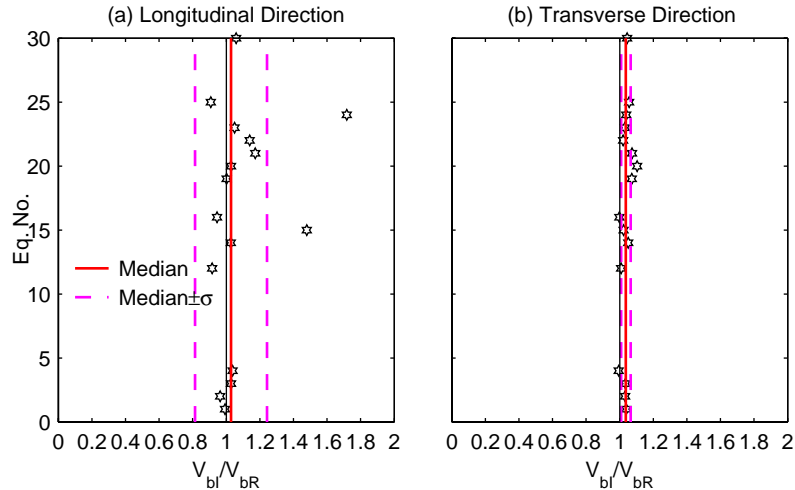


Figure 18. Ratio of peak inertial and true base shears from *OpenSees* for Los Angeles Building.

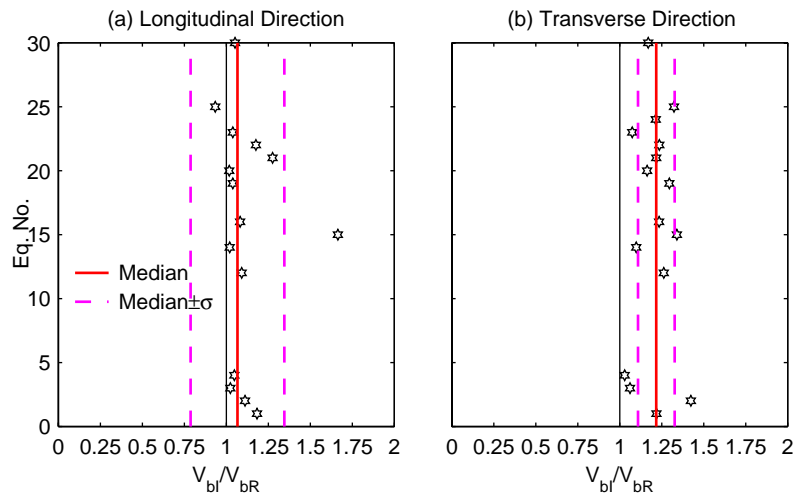


Figure 19. Ratio of peak inertial and true base shears from *Perform3D* for Los Angeles Building.

The presented so far indicate that the median inertial base shear exceeds the true base shear by 10 to 20%. For individual earthquakes, however, the inertial base shear may overestimate the true base shear by as much as 75%. Therefore, inertial base shear should be used with caution as an estimate of the true base shear.

Effects of Time Shift on Inertial Base Shear

The inertial base shear is typically used to estimate the true base shear in buildings with acceleration recorded during earthquakes. A mid- or high-rise building is instrumented with a large number of accelerometers and all of these accelerometers may not be connected to a single recorder. Although, the recorders are generally time synchronized, there is still a possibility of time shift between different recorders. Examined next is the effect of time shift on inertial base shear. For this purpose, time shift equal to one time step is introduced between the base acceleration and the relative acceleration computed from RHA of the two selected buildings using *OpenSees* and the inertial base shears are recomputed; recall the inertial base shear requires total floor accelerations which are defined as sum of the base acceleration and relative floor

acceleration. The results are presented in Figure 20 for the North Hollywood Hotel and Figure 21 for the Los Angeles Building. These results indicate a large discrepancy between the inertial and true base shears. The median of inertial base shear may exceed the true base shear by a factor of 2 to 4. Furthermore, the inertial base shear may be as large as 10 times the true base shear for individual earthquakes. Clearly, time shift, even a small one, can lead to erroneous estimate of base shear demand in buildings with accelerations recorded during earthquakes.

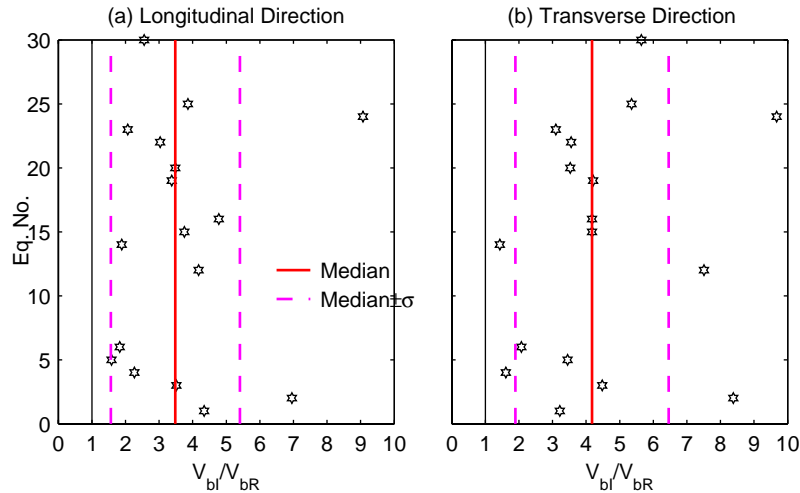


Figure 20. Ratio of peak inertial and true base shears from *OpenSees* for North Hollywood Hotel; results are computed by introducing a one time step delay between base acceleration and relative floor acceleration.

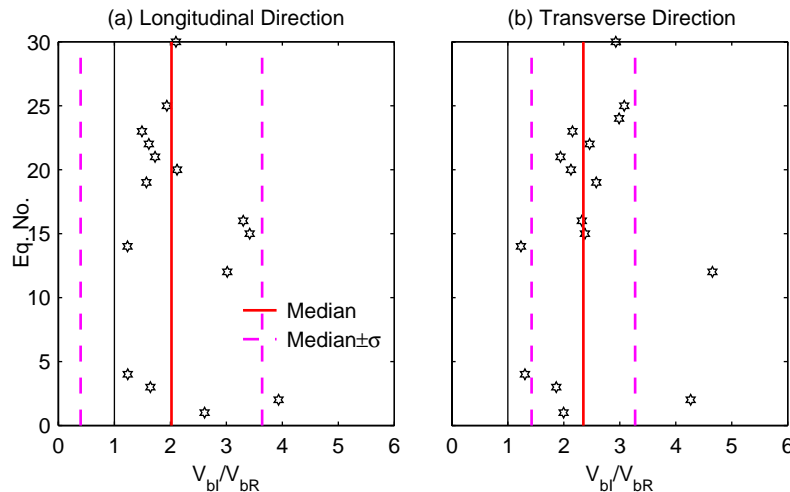


Figure 21. Ratio of peak inertial and true base shears from *OpenSees* for Los Angeles Office Building; results are computed by introducing a one time step delay between base acceleration and relative floor acceleration.

Conclusions

The investigation first examined the effects of modeling assumptions and two different computer programs on nonlinear response of three-dimensional buildings. It was found that modeling assumptions may significantly affect the pushover curves: concentrated plasticity

model leads to lower strength, early initiation of yielding, and post yielding strength loss in pushover curves compared to spread plasticity model; and strength loss model for beams/columns leads to significant post yielding strength loss in the pushover curve. The concrete material model, on the other hand, appears to have minimal effect on the pushover curves of reinforced concrete buildings. While most of the differences may be attributed to differences in modeling options available in different programs (e.g., *OpenSees* does not have an option for modeling FEMA-356 force-deformation behavior with strength loss whereas *Perform3D* does), some differences may also occur due to differences in solution schemes and convergence criteria available in different software programs.

It was also found that the prediction of median peak response from different software can differ from 10% to 40%. The difference tends to be much higher for reinforced concrete building compared to the steel building, and for floor displacements compared to floor accelerations and base shear. Furthermore, there is dispersion of about 10% to 15% in the median prediction as apparent from median $\pm\sigma$ band. For individual ground motions, the peak responses from different computer programs may vary by as much as 50%.

This investigation also examined if the “inertial base shear”, defined as summation of floor inertial forces above the building’s base with the floor inertial forces computed by multiplying the floor masses with the total floor accelerations, can provide an accurate estimate of the “true base shear” which is equal to sum of shears in all columns at the building’s base. This investigation indicated that the median inertial base shear exceeds the true base shear by 10 to 20%. For individual earthquakes, however, the inertial base shear may overestimate the true base shear by as much as 50%. It was also found that even a small recording time delay between different acceleration channels may lead to large errors if these accelerations are used to estimate base shear demand during an earthquake event. Therefore, inertial base shear should be used with caution as an estimate of the true base shear.

Acknowledgment

This investigation is supported by the California Department of Conservation, California Geological Survey, Strong Motion Instrumentation Program, Contract No. 1007-907. This support is gratefully acknowledged. The author would also like to acknowledge the support provided by Prof. Graham Powell on implementation of *Perform3D* and by Dr. Charles Chadwell on use of *Xtract*.

References

- ASCE (2000). Prestandard and Commentary for the Seismic Rehabilitation of Buildings. *Report No. FEMA-356*, Building Seismic Safety Council, Federal Emergency Management Agency, Washington, D.C.
- Bernal, D. (2007). Predictive Capability of Nonlinear Static Analysis Procedures for Seismic Evaluation of Buildings, *CSMIP Data Interpretation Report*, Strong Motion Instrumentation Program, CDMG, Sacramento, CA.
- Chadwell, C. (2007). Capacity Analysis and Pushover Program (Capp): Version 1.04. Imbsen & Associates, Inc., <www.imbsen.com>.

- CSI (2006). Perform3D: Nonlinear Analysis and Performance Assessment for 3d Structures: Version 4. Computers and Structures, Inc., Berkeley. <www.csiberkeley.com>.
- De la Llera, J. C. and Chopra, A. K. (1998). "Evaluation of Seismic Code Provisions Using Strong-Motion Building Records from the 1994 Northridge Earthquake," Report No. UCB/EERC-97/16, Earthquake Engineering Research Center, University of California, Berkeley, CA.
- Goel, R.K. (2005). "Evaluation of Modal and FEMA Pushover Procedures Using Strong-Motion Records of Buildings," *Earthquake Spectra*, 21(3): 653-684, 2005.
- Goel, R.K. (2007). "Evaluation of Current Nonlinear Static Procedures Using Strong Motion Records," *Proceedings of the 2007 Structures Congress, Long Beach, CA*, American Society of Civil Engineers, Reston, VA.
- Goel, R.K. (2008). "Mode-Based Procedure to Interpolate Strong Motion Records of Instrumented Building." *ISET Journal of Earthquake Technology*, 45(3-4), December.
- Goel, R.K. and Chadwell, C. (2007). Evaluation of Current Nonlinear Static Procedures for Concrete Buildings Using Recorded Strong-Motion Data, *CSMIP Data Interpretation Report*, Strong Motion Instrumentation Program, CDMG, Sacramento, CA.
- Karsan, I. D., and Jirsa, J. O. (1969). "Behavior of concrete under compressive loading." *Journal of Structural Division ASCE*, 95(ST12).
- Limongelli, M. P. (2003). "Optimal Location of Sensors for Reconstruction of Seismic Response through Spline Function Interpolation," *Earthquake Engineering and Structural Dynamics*, 32(7):1055-1074.
- Mander, J. B., Priestley, M. J. N., and Park, R. (1988). "Theoretical stress-strain model for confined concrete." *Journal of Structural Engineering ASCE*, 114(8), 1804-1825.
- McKenna, F. and Fenves, G. (2001). The Opensees Command Language Manual: 1.2. Pacific Earthquake Engineering Center, University of California, Berkeley, (<http://opensees.berkeley.edu>).
- Naeim, F., Lee, H., Bhatia, H., Hagie, S., and Skliros, K. (2004). "CSMIP Instrumented Building Response Analysis and 3-D Visualization System (CSMIP-3DV)," Proceedings, SMIP04 Seminar on Utilization of Strong-Motion Data, Strong Motion Instrumentation Program, CDMG, Sacramento, CA.
- Naeim, F. (1997). Performance of Extensively Instrumented Buildings During the January 17, 1994 Northridge Earthquake: An Interactive Information System, Report No. 97-7530.68, John A. Martin & Associates, Los Angeles, CA, 1997.
- Popovics, S. (1973). "A numerical approach to the complete stress strain curve for concrete." *Cement and concrete research*, 3(5), 583-599.
- TRC (2008), Cross Sectional Analysis of Structural Components, v3.0.8, TRC/Imbsen Software Systems, Rancho Cordova, CA. <<http://www.imbsen.com/>>

OBSERVATIONS OF STRUCTURAL PERFORMANCE NEAR STRONG-MOTION STATIONS DURING THE ITALY L'AQUILA EARTHQUAKE

Chris D. Poland
Degenkolb Engineers, San Francisco

Abstract

The deployment and retrieval of strong motion records over the past 80 years has provided new insight into the intensity, distribution, and character of strong motion. Gathering, processing, and interpreting the records has also become a key aspect of understanding building response and damage patterns. Specific inspections of the buildings around the 2009 L'Aquila Italy Earthquake strong motion recording stations offers yet another glimpse of how well buildings seem to be responding to strong shaking that appears to exceed the design levels. The observed damage pattern beyond the instrumented locations also offers some indication of the variation of shaking and once again demonstrates the need for significantly more instruments.

Background and Observations

L'Aquila is located in central Italy, about 60 miles northeast of Rome in the mountainous Abruzzo region. Construction in the region dates back hundreds of years and includes a rich collection of stone, masonry and concrete buildings. Italy's design standards for the expected earthquakes have been developing since the early 1900's and are similar to those used in California. The magnitude 5.8 earthquake that occurred on April 6, 2009, damaged thousands of buildings, collapsed several dozens, killed just over 300 people and left nearly 70,000 homeless. Italy's 2006 Seismic Hazard map indicates that the region is in the second highest seismic region with an expected PGA of .25g to .275g for the 10/50 earthquakes.

Italy's Rete Accelerometrica Nazionale (RAN) has deployed hundreds of strong motion instruments throughout Italy. Dozens recorded the April 6, 2009, event with four stations located within 6 km of the epicenter. Three of those stations were a part of a five-station array deployed to capture the variation of motion across a valley. The fourth was located near the ancient city and located at the base of the bluff on the north side. The records are posted on the Center for Engineering Strong Motion Data (www.strongmotioncenter.org) as well as from the RAN web site. Extensive documentation for each station site is also available from RAN.

The four strong motion stations near the epicenter recorded peak ground accelerations that varied from .36g to .67g with the strong shaking lasting about 10 seconds. The instrument located at the northeast end of the array reportedly went off scale at 1g, though the record has not been published due to quality concerns. It appears that the earthquake produced ground motions considerably larger than expected for the regions 10/50 earthquake. The response spectra for the recordings show the expected variation due to the local site conditions.

Figure 1 includes a single, sample response spectrum for the record taken nearest the ancient city and a cluster of buildings located nearby. None were seriously damaged. Figure 2 includes three of the five instruments in the valley array along with buildings located in the

immediate vicinity. In all cases, damage to the adjacent buildings was light to not visible, even for those in the area of the instrument that went off-scale. The buildings observed included many of the styles of construction in the region and ranged in height from one to six stories. The strength of these records and the lack of damage suggest that acceleration alone is not a good indicator of damage potential.

In an effort to catalogue the variations in the intensity of shaking throughout the region, the extent of damage to reinforced concrete frame/infill buildings was catalogued throughout the region. Four damage states from “Extreme” to “Mild” were defined and assigned based on visual inspection from the street. The GPS coordinates of each building were determined and plotted with an indicator of damage level on a Google Map image of the region as shown in Figure 3. The location of the strong motion instruments is also shown on the figure along with the zones of intensity inferred from the individual building observations. These zones represent the general damage patterns observed within each zone and not the worst-case occurrences.

Initial reports for the region suggested that the city was destroyed and blamed inadequate design standards and poor construction for the outcome. The reality is that the shaking appears to have far exceeded what was expected and the buildings, in general, performed amazingly well. The strong motion records provide the opportunity to better understand the damage and lack of damage that occurred. They also provide the opportunity for earthquake professionals to improve the design, evaluation and analysis techniques used to predict building performance and better account for the effects of variations in the geology and site conditions.

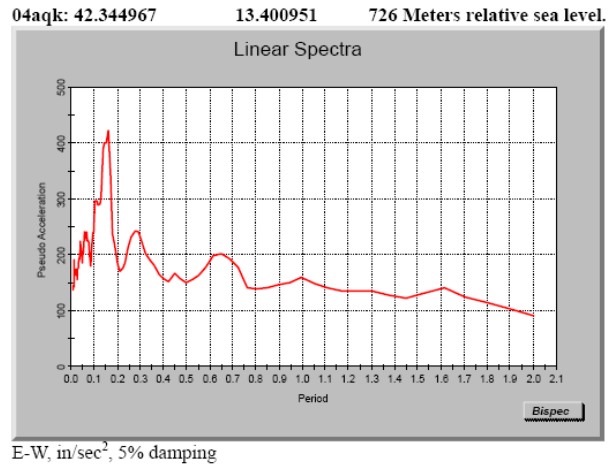
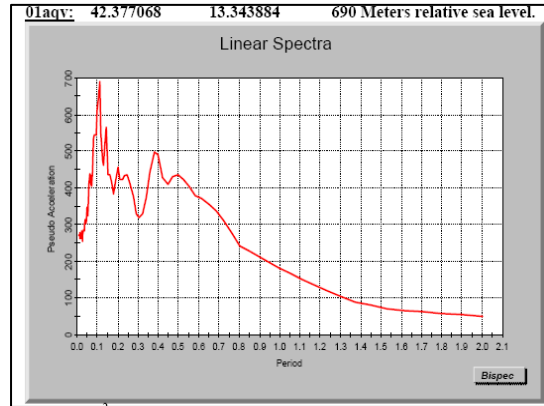
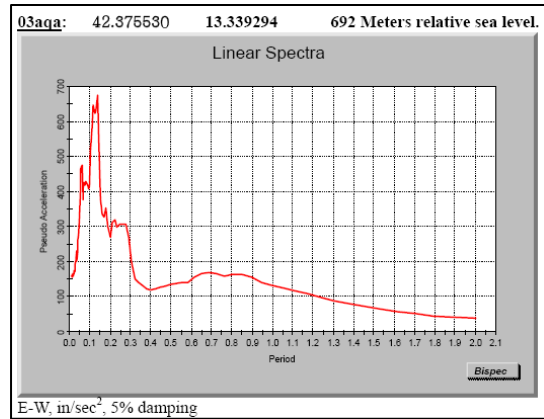


Figure 1. Strong Motion record near the Ancient City, .36g PGA

Station AQV, Valley location, .67g PGA



Station AQA, Edge of Valley location, .44g PGA



Station AQG, Rock location beyond valley edge, .51g PGA

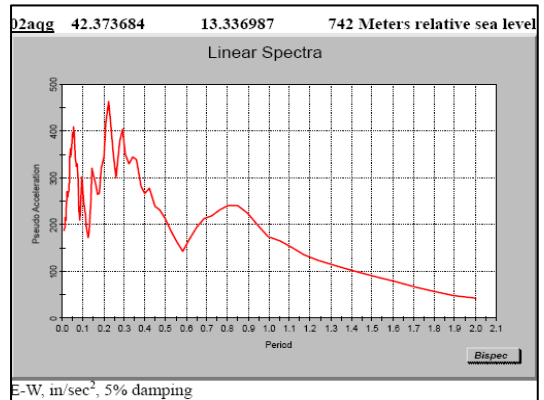


Figure 2. Response Spectra and nearby Sample Building Performance

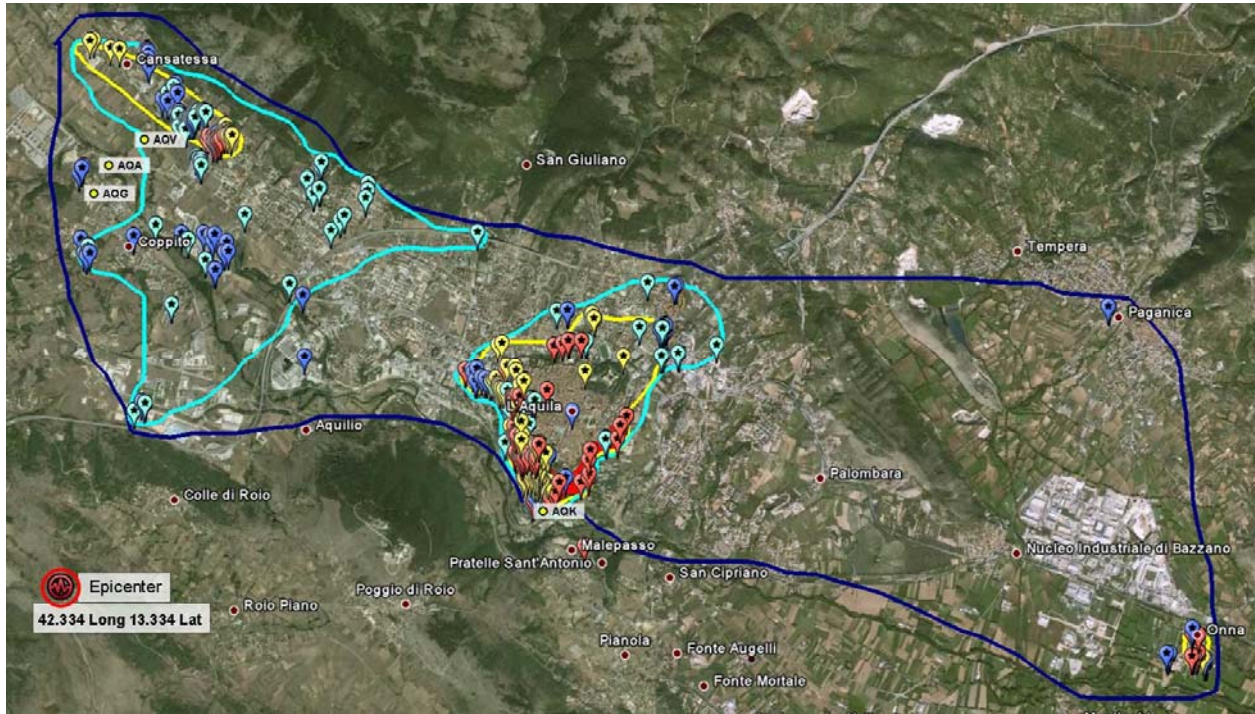


Figure 3. Inferred Intensity from Damage Observations

UTILIZATION OF STRONG-MOTION DATA FOR ASSESSMENT OF STRUCTURAL INTEGRITY IN INSTRUMENTED HIGHWAY BRIDGES

Virginia Mosquera, Andrew W. Smyth and Raimondo Betti

Department of Civil Engineering and Engineering Mechanics
Columbia University, New York

Abstract

This study focuses on the use of strong motion data recorded during earthquakes and aftershocks to provide a preliminary assessment of the structural integrity and possible damage in bridges. A system identification technique is used to determine dynamical characteristics and high-fidelity first-order linear models of four bridges from low level earthquake excitations. A finite element model (FEM) was developed and updated to simulate data from a damaging earthquake for one of the bridges. The difference between data recorded or simulated by FEM and data predicted by the linear model was used to detect damage. The use of this technique can provide an almost immediate, yet reliable, assessment of the structural health after a seismic event.

Introduction

It is of great interest after an extreme event such as an earthquake, to have reliable information regarding the integrity of a structure. In recent years, the use of vibration based damage detection techniques for structural health monitoring has gained significant attention by researchers. There is a considerable amount of studies on these techniques, where damage is usually determined by a change in the dynamical properties of the structure. Doebling et al. [1] presents a thorough review of these techniques.

An alternative for damage detection is to identify damage by determining the degree of nonlinearity present in the structural response [2]. If a linear model has been previously identified for a healthy state of the structure, this model should be able to accurately predict the response to any other input data if the structure stays in the elastic range. The difference between the recorded data and the response predicted by the linear model can be used to give an estimate of the state of the structure.

There has been a large amount of algorithms developed in the frequency and time domain to identify modal parameters and determine state space representations of linear dynamical systems. Many studies have successfully applied these techniques in the system identification of buildings and bridges [3],[4],[5]. Among those techniques, one that has shown great promise is the Eigensystem Realization Algorithm (ERA) proposed by Juang and Pappa [6], with Observer Kalman Filter Identification [7],[8].

In this study the ERA/OKID is used to identify the modal parameters and linear models of four bridges. The input and output data used for the identification are obtained from previous ground motions and structural responses recorded by the California Strong Motion

Instrumentation Program (CSMIP). One of the bridges was selected for further study and a FEM model was developed for it.

Due to assumptions made while developing a FEM and uncertainty in boundary conditions, geometrical and material properties of the structure, there can be significant differences between the dynamic behavior of the model and the real structure. To accurately represent the structure, the FEM model must be updated [9].

In model updating techniques an objective function is optimized to find a model that behaves similarly to the real structure [10], [11]. Here some structural parameters were varied to match the measured structural responses of the bridge, as well as the modal frequencies found using ERA/OKID. To select the optimum values for these parameters a Genetic Algorithm (GA) optimization approach [12] was used.

After the updating process, hinges which defined the nonlinear behavior of the structure were inserted in the model at the tower-deck and tower-foundation connections as well as in the bent cap on each side of the column. Once the FEM was completed, appropriately scaled input time histories of the ground motion from a previously recorded data set were used to simulate the possible nonlinear response of the bridge to a future damaging earthquake. The simulated time histories of the response from the nonlinear model will represent a new set of data that can be compared with the data predicted by the linear model identified with ERA/OKID and provide an estimate of the location and amount of structural damage that occurs during a major earthquake.

System Identification

State space representation

The dynamic behavior of a multi (n) degree-of-freedom (n DOF) linear structural system can be represented by a system of second order differential equations as:

$$M\ddot{q}(t) + C\dot{q}(t) + Kq(t) = B_2u(t) \quad (1)$$

where $q(t)$ is the structural displacement vector, M , C and K are respectively the $n \times n$ mass, damping and stiffness matrices; $u(t)$ is the input vector and B_2 is the input matrix. When the input is a seismic excitation, the external forcing term $B_2u(t)$ can be replaced by $-M\ddot{q}_g(t)$, where $\ddot{q}_g(t)$ is the ground acceleration.

By defining $2n \times 1$ state vector $x(t)$ as a vector containing the displacement $q(t)$ and the velocity $\dot{q}(t)$, the system of second order differential equations (1) can be rewritten as a first order system of differential equations

$$\dot{x}(t) = A_c x(t) + B_c u(t) \quad (2)$$

$$y(t) = C_c x(t) + D_c u(t) \quad (3)$$

where the matrices A_c , B_c , C_c and D_c are the time invariant continuous time system matrices while $u(t)$, of dimension $r \times 1$, and $y(t)$, of dimension $m \times 1$, are the input and output vectors, respectively. Since the input and output generated by an earthquake excitation will be recorded at discrete time intervals, equations (2) and (3) must also be expressed in discrete time

$$x(k + 1) = Ax(k) + Bu(k) \quad (4)$$

$$y(k) = Cx(k) + Du(k) \quad (5)$$

where $x(k)$, $y(k)$, and $u(k)$ represent the state, output and input vectors, respectively, at time $t = k \Delta t$, with Δt being the sampling time. The matrices A , B , C and D are the discrete time versions of the continuous time matrices A_c , B_c , C_c and D_c .

Eigensystem Realization Theory

A realization is a set of matrices A , B , C and D that describe the behavior of the structure and satisfy equations (4) and (5). A system can have an infinite number of realizations that will predict the same output for a given input: a minimum realization will have the smallest state-space dimensions among all the possible realizations and the modal parameters found will be the ones of the structure.

The ERA algorithm is used to find the minimum realization. This algorithm uses the Hankel matrix, which can be written as:

$$H(k-1) = \begin{bmatrix} Y_k & Y_{k+1} & Y_{k+2} & \dots & Y_{k+\beta+1} \\ Y_{k+1} & Y_{k+2} & Y_{k+3} & \dots & Y_{k+\beta} \\ Y_{k+2} & Y_{k+3} & Y_{k+4} & \dots & Y_{k+\beta-1} \\ \vdots & \vdots & \vdots & \ddots & \vdots \\ Y_{k+\alpha-1} & Y_{k+\alpha} & Y_{k+\alpha} & \dots & Y_{k+\alpha+\beta-1} \end{bmatrix} \quad (6)$$

where Y_k are the Markov parameters, defined as:

$$Y_0 = D \quad (7)$$

$$Y_k = CA^{k-1}B \quad \text{for } k=1,2,\dots \quad (8)$$

while α and β are sufficiently large numbers that determine the size of the Hankel matrix.

For lightly damped systems, the number of Markov parameters can be quite large so to make the computational effort quite cumbersome. To circumvent this problem, the Observer Kalman Filter Identification algorithm transforms the state equations (4) and (5) into observer equations where the observer gain matrix is chosen to make the observer asymptotically stable. In this case, it is much easier to retrieve the observer's Markov parameters and, through a recursive relation, to obtain the system's Markov parameters. Details of this methodology can be found in [4], [7] and [8].

Useful information about the system's dynamics can be obtained by the Singular Value Decomposition (SVD) of $H(0)$, that can be expressed as:

$$H(0) = U\Sigma V^T = \begin{bmatrix} U_n & U_{n_1-n} \end{bmatrix} \begin{bmatrix} S_n & 0 \\ 0 & 0 \end{bmatrix} \begin{bmatrix} V_n \\ V_{n_2-n} \end{bmatrix} = U_n S_n V_n \quad (9)$$

where the matrices U , of dimensions $n_1 \times n_1$, and V , of dimension $n_2 \times n_2$, are orthonormal while Σ is a rectangular matrix, of dimension $n_1 \times n_2$, that contains the singular values of $H(0)$.

By looking at the non-zero singular values contained in the matrix S_n , it is possible to identify the number of vibrational modes that significantly contribute to the dynamic response. If the signals contain very small noise level, the distinction between non zero singular values (corresponding to structural modes) and “almost zero” singular values (noise related modes) is quite evident, allowing a clear estimation of the order of the system. However, if the recorded data have a substantial amount of measurement noise, then the distinction between structural and noise modes is not clear and this requires additional manipulation (e.g. stabilization diagram and/or optimization).

Using the definition of the Markov parameters, the Hankel matrix $H(1)$ and the singular value decomposition of $H(0)$, the state matrix A , the input matrix B and the output matrix C in equations (4) and (5) can be expressed as:

$$A = S_n^{-\frac{1}{2}} U_n^T H(1) V_n S_n^{-\frac{1}{2}} \quad (10)$$

$$B = S_n^{-\frac{1}{2}} V_n E_r \quad (11)$$

$$C = E_m^T U_n S_n^{\frac{1}{2}} \quad (12)$$

where $E_m^T = [I_m \ 0_m \ \dots \ 0_m]$, $E_r = [I_r \ 0_r \ \dots \ 0_r]$, with I_i and 0_i being an identity matrix and a null matrix, respectively, of order i .

Model Updating

Another approach to create a dynamic model of a structural system is to directly determine the mass, damping and stiffness matrices, as they appear in equation (1). This can be accomplished by using the FEM. However, no matter how accurate the initial FEM model, there are always inaccuracies between the dynamic behavior of such a model and the real structure, inaccuracies that can be reduced through model updating. The purpose of model updating is to adjust the parameters of the FEM (e.g. Young's modulus, ultimate strength, boundary conditions, etc.) in a way such that it behaves as close to the real structure as possible. Usually, updating techniques vary the structural parameters of the model so as to minimize an objective function that compares measured and numerical responses (e.g. measured and computed natural frequencies, recorded and predicted time histories of the structural response, etc.). Different techniques have been proposed for this purpose; in this project, a form of Genetic algorithms has been used.

Generic Algorithm

Genetic algorithms have been broadly used as a tool to find an exact or approximate solution for search or optimization problems. Essentially, it is a programming technique that mimics the biological process of natural evolution and survival of the fittest to solve an optimization problem [13].

The Genetic Algorithm was first introduced by John Holland [14], who proposed that each potential solution to a problem can be seen as a set of genes. Usually, a gene is represented by binary bits and the possible solution by a binary string is called chromosome. The evolution process starts from a randomly-generated population of chromosomes. At each cycle, a new set

of chromosomes is generated by recombination and mutation of a previous generation. The purpose of this evolutionary algorithm is to eventually find the fittest chromosome that will lead to the best solution for the problem at hand. All genetic algorithms follow these basic steps:

A set of parameters from the problem are selected to be encoded into a binary string. Once the parameters have been selected, an initial population of chromosomes is randomly generated. A fitness function is selected and evaluated for each member of the population to determine the quality of each solution.

The selection of a chromosome for reproduction is based on its fitness; there are different schemes to select the parent chromosomes, like the roulette-wheel selection and tournament selection among others. In the roulette wheel, the probability to be selected is proportional to the fitness of each chromosome while, in the tournament selection, subgroups of chromosomes are selected and members of each subgroup compete against each other. The latter selection contributes toward the preservation of diversity on the population and it is used here.

Once the parent chromosomes have been selected, the reproduction process is simulated by applying a crossover operator and a mutation operator. The crossover operator tries to simulate the recombination that occurs to chromosomes during reproduction. A position in the binary string is randomly selected and mutually exchanges parts of the string before and after this point to create two offsprings or child chromosomes. The mutation operator is applied in order to improve the fitness and avoid loss of diversity in the population. It involves a random alteration of the genes and it has a small probability of occurrence.

The evolutionary process is repeated until a termination criterion is satisfied. The following termination criteria are commonly used: 1) a maximum number of generations is completed [15],[16], 2) a global minimum within an specified tolerance was found [17], or 3) a maximum number of consecutive generations without improvement was reached [18]. In the problem studied here, the applied termination criterion was the maximum number of generations. The steps described above are illustrated in Fig. 1.

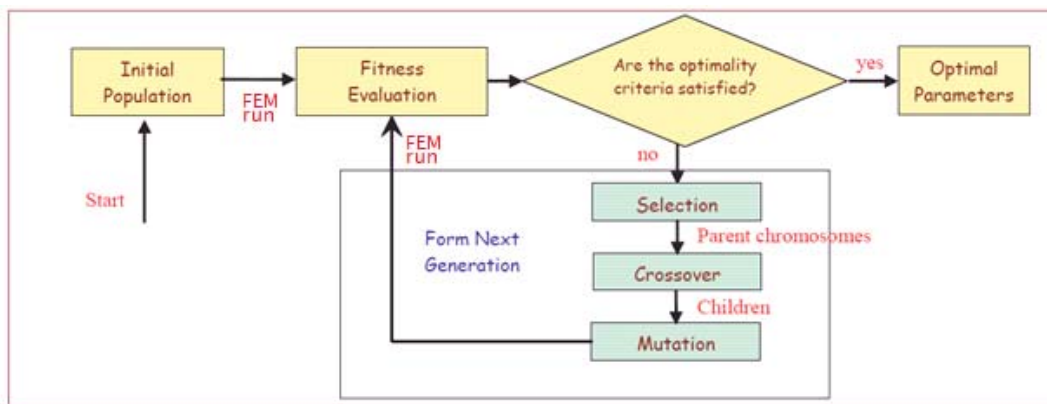


Fig. 1. Genetic Algorithm flowchart

These techniques can also be combined with others such as elitism, which guarantees survival of the fittest chromosome into the next generation; and niching, which allows the possibility of exploring different local optima by creating and evolving smaller subgroups within the population. Another recent technique is the micro-GA [19], [20], which prevents loss of

diversity by restarting the population as soon as it degenerates below some threshold. There is also the sawtooth-GA technique proposed by Koumoussis, and Katsaras [21], which proved to be most helpful for the particular problem considered here. This method uses a variable population size of mean value \bar{n} , and amplitude D , and a periodic partial re-initialization of the population of a period T , in the form of a saw-tooth function as shown in Fig. 2.

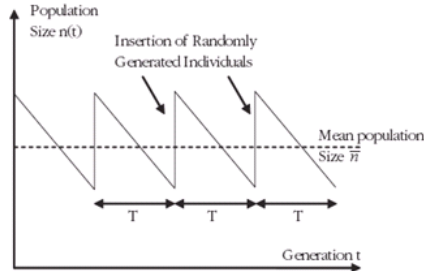


Fig. 2. Population variation scheme of saw-tooth GA.

Analysis of results

When a structure is subjected to a severe seismic event, it will deform into the inelastic range, exhibiting a nonlinear hysteretic behavior. Since the amount of damage experienced by the structure will increase as the inelastic behavior increases, damage can be determined by estimating the degree of nonlinearity present in the response of the bridge.

The linear state-space model identified by ERA/OKID is able to accurately predict the response of the structure at different sensor locations to any ground motion that produces a linear-elastic behavior on the bridge. However, if nonlinear behavior occurs, the model will no longer be able to predict the structural response. The difference between the predicted response and the measured response will be used to determine whether the structure has suffered damage or not. This difference will be quantified by the Root Mean Square (RMS) error

$$\text{RMSerror} = \sqrt{\frac{\sum_1^n (\text{Acc}_{\text{measured}} - \text{Acc}_{\text{predicted}})^2}{\sum_1^n (\text{Acc}_{\text{measured}})^2}} \quad (13)$$

where n is the number of time steps in each acceleration time history.

Experimental results

In this paper four bridges instrumented by CSMIP are studied. . The bridges studied here are a) Rio Dell – Hwy 101/Painter Street Overpass, b) Sylmar – I5/14 Interchange Bridge, c) San Bernardino – I10/215 Interchange and d) El Centro – Hwy 8/Meloland Road Overpass. Initially the modal parameters of each bridge were identified using ERA/OKID. After this identification, the Meloland Road Overpass was selected for further study.

System identification

The Rio Dell overpass is a two span bridge with a length of 265 feet. It is a monolithic, cast in place, prestressed concrete, box girder bridge with end diaphragm abutments and a two column bent. Both end diaphragm abutments and two-column bent are skewed at 39 degrees and supported on piles. It was instrumented in 1977 with 17 strong motion accelerometers along one side of the deck and at the base of one of the piers and 3 accelerometers at the free field. In the

identification process 7 accelerometers along the deck were used as output data and 6 accelerometers at the embankments as input data (Fig. 3a).

The Sylmar interchange bridge is a curved concrete box girder with a length of 1582 feet and a deck width of 51 feet. It has 9 spans supported in single column bents and one expansion joint. The columns are orthogonal, supported by circular CIDH concrete piles. It was constructed and instrumented in 1995. Thirty nine strong motion accelerometers were installed along the deck, abutments and base of the columns, and 3 more at the free field site. For the modal parameter identification 9 channels were used as inputs and 21 channels as outputs (Fig. 3b).

The San Bernardino connector is a curved multi-span concrete box girder with a length of 2540 ft. It has five separation joints that divide the bridge into six segments of different lengths. The superstructure is supported by single column concrete bents; the columns are octagonal in shape and have variable height. The Bridge was constructed in 1973 and it was retrofitted in 1991. In the retrofiting, steel jackets were added to the columns, the foundation were enlarged and cables tying adjacent slabs at the expansion joints were replaced. In 1992 the bridge was instrumented with 37 strong motion accelerometers located along the deck, at the base of the columns and at the free field. Here 12 sensors located at the abutments and base of the columns were used as input data and 22 sensors along the deck of the bridge were used as output data for the modal parameter identification (Fig. 3c).

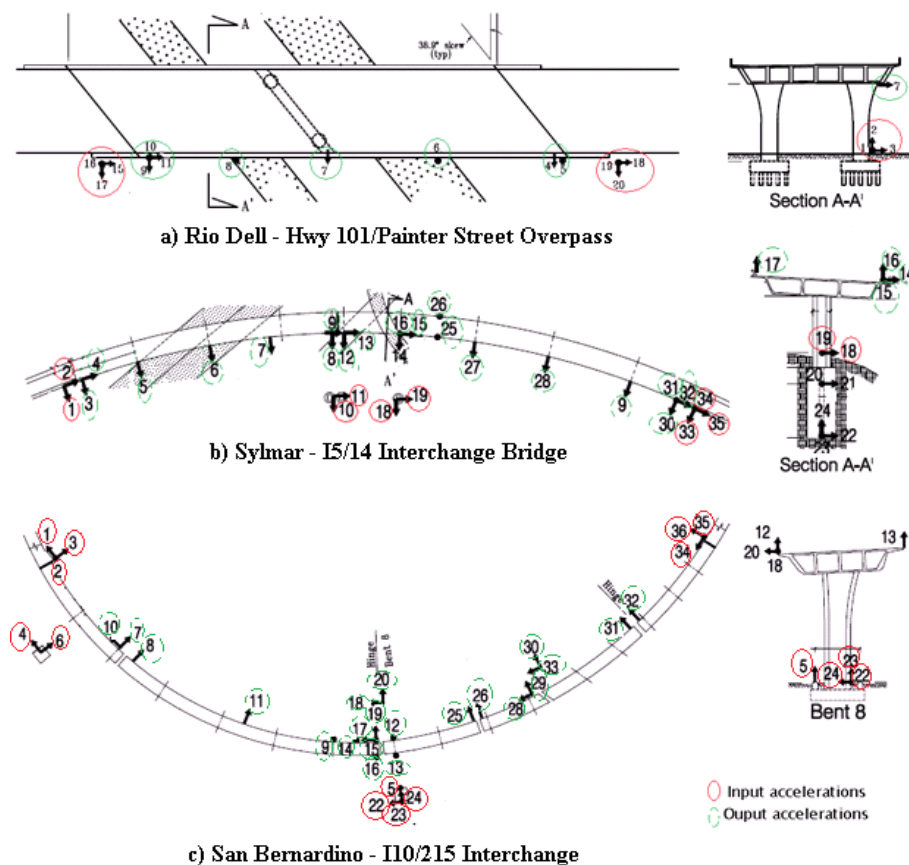


Fig. 3. Plan views and sensor locations of bridges

In the modal parameter identification of the first 3 bridges, two ground motions were used for each bridge and are listed in Table 1. The modal frequencies and damping identified for Rio Dell Overpass, Sylmar Interchange and San Bernardino Interchange are listed in Tables 2, 3 and 4 respectively. Similar frequencies were obtained for each bridge for both sets of ground motions: however, larger differences appear in the identified damping ratios. This is expected since the identification of the damping factors is much more difficult than the identification of the frequency and it is strongly dependent on the order of the identification model.

Table 1. Earthquakes used for system identification.

Bridge	Earthquake	Horizontal Apk(g)	
		Ground	Struct.
Rio Dell	Trinidad	0.147	0.330
	Rio Dell	N/A	0.593
Sylmar	April 11/1999	0.011	0.096
	Jan 14/2001	0.084	0.064
San Bernardino	Yucaipa	0.135	0.244
	Chino hills	0.110	0.165

Table 2. Dynamic parameters identified for Rio Dell Overpass

Mode	Trinidad EQ		Rio Dell EQ	
	ω (Hz)	ξ (%)	ω (Hz)	ξ (%)
1	3.39	2.67	3.36	2.20
2	4.33	9.53	4.14	20.29
3	4.85	2.82	4.91	6.42
4	-	-	5.09	4.21
5	6.08	1.94	-	-
6	7.30	3.17	7.19	10.12

Table 3. Dynamic parameters identified for Sylmar Interchange.

Mode	April 11 / 1999		Jan 14 / 2001	
	ω (Hz)	ξ (%)	ω (Hz)	ξ (%)
1	-	-	0.75	1.94
2	1.04	1.85	1.01	1.14
3	1.31	0.43	1.29	1.68
4	1.69	1.15	1.71	0.8
5	2.21	0.44	2.12	1.77
6	-	-	2.43	0.74
7	3.19	2.83	2.98	1.49
8	3.69	0.65	3.65	0.29
9	4.53	0.64	4.43	0.72
10	4.87	1.09	4.90	0.46
11	6.60	0.39	6.53	0.76
12	8.09	0.22	7.99	0.39
13	10.8	0.55	10.45	9.09

Table 4. Dynamic parameters identified for San Bernardino Interchange.

Mode	Yucaipa		Chino Hills	
	ω (Hz)	ξ (%)	ω (Hz)	ξ (%)
1	0.88	1.18	0.92	3.24
2	0.90	7.32	1.04	10.5
3	1.03	1.49	-	-
4	1.23	0.39	1.33	7.17
5	2.81	3.28	2.71	2.39
6	3.11	6.73	3.01	4.62
7	4.64	3.53	4.66	0.92
8	-	-	4.97	2.25
9	-	-	5.20	4.26
10	6.68	1.76	6.47	1.33
11	-	-	7.22	1.26
12	8.93	0.58	9.17	0.83

The Meloland Road Overpass (MRO) is a reinforced concrete box girder bridge. It consists of two 104 feet spans, constructed monolithically with the abutments and a central circular pier of 5 feet of diameter and 21 feet of height. The pier and the abutments are supported on timber piles. The MRO was constructed in 1971; in 1979 the bridge was instrumented with 26 strong motion accelerometers along the superstructure, base of the pier, embankments and free field. In 1991 the instrumentation was upgraded to 32 sensors (Fig. 4).

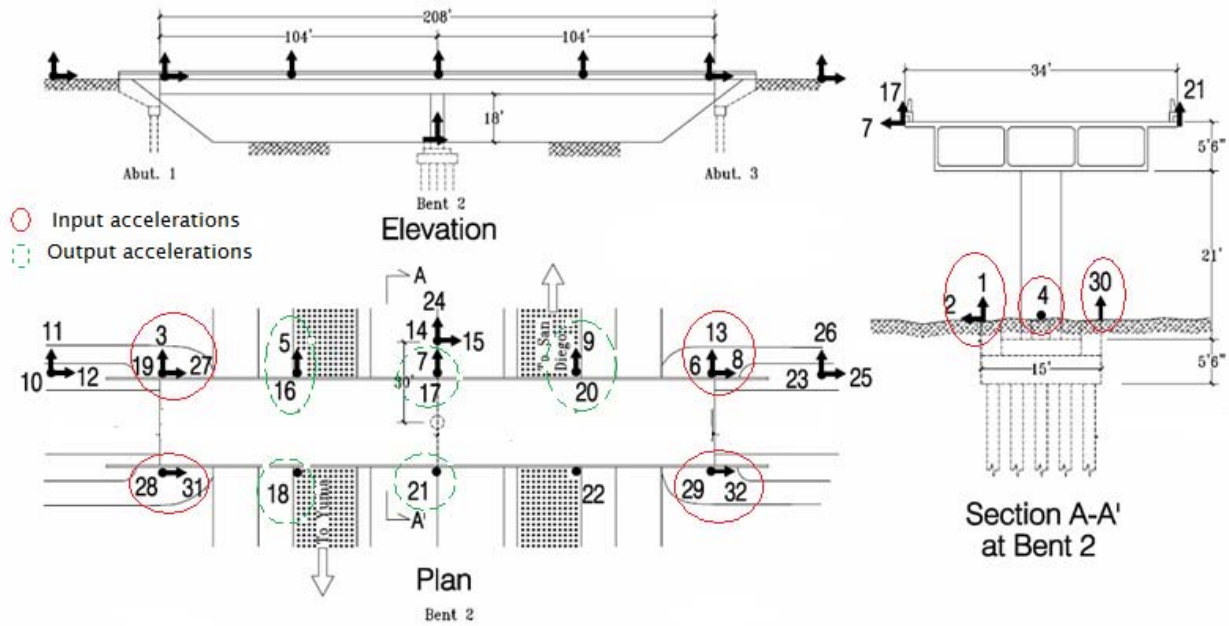


Fig. 4. Elevation and plan views of MRO along with sensor locations

For the system identification of this bridge using ERA/OKID, 14 input acceleration records and 8 output acceleration records were used. The sensors used for the inputs are located at the abutments and at the base of the pier in the three orthogonal directions, while the output sensors are located along the deck of the bridge in the transverse and vertical directions, as shown in Fig. 4. The identification was performed for five ground motions listed in Table 5; all of them were of small magnitude so that a linear behavior was expected.

Table5. Earthquakes used in system identification of MRO

Earthquake	Horizontal Apk (g)		Distance (Km)
	Ground	Structure	Epicenter
Cerro Prieto Feb 8 2008	0.020	0.058	41.9
Cerro Prieto Event 1 Feb 11 2008	0.012	0.035	45
Cerro Prieto Event 2 Feb 11 2008	0.014	0.042	37
Calexico Nov 20 2008	0.017	0.027	50.4
Calexico Dec 27 2008	0.006	0.02	24.5

The identified frequencies and damping ratios are presented in Table 6: for the first three ground motions, six frequencies were identified while, for the remaining two, it was possible to identify only five. The values of the identified frequencies and damping ratios are quite consistent among the five sets: of particular interest is the damping ratio relative to the second frequency that shows consistently high values ranging from 17.40% to 22.79%.

Looking at the time histories of the structural acceleration, extremely good agreement was found between the response predicted by the identified models and the actual recorded response, as can be inferred from the RMS errors for all the channels and ground motions (Table 7). Fig. 5 shows the actual and predicted responses of the bridge at channels 5 and 18 for Cerro Prieto Feb 8 2008.

Table 6. Dynamic parameters identified for MRO

Mode	Cerro Prieto Feb 8 2008		Cerro Prieto Event 1 Feb 11 2008		Cerro Prieto Event 2 Feb 11 2008		Calexico Nov 20 2008		Calexico Dec 27 2008	
	ω (Hz)	ξ (%)	ω (Hz)	ξ (%)	ω (Hz)	ξ (%)	ω (Hz)	ξ (%)	ω (Hz)	ξ (%)
1	3.37	1.12	3.42	1.41	3.43	1.32	3.38	1.49	3.38	1.67
2	4.45	21.4	4.31	21.27	4.47	18.70	3.98	22.79	3.97	17.40
3	4.86	3.6	4.92	2.31	4.90	2.43	4.82	2.79	4.81	3.45
4	7.14	7.4	7.32	5.67	7.29	6.33	7.21	5.18	7.23	6.93
5	10.20	5.8	10.23	4.6	10.15	5.65	9.68	5.49	9.78	6.76
6	14.69	6.15	14.69	9.04	14.79	5.59	-	-	-	-

Table 7. RMS errors of measured data and predicted data by identified models of MRO

Sensor number	RMS error				
	Cerro Prieto Feb 8 2008	Cerro Prieto Event 1 Feb 11 2008	Cerro Prieto Event 2 Feb 11 2008	Calexico Nov 20 2008	Calexico Dec 27 2008
5	0.0328	0.0505	0.0565	0.0793	0.0583
7	0.0258	0.0378	0.0446	0.0628	0.0480
9	0.0330	0.0515	0.0559	0.0849	0.0586
16	0.0804	0.0990	0.0954	0.0939	0.1311
17	0.0718	0.0734	0.0936	0.1137	0.0920
18	0.0832	0.1081	0.1158	0.1044	0.1210
20	0.0806	0.0991	0.0940	0.0861	0.1274
21	0.0736	0.0809	0.1107	0.1267	0.0937

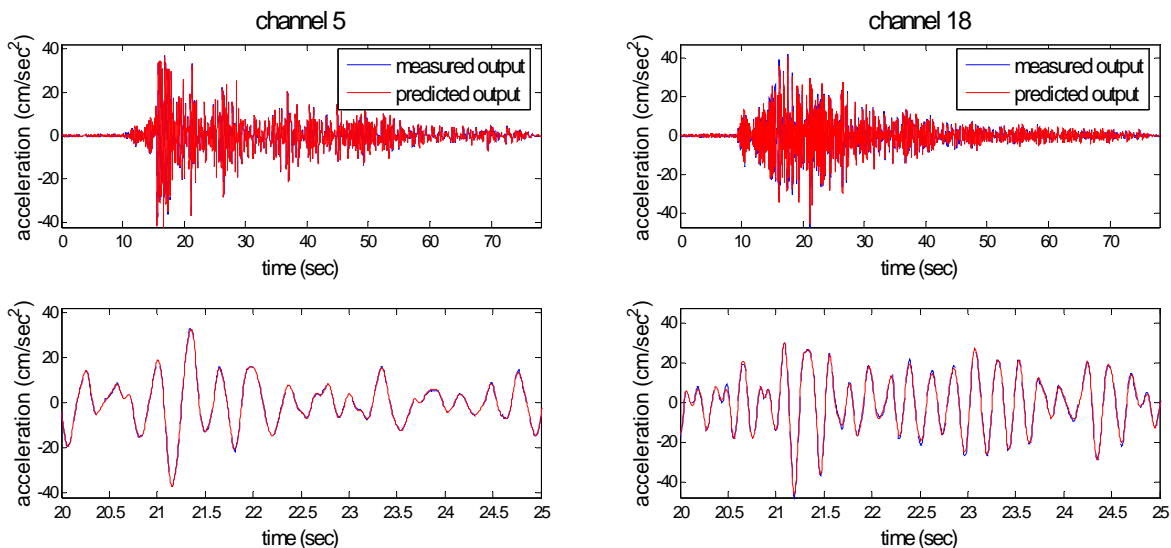


Fig. 5. Recorded and predicted acceleration data for channels 5 and 18 during Cerro Prieto Feb 8 2008 earthquake.

Each identified linear model should be able to reasonably predict the structural response for the other ground motions studied here, since they are of a small intensity and no large

damaging event occurred between these smaller events. The model identified for the input/output data from Calexico Dec 27 2008 was used to predict the structural response obtained with the input data from Cerro Prieto Feb 8 2008. Good agreement was found between the predicted and simulated data; plots for channels five and eight are shown in Fig. 6. The errors found are within acceptable limits.

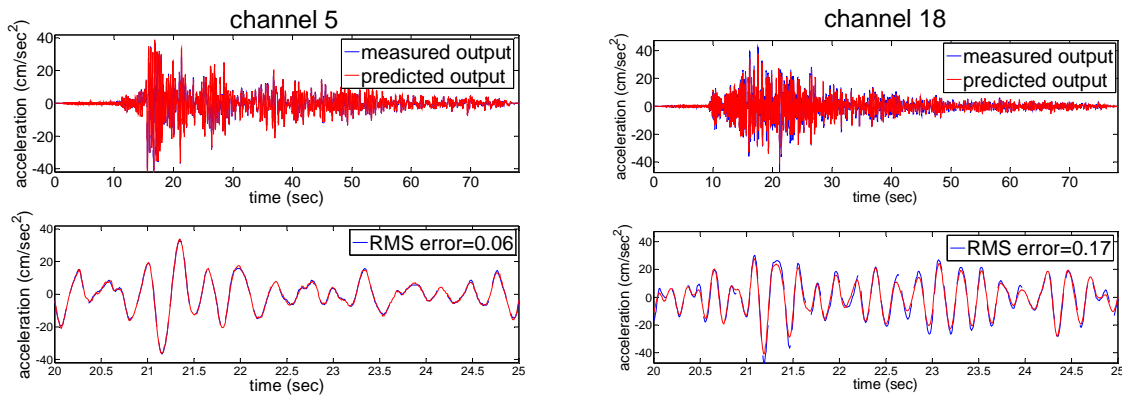


Fig. 6. Recorded and predicted acceleration data for channels 5 and 18 using data from Cerro Prieto Feb 8 2008 earthquake and linear model predicted with Calexico dec 27 2008.

Model updating

An initial finite element model of MRO was developed using SAP2000. The box girder and abutments were modeled with 3776 shells elements and the central pier and bent cap with 24 frame elements. The concrete was assumed to have a unit weight of 0.145 kip/ft³, a Poisson's ratio of 0.2 and a compressive strength of 3250 psi. As input, the displacement time histories from Cerro Prieto Feb 8, 2008, obtained also from the CSMIP website, were applied at the abutments and bottom of central pier.

To be able to accurately identify a reliable model of this bridge structure, the genetic algorithm was used to update the initial SAP2000 model. The objective was to match the frequencies found with ERA/OKID, as well as the measured acceleration time histories along the deck of the bridge with the frequencies and time histories from the FEM model. The fitness function was defined as the sum of the normalized errors of each identified (from ERA/OKID) and simulated (from SAP) frequency plus the sum of the normalized errors between the recorded acceleration time histories and those simulated by SAP.

At each generation of the GA, linear FEM analyses were performed in order to evaluate the fitness function for the new sets of parameters (one per each chromosome). Because of the small magnitude of the earthquake used, a linear analysis was considered appropriate for the model updating, keeping the computational costs low.

The parameters of the model selected to be updated were the elastic modulus of the concrete and the damping ratio parameters. The damping model used here was the Rayleigh damping, which assumes that the damping matrix is proportional to the mass and to the stiffness matrices through two coefficients. The choice of these 3 parameters to be updated was dictated by the fact that there are a lot of uncertainties about their magnitude and that they strongly influence the overall dynamic behavior. A range of possible values was selected for each

parameter. The elastic modulus of the concrete could vary between 460000 ksf and 560000 ksf, the mass coefficient between 0 and 2, and the stiffness coefficient between 0 and 0.01.

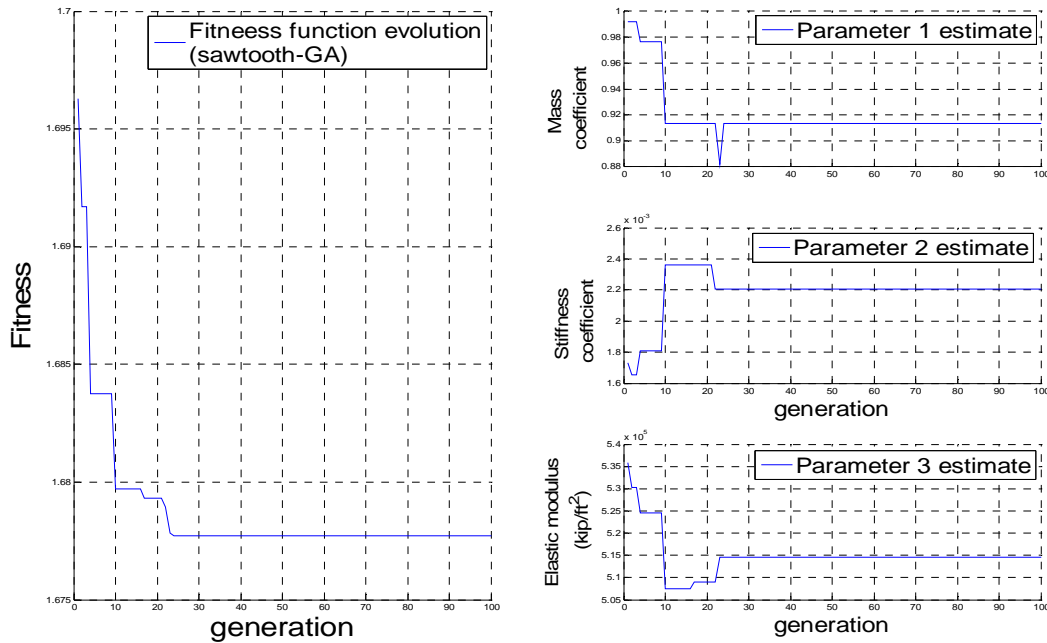


Fig. 7. Fitness function evolution and parameter evolution using genetic algorithm

Evolution of the fitness function and of the three parameters is presented in Fig.7. It was found that the optimized model will have an elastic modulus of 514,645.67 kip/ft² and the mass and stiffness coefficients will be 0.9134 and 0.0022 respectively.

In the Seismic Design Criteria [22] Caltrans suggests the elastic modulus can be approximated by

$$E_c = 57000\sqrt{1.3 * f'_c} \quad (\text{in psi}) \quad (14)$$

which, for an assumed $f'_c = 3250$ psi, corresponds to a magnitude 533,520 ksf. This value is relatively close to the optimal value found in the updating process, e.g. a difference of only 3.5% between them.

To test the accuracy of the updated FEM in reproducing the dynamic behavior of the real bridge, Fig. 8 compares the measured response from the Cerro Prieto Feb 8 2008 earthquake and the simulated one obtained by the updated FEM. Plots for channels 5 and 17 comparing acceleration time history, power spectral density of the acceleration and displacement time history are displayed. From plots, we can see that a good level of agreement was reached with the updating process.

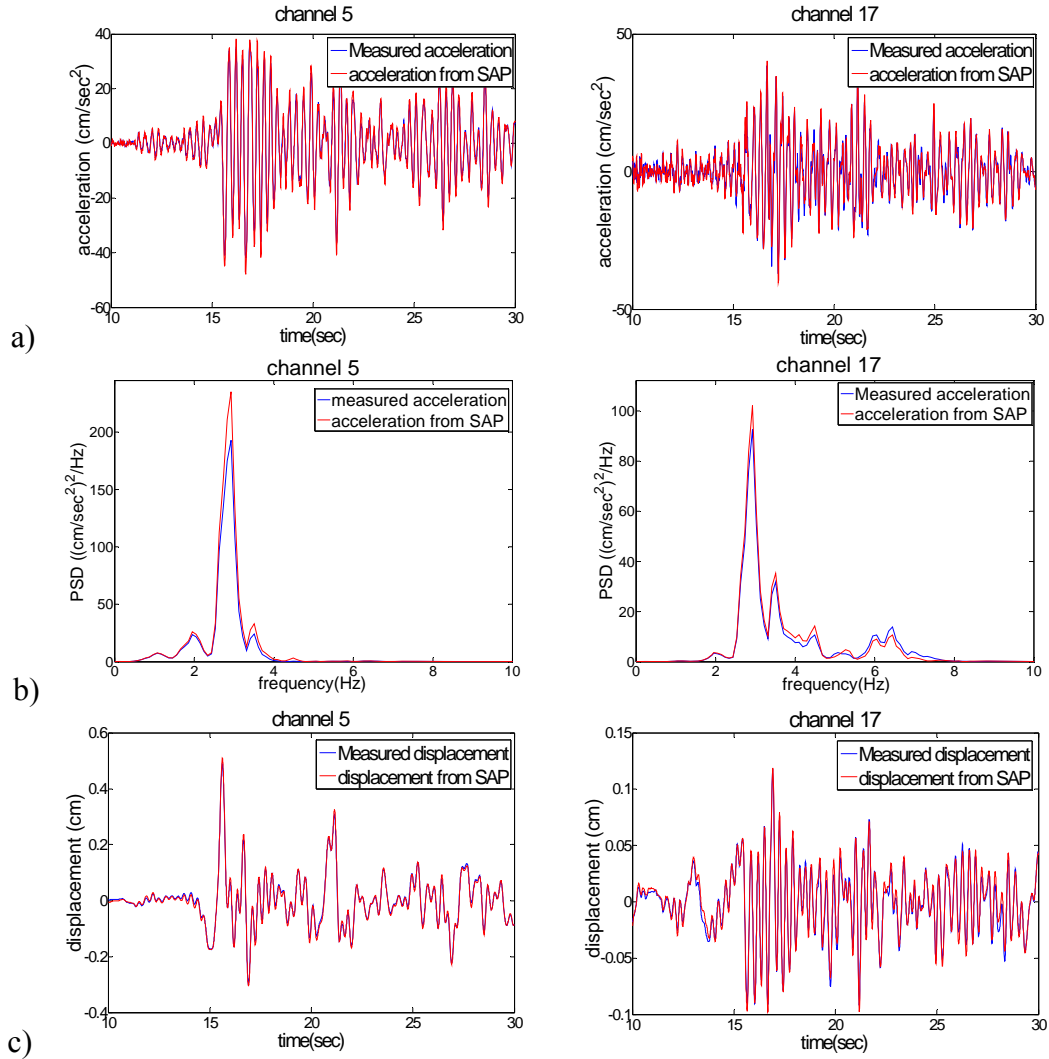


Fig. 8. Comparison of measured response and simulated response by updated SAP model for channels 5 and 7. a) acceleration time history, b) Power spectral density of acceleration, c) displacement time history

Table 8. Frequencies found with OKID and frequencies from FEM after calibration of the model

Mode	Mode description	Frequencies (Hz)	
		Identified with OKID	Calculated with FEM
1	Vertical anti-symmetric mode.	3.37 – 3.43	3.59
2	Transverse mode.	3.98 – 4.47	4.48
3	Vertical symmetric mode.	4.82 – 4.92	5.2
4	First torsional mode.	7.08 – 7.32	7.28
6	Second torsional mode of the whole length of the bridge.	9.68 – 10.2	10.4
10	Third torsional mode of the whole length of the bridge.	14.69 – 14.79	14.2

Table 9. RMS errors of measured data and data simulated by the FEM

Sensor number	Acceleration RMS error	Displacement RMS error
5	0.1576	0.0725
7	0.1416	0.0657
9	0.1633	0.0627
17	0.2252	0.1581
21	0.2345	0.1432
16	0.5218	0.3836
18	0.5584	0.4375
20	0.6462	0.4815

Table 8 shows the frequencies identified with OKID and the ones calculated with the updated FEM and Table 9 presents the RMS error between the measured data and the simulated ones by SAP for displacement and acceleration. From Table 8, it appears that the frequencies of the updated FEM model are within the range of values identified by ERA/OKID, with the exception of the one for mode 3 (slightly higher in FEM model) and the one of mode 10 (slightly lower). In looking at the RMS errors, (Table 9) it can be seen that the updating process was able to simulate the behavior of the first five channels, but it was not able to simulate channels 16, 18 and 20. This larger error on these few channels might be caused by the use of Rayleigh damping in the SAP model. If we compare Rayleigh damping with the values of damping identified by ERA/OKID (Fig. 9.), which is able to accurately predict those channels, we noticed that Rayleigh damping cannot model the damping of the structure for all the modes.

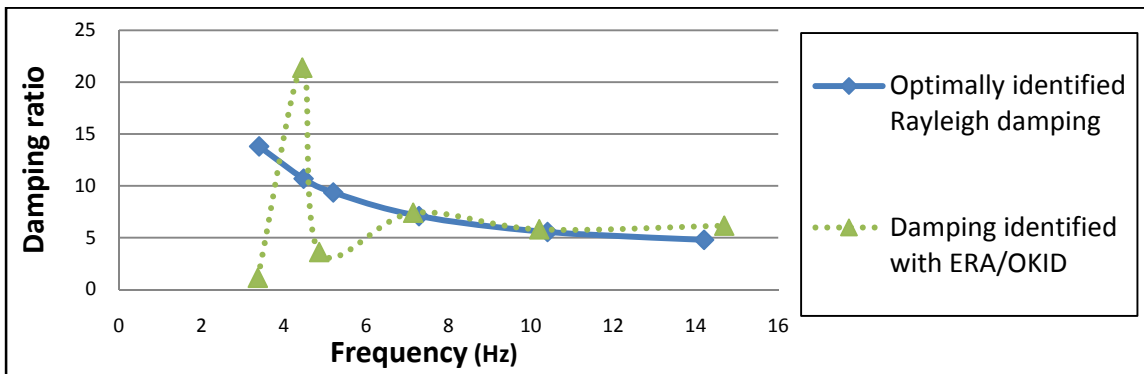


Fig. 9. Comparison damping ratios found using Rayleigh damping and identified by ERA/OKID

Since the acceleration time histories from channels 16, 18 and 20 were not simulated correctly, their data will not be used for the damage assessment.

Nonlinear analysis of the bridge using the updated finite element model

In order to perform a nonlinear analysis, fiber hinges were defined in the model at locations of potential damage as the column-deck and column-foundation connections as well as in the bent cap on each side of the column (Fig. 10). To define the fiber hinges the section of the columns and bent cap had to be divided into a discrete number of fibers. To select the number of fibers for the section, there has to be a balance between accuracy and computational cost: in this study, the column section and bent cap section were divided into four hundred fibers. Cross-sections and fiber distribution of the column and bent cap are shown in Fig. 11.

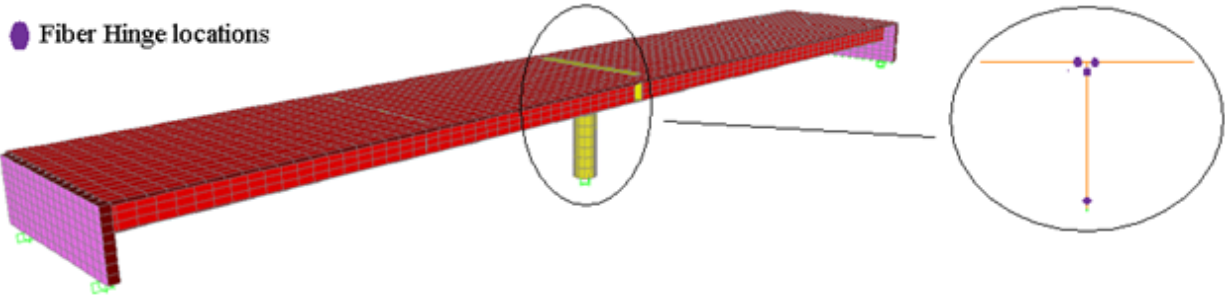


Fig. 10.FEM and fiber hinge locations

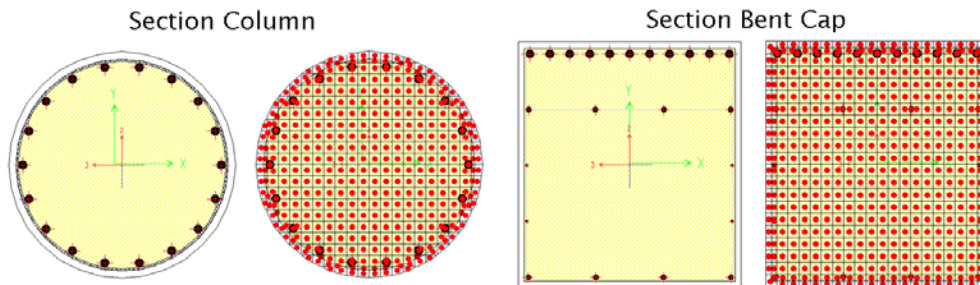


Fig. 11.Section of column and bent cap, and distribution of fibers

The fiber hinge defines its hysteretic behavior through the non-linear material models of the individual fibers [23], [24]; each fiber has a location, a tributary area and a stress-strain curve. For the concrete fibers, the Takeda model [25] was chosen; this model is suitable for concrete and other brittle materials. For the steel fibers, the multi-linear kinematic plastic model [26] was used; such a model is based on the kinematic hardening behavior, commonly observed in metals. Schematic plots of the models are shown in Fig. 12.

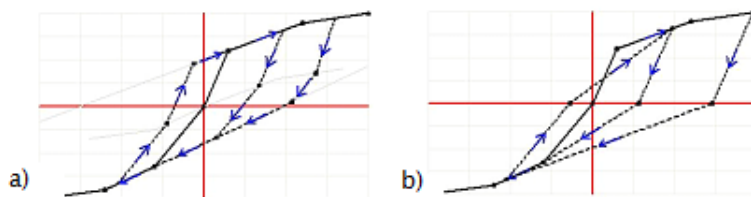


Fig. 12. Hysteretic models. a)Multi-linear kinematic, b)Takeda.

Having decided on the hysteretic behavior of the elements in the FEM, the ground motion time histories from one of the recorded earthquakes available from CSMIP was amplified by different factors and used as input on the FEM model so to induce various levels of nonlinearity on the bridge. These sets of data could simulate ground motions from a damaging earthquake. In Fig. 13 Moment-Rotation diagrams of the hinges at top and bottom of the column are presented for three amplification factors. In case a) the data from Cerro Prieto Feb 8 earthquake has not been amplified, and it is clear that the bridge behaves linearly. In the other two cases shown in Fig. 13, the displacement time histories from Cerro Prieto have been amplified by factors of fifty and one hundred. This amplified displacement time histories correspond to peak ground acceleration of 1.0 g and 2.0 g. For an amplification of fifty, the hinge at the bottom of the column presents nonlinear behavior, while the hinge at the top of the column is only starting to go into the inelastic range. For an amplification of one hundred, both the hinges at top and

bottom of the column clearly show a nonlinear behavior and will both be areas of potential damage. The hinges at the bent cap behave linearly for the first two cases, and start developing some non-linearity in the case where the data is amplified by one hundred.

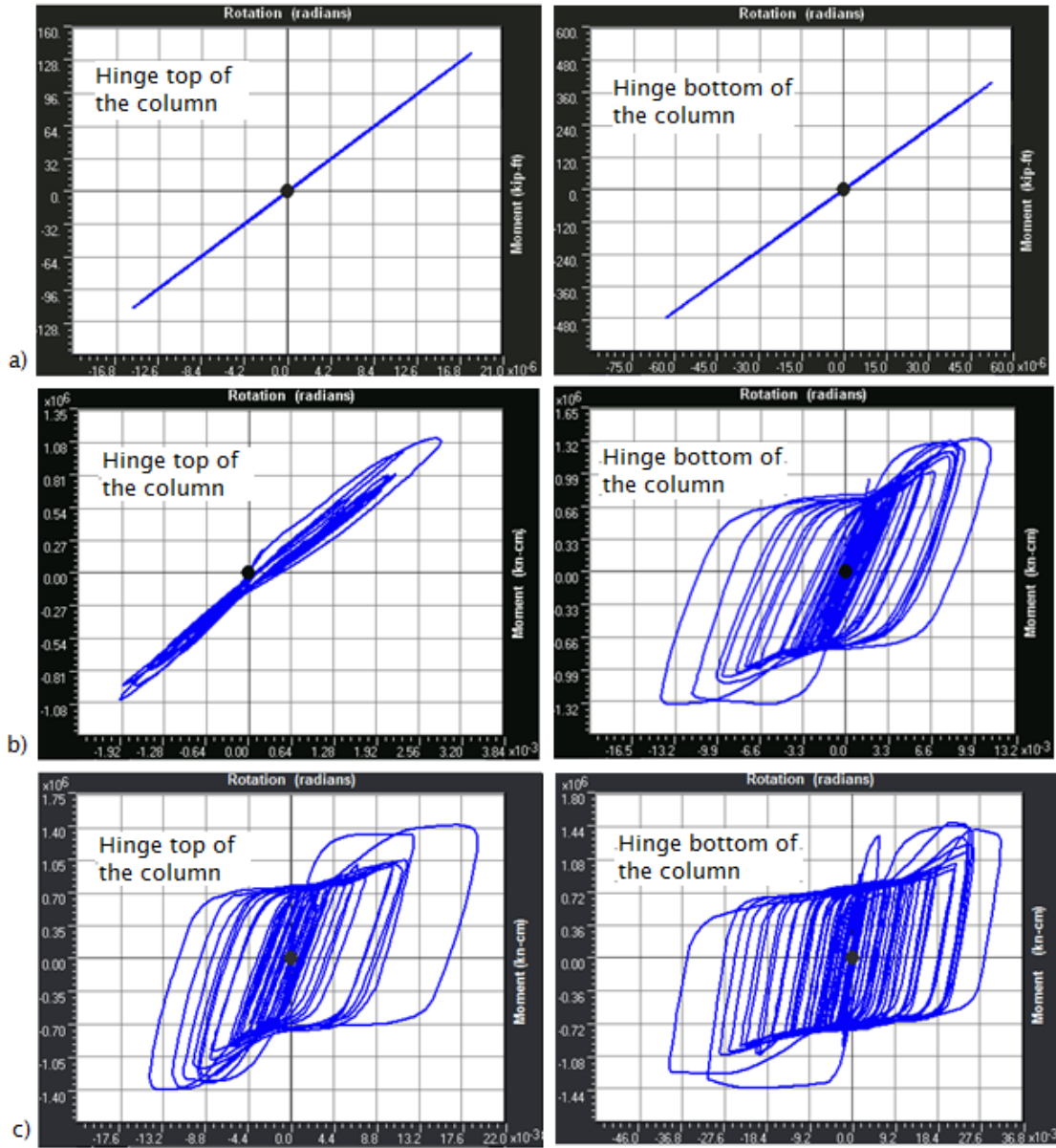


Fig. 13. Moment-Rotation diagrams of hinges at top and bottom of the column for Cerro Prieto Feb 8 Earthquake. a) Without amplification, b) Amplified by 50, c) Amplified by 100.

Table 10. RMS errors of data predicted by ERA/OKID (linear model identified with real data) and data simulated by the FEM

Channel	Acceleration RMS error		
	Original	Amplified by 50	Amplified by 100
5	0.1467	0.3139	0.4198
7	0.1343	0.3514	0.4763
9	0.1510	0.3175	0.4217
17	0.2284	0.3944	0.4600
21	0.2363	0.4042	0.4700

The linear model previously identified with ERA/OKID from the measured accelerations was used to predict the structural response for the different magnitudes of the earthquake. RMS errors of the predicted structural response and the simulated by the FEM are presented in Table 10. It can be seen that the errors increase as the nonlinearity in the structure or level of damage increases.

To show the bases of the damage detection technique used here and assure that the difference in the errors are due to damage in the bridge, a new linear model was determined with ERA/OKID using the data simulated with the FEM model for the case of no amplification of the ground motion. This model was then used to predict the bridge response for the different magnitudes of the earthquake. In Table 11, RMS errors of the data predicted with the linear model obtained with ERA/OKID and the data simulated by the FEM are tabulated. The table shows that, for the original earthquake, the RMS error is quite similar to the one obtained by looking at the real recorded data, an indication that ERA/OKID performs equally well with simulated as well as recorded data. In addition, it shows that the updated FEM model of the bridge provides an accurate representation of the linear behavior of the bridge. The same behavior observed using the linear model identified with ERA/OKID from the measured accelerations occurs here. The errors between the predicted response from the linear model identified with simulated data and the response from the nonlinear model increase as the nonlinearity in the bridge increase.

Table 11. RMS errors of data predicted by ERA/OKID (linear model identified with data simulated by FEM) and data simulated by the FEM

Channel	Acceleration RMS error		
	Original	Amplified by 50	Amplified by 100
5	0.0429	0.2267	0.3474
7	0.0121	0.2755	0.4136
9	0.0409	0.2255	0.3449
17	0.0982	0.2808	0.3391
21	0.1035	0.2945	0.3593

Looking at the time histories of the bridge's deck acceleration, the predicted response is almost identical to the actual response as long as the response remains linear as shown in Fig. 14a, but, as soon as the input is amplified and the response changes from linear to nonlinear, the linear model is no longer capable of predicting the structural response as shown in Fig.14b.

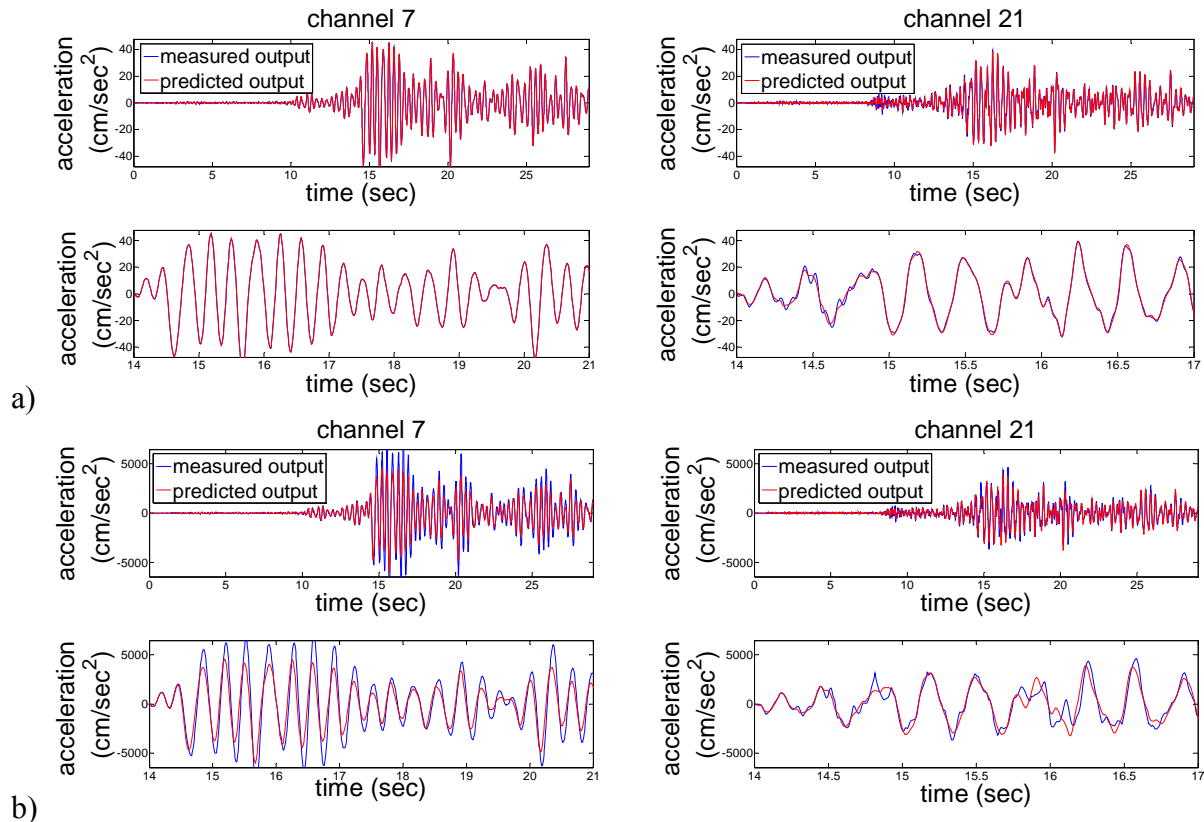


Fig. 14. Comparison of predicted response and simulated response by updated SAP model for channels 5 and 7. a) Acceleration time history, b) Power spectral density of acceleration

Conclusions

This paper presents a vibration-based damage detection technique. The difference between the actual measurement of the structural response and the predicted one by a linear state space model is used to detect damage. The basis of this technique is that a linear model developed using the ERA/OKID system identification technique will correctly predict a linear structural response but, if inelastic behavior (e.g. induced by damage) has occurred, the predicted response will deviate from the actual response.

Initially the ERA/OKID algorithm was applied using time histories of ground shaking and structural response of previous earthquakes. This algorithm, in addition to the high-fidelity linear first-order model later used to detect the presence on damage, provided dynamic characteristics of the structure (e.g. natural frequencies and damping ratios) that were used to update a FEM model of the bridge.

Although most modal updating processes only try to match modal parameters as frequencies and modal assurance criteria, here a more challenging updating process was performed trying to match the measured acceleration time histories at sensor locations, in addition to matching the frequencies of the structure. The numerical results from the updated model showed good agreement with the measured structural response as well as with the modal parameters identified. The model updating process used here shows potential for such a procedure to provide validated structural models of important structures.

The finite element model, updated following a GA, was used to simulate structural response for different levels of input excitation. Consequently, this resulted in increasing levels of structural damage. It was observed that the identified linear model could accurately predict the data if nonlinear behavior is not present, but, as the inelastic behavior grows, the error between the predicted and simulated data also grows.

The procedure used here to identify damage, can be implemented to give an almost immediate damage assessment after a seismic event. If a high-fidelity linear state-space model has been previously identified, when a new ground motion occurs, the data could be processed in near-real time and an estimate of the state of the bridge can be given. This is a rapid tool that can put up a green or red flag in a matter of few minutes after an earthquake.

Acknowledgements

The authors would like to gratefully acknowledge the support and guidance of Dr. Moh Huang and CSMIP which supported this study under contract CSMIP 1007-908. The authors would also like to acknowledge Eleni Chatzi for her guidance with the GA's, Luciana Balsamo for her work on the Rio Dell Overpass and Ah-Lum Hong for her advice on the application of the OKID-based algorithms.

References

- [1] Doebling SW, Farrar CR, Prime MB. A summary review of vibration-based damage detection and system identification methods. *Shock and vibration digest*. 1998; 30(2):91-105.
- [2] Mohamed AS. A data driven approach for earthquake damage detection. Master's thesis, The Graduate School of Natural and Applied Sciences, Atlim University. 2005.
- [3] Smyth AW, Pei JS, Masri SF. System Identification of the Vincent Thomas Suspension Bridge using Earthquake Records. *International Journal of earthquake and Structural Dynamics*. 2003; 32:339-367.
- [4] Lus H, Betti R, Longman RW. Identification of Linear Structural Systems using Earthquake-Induced Vibration Data, *Earthquake Engn. Struct. Dyn*. 1999; 28:918-929.
- [5] Arice Y, Mosalam KM. System identification of instrumented bridges. *Earthquake Engng Struct. Dyn*. 2003; 32:999-1020.
- [6] Juang JN, Pappa RS. An Eigensystem Realization Algorithm for modal parameter identification and model reduction. *J Guid control Dyn*. 1995; 8:620-627.
- [7] Juang JN, Phan M, Horta LG, Longman RW. Identification of observer/Kalman filter Markov parameters: theory and experiments. *J Guid Control Dyn*. 1993; 16:320-329.
- [8] Juang JN. *Applied system identification*. Prentice Hall, 1994.
- [9] Mottershead JE, Friswell MI. Model updating in structural dynamics: a survey. *J Sound Vib*. 1993; 165:347-375

- [10] Brownjohn JMW, Moyo P, Omenzetter P, Lu Y. Assessment of highway bridge upgrading by dynamic testing and finite element model updating. *J Bridge Eng.* 2003;8:162-172.
- [11] Zarate BA, Caicedo JM. Finite element model updating: Multiple alternatives. *Engineering Structures.* 2008; 30: 3724-3730.
- [12] Darrell Whitley. *A Genetic Algorithm Tutorial*, volume 4. 1994.
- [13] Brad L. Miller, Brad L. Miller, and David E. Goldberg. Genetic algorithms, tournament selection, and the effects of noise. *Complex Systems.* 1995; 9:193-212.
- [14] John H. Holland. *Adaptation in natural and artificial systems.* MIT Press, Cambridge, MA, USA. 1992.
- [15] Dudy Lim, Yew-Soon Ong, Yaochu Jin, and B. Sendhoff. Trusted evolutionary algorithm. *Evolutionary Computation. CEC 2006. IEEE Congress.* 2006; 149-156.
- [16] Chang-Yong Lee and Xin Yao. Evolutionary programming using mutations based on the levy probability distribution. *Evolutionary Computation, IEEE Transactions on.* 2004; 8(1):1-13.
- [17] Jinn-Tsong Tsai, Tung-Kuan Liu, and Jyh-Horng Chou. Hybrid taguchigenetic algorithm for global numerical optimization. *Evolutionary Computation, IEEE Transactions on.* 2004; 8(4):365-377.
- [18] Y. W. Leung and Y. Wang. An orthogonal genetic algorithm with quantization for numerical optimization. *Evolutionary Computation, IEEE Transactions on.* 2001;5:41-53.
- [19] David E. Goldberg. Sizing populations for serial and parallel genetic algorithms. 1989;70-79.
- [20] Micro-genetic algorithms for stationary and non-stationary function optimization, 1989.
- [21] C.P. Koumoussis, V.K.; Katsaras. A saw-tooth genetic algorithm combining the effects of variable population size and reinitialization to enhance performance. *Evolutionary Computation, IEEE Transactions on.* 2006;10(1):19-28.
- [22] Caltrans Seismic Design Criteria, Version 1.4, June 2006.
- [23] Filippou FC, Taucher FF. Fiber beam-column for non-linear analysis of RC frames: Part I. Formulation. *Earthquake eng. struct. dyn.* 1996; 25:711-725.
- [24] Filippou FC, Taucher FF. Fiber beam-column for non-linear analysis of RC frames: Part I. Applications. *Earthquake eng. struct. dyn.* 1996; 25:727-742.
- [25] Takeda T, Sozen MA, Nielsen NN. Reinforced Concrete Response to Simulated Earthquakes, *J. Struct. Engrg. Div., ASCE.* 1970; 96(12):2257-2273.
- [26] CSI Analysis Reference Manual for SAP2000, ETABS, and SAFE. April 2009.

COMPARISON OF RECORDED AND SIMULATED GROUND MOTIONS FOR TALL BUILDINGS

Jonathan P. Stewart¹, Lisa M. Star¹ and Robert W. Graves²

¹ Department of Civil & Environmental Engineering, University of California, Los Angeles
² URS Corporation, Pasadena, CA

Abstract

Seismic hazard for tall buildings in California is often dominated by large magnitude earthquakes for which few recorded accelerograms are available for response history analysis. In several recent manuscripts, we compare motions for an M_w 7.8 event on the southern San Andreas fault (known as the ShakeOut event), two ShakeOut permutations with different hypocenter locations, and a M_w 7.15 Puente Hills blind thrust event beneath downtown Los Angeles, to median and dispersion predictions from the empirical NGA ground motion prediction equations. The dispersion is represented by an intra-event standard deviation term, which is lower than NGA values at low periods and abruptly increases at 1.0 sec due to different simulation procedures at low and high periods. The simulated motions attenuate faster with distance than is predicted by the NGA models for periods under approximately 5.0 sec. This suggests ground motions away from the fault rupture are under-predicted by the simulation. After removing distance attenuation bias, we have found average residuals of the simulated events (i.e., event terms) are generally within the scatter of empirical event terms, indicating that the ShakeOut event is not unusually energetic for its magnitude. The simulated motions have a depth-dependent basin response similar to the NGA models, but also show complex effects in which stronger basin response occurs when the fault rupture transmits energy into a basin at low angle. The motions also indicate rupture directivity effects that scale with the isochrone parameter.

Introduction

This article is a brief overview of materials that have been submitted for publication elsewhere (Star et al., 2010a, 2010b).

Simulated ground motions have the potential to provide a valuable supplement to empirical methods, especially for large magnitudes and close site-source distances (e.g., $M_w > 7.5$ and distance < 20 km) for which recordings are sparse, especially for strike-slip earthquakes. In southern California, the design of duration-sensitive or long-period structures is often controlled by magnitude ~ 7.8 - 8.2 earthquakes on the southern San Andreas fault. There are very few recorded accelerograms that can be used for response history analysis for such conditions.

Simulation procedures that capture complex source features, path effects, and site effects can help fill this need. However, such techniques have not found significant practical

applications to date in the western United States because of a general sense among engineers that the simulated motions have not been adequately validated. This, then, raises the issue of how simulated motions *should* be validated.

Star et al. (2010a) present a procedure that checks key attributes of simulated motions relative to empirical observation, as represented by appropriate GMPEs. The procedure is appropriate for use with simulated motions that are both broad-band (i.e., span the range of periods of engineering interest) and are based on a simulation procedure that considers essential earthquake physics (i.e., source, path, and site processes). The Shakeout project (Jones et al., 2008) provides a convenient test case, as the motions for the M_w 7.8 earthquake on the southern San Andreas fault have the above attributes. Using motions from the ShakeOut event and other events, Star et al. (2010a) evaluate specific attributes critical to ground motion hazard analysis, including site-to-site variability, distance attenuation, source energy, basin response, and directivity effects. Star et al. (2010b) discuss the basin response and directivity effects in more detail.

Overview of Major Findings

Star et al. (2010a) investigate the degree to which the ground motions produced by simulations of major earthquakes on the San Andreas and Puente Hills faults are consistent with respect to specific attributes of NGA ground motion prediction equations (GMPEs), including source scaling, distance attenuation, and dispersion. They compare the intensity measures (peak acceleration, peak velocity, and spectral acceleration) with those predicted using the NGA GMPEs.

Analyses of intra-event residuals shows faster distance-attenuation of the simulated data relative to the GMPEs. This was interpreted as a shortcoming of the existing simulation routine that will be addressed in future research. They modify the GMPE distance parameters in order to match the distance attenuation of the synthetic models so that distance-bias is not mapped into the analysis of other effects. Using the modified GMPEs, they then perform a general comparison of the overall synthetic ground motions to the average ground motions predicted using the GMPEs for events of the same magnitude. This is accomplished through the analysis of event terms (inter-event residuals), which represent the average offset of the data (in this case, from the simulations) from a median model prediction (from the modified GMPE). They find that the event terms, while non-zero, are generally within a reasonable range relative to actual event terms from past earthquakes.

Star et al. (2010a) then examine the intra-event standard deviation to investigate the amount of scatter between different recordings of the same earthquake. They find that for short periods, the intra-event standard deviation values calculated from the simulated data are low compared to those given by empirical models. This indicates that the simulated models underpredict dispersion relative to GMPEs. There is a significant jump in the intra-event standard deviation values at about $T=1.0$ s that results from different simulation procedures at short and long periods. They interpret both the low dispersion at short periods and the jump as additional shortcomings in the simulation procedure that will be addressed in subsequent work.

Star et al. (2010a, 2010b) performed additional analysis of residuals from the modified GMPEs provided insights into basin and directivity effects. They generally observe ground motion increases with depth within basins, but also find complex interactions between basins and fault rupture. Among the most significant of those interactions are relatively strong motions within basins that open to the fault at low angle (i.e., when waves traveling along the fault strike can enter a basin with a small to modest “turn,” the basin response is strong). For rock sites, directivity effects at close distance ($R_{rup} < 40$ km) scale with the isochrone parameter in a manner similar to the Spudich and Chiou (2008) model. However, the coupling of basin and directivity effects described above often leads to average residuals within basins that are more strongly positive or negative than would be predicted by existing empirical models. It is not clear whether these differences reflect shortcomings in the empirical models or peculiarities in the simulated motions.

References

- Spudich, P., and Chiou, B., (2008). “Directivity in NGA earthquake ground motions: Analysis using isochrone theory,” *Earthquake Spectra* **24**. 279–298.
- Star, L. M., Stewart, J.P., and Graves, R. W. (2010a). “Comparison of ground motions from hybrid simulations to NGA prediction equations,” *Earthquake Spectra*, submitted.
- Star, L. M., Stewart, J.P., and Graves, R. W. (2010b). “Investigation of basin and directivity effects in broadband synthetic ground motion models,” *Ninth U.S. National Conference on Earthquake Engineering and 10th Canadian Conference on Earthquake Engineering*, submitted.

UPDATE AND NEW FEATURES OF THE CENTER FOR ENGINEERING STRONG MOTION DATA (CESMD)

Hamid Haddadi¹, Christopher Stephen², Anthony Shakal¹, Moh Huang¹, D. Oppenheimer², William Savage², William Leith² and John Parrish¹

¹ California Geological Survey

² U.S. Geological Survey

Abstract

The Center for Engineering Strong-Motion Data (CESMD) has been established by the U.S. Geological Survey (USGS) and the California Geological Survey (CGS) to provide a single access point for earthquake strong-motion records and station metadata from the CGS California Strong-Motion Instrumentation Program, the USGS National Engineering Strong-Motion Program, and the US Advanced National Seismic System (ANSS). This paper briefly summarizes the CESMD functions, describes the new developed features at the Center and gives an update on the data recently added to the CESMD database. Users can now download multiple records from different earthquakes and stations in zip file(s) that are separated by earthquake name and date and recording station. Registered users are notified of new significant earthquakes with strong-motion data. Highlights are added to the Internet Data Reports of significant earthquakes that summarize earthquakes details and give an overview of available strong-motion data. The CESMD Internet Data Reports for major earthquakes provide access to the references, such as papers and reports that were published on the earthquakes. For each earthquake, a summary of records parameters including station location, peak ground acceleration, velocity, displacement, and peak response spectral values are downloadable as a table that can be imported to a spreadsheet. All the functions and features of the Center are organized in a page named "About CESMD". Also, in this paper major earthquakes with strong ground motion data in CESMD that occurred since the SMIP 2007 seminar, in September 2007 are summarized.

Introduction

The Center for Engineering Strong Motion Data (CESMD) was established to provide timely, well-documented, and easily accessible data from domestic and international earthquakes of engineering interest. The CESMD was established by the USGS Earthquake Hazards Program and its National Engineering Strong-Motion Program (NESMP) and Advanced National Seismic System (ANSS), and the CGS Strong Motion Instrumentation Program (CSMIP). The Center is responsible for receiving US data from field stations, uniformly processing the data, rapidly releasing it through the Web, and archiving the data. In addition to strong-motion records, the Center provides information about site characteristics of stations (e.g., Vs30 and near-surface geology), and station characteristics such as structure type, height, and seismic design for instrumented structures, and a photograph showing the station surroundings.

The Center is engaged with the Consortium of Strong Motion Observation System (COSMOS) in the process of transitioning the COSMOS Virtual Data Center (VDC) to integrate it with the CESMD for improved efficiency of operations and to provide all users with a more convenient one-stop portal to both US and international strong motion data. The Center is working with COSMOS and international and US data providers to improve the completeness of site and station information, which are needed to most effectively use the recorded data.

CESMD Operation

The Center is managed by a Center Management Group (CMG), which consists of representatives from the CGS and USGS to coordinate policies and to oversee operation, coordination, and standardization of the CESMD. The Center Advisory Committee consists of researchers and practitioners from the engineering, science, and emergency response fields, and provides advice to the CMG on directions, goals and services.

CESMD Threshold for Data Inclusion

The threshold for including earthquakes in the Center's database depends on earthquake magnitude, peak ground acceleration and the seismic region (Figure 1). An earthquake in the US with magnitude 4.5 and larger that has a record with peak ground acceleration exceeding 5%g is included in the data center. However, the threshold for including earthquake is lowered to magnitude 4.0 in Center and East US. International earthquakes with magnitude 5.5 and larger that have records with peak ground accelerations of minimum 10%g are included in the CESMD.

CESMD Web Site

The CESMD provides strong-motion data, metadata about stations and sites, and other services such as a search engine and interactive maps of events and stations through its web site. The web site is also the means of communicating between the Center and users in order to get feedback, answer questions regarding the data, and inform users about the updates at the Center. The web site, hosted by CGS and USGS at <http://www.strongmotioncenter.org>, consists of three major sections: Internet Quick Reports (IQR), Archive, and Search Engine. The front page of the Center's web site is shown in Figure 2. In addition to serving as a data source, the Center notifies users when new data from earthquakes with magnitude 5.0 and larger are available, and when pages are significantly updated.

The CESMD's web site is a dynamic web site in which all the web pages are generated on-the-fly upon a user's request. Data are retrieved from a database in real time when a user opens a web page. The dynamic nature of the database-driven system ensures that tables and maps will always contain the most updated information.

The Internet Quick Reports

The CESMD provides the most current strong-motion data of engineering interest through the Internet Quick Reports (IQR) that are generated shortly after earthquakes. The first version of the IQR is often released within 30 minutes after the event. More complete IQR pages are posted as data are recovered and received by the Center. The Center plans to automate preliminary data processing and dissemination in the near future, which will make the information available more rapidly. An example of an IQR event summary page is shown in Figure 3. The user can access the Internet Quick Report for individual events by clicking on the event name on an event summary page of the IQR web page.

Archive

The Archive pages are sorted by event date (most recent on top). The layout of the Archive pages is the same as that of the IQR pages, so a user familiar with the IQR will find it easy to use the Archive pages. Concurrent with the accumulation of data from new and recent events, the CESMD also is loading additional significant strong-motion records for historic earthquakes to the Archive.

Searching for Data

Strong motion records of the Center are searchable using the “Search for Data” button on the Center’s front page. Clicking on this button will display a search page that currently includes two search options, one for the CESMD and one for the COSMOS Virtual Data Center (VDC). Currently these two options are needed because the extent and scope of data holdings as well as the search options of these two data centers are incongruent (presently the VDC provides access to worldwide data). Future plans include incorporation of the VDC into the CESMD so that users will be able to access both U.S. and significant international data through the CESMD web site.

The current search page of the CESMD for U.S. structural and ground response data is shown in Figure 4. The records in the CESMD archive are searchable in several ways, depending upon a user’s interests. In general, the search parameters can be a combination of earthquake, station, and record parameters. The searchable earthquake parameters are currently earthquake name, magnitude and date. The station parameters are station city, station name, number, and type. The station types include ground stations, buildings, bridges, dams, geotechnical arrays, and others. For building stations, additional search parameters include material of construction (such as steel, concrete, masonry and wood), whether or not there is base-isolation, and the height (low, mid, and high rise). The search table can be sorted in the same way as an IQR or Archive table. The records found are directly viewable and downloadable from the search result table as shown in Figure 5.

The Center provides ambient vibration data recorded at some of the requested CGS stations through the search engine. The ambient data are loaded at the ftp site, linkable through a button at the bottom of the CESMD link on the Search for Data page.

Interactive Map for Earthquake

The CESMD includes interactive Google Maps that allow users to view maps of strong motion stations and events. This feature makes use of the Google Maps web service. An example of the map interface for an IQR page is shown in Figure 6. The map shows the earthquake epicenter and the stations that recorded the Inglewood earthquake of May 17, 2009. The station symbols (circles for ground sites, squares for structures) are colored according to maximum horizontal acceleration (PGA), so a user can see at a glance where the highest ground motions were recorded. The corresponding legend of PGA values appears in the upper right corner of the map. For consistency and ease of use, the colors used in the symbols correspond to the coloring used on ShakeMap for that acceleration. Many standard features of Google Maps are also present. For example, the inset at the lower right corner of the map provides regional context, a distance scale is displayed at the lower left corner of the map, standard navigation tools (zoom, translation) appear in the upper left of the map, and the base map view (Map, Satellite, Terrain) can be selected at the upper right. These features allow the user to interactively drag or pan the map around using either the left mouse button (click and drag), or the arrows at the upper left corner of the map. The button in the middle of those arrows (with four arrows pointing inward) will bring the user back to the previous map coverage. The map can also be panned by clicking and dragging the blue rectangle inside the regional overview map.

When the mouse hovers over a station on the map, a photo of the station appears beside the map at the lower right, along with some information about the station. The user can also click on the station to open a pop-up window containing basic information about the station and links to view the time histories and download the strong-motion data. Clicking on the epicenter opens a pop-up window providing the basic information on the earthquake.

A feature has been added in the Interactive Map that allows users to download a file with station information in KML format so that it can be viewed in three dimensions in the Google Earth viewer.

New Developments

The CESMD is working to implement modifications and enhancements to existing search options and display features in response to suggestions from the Center Advisory Committee, and also working to implement automatic data collection and preliminary processing and dissemination. The goal is to provide at least preliminary versions of US strong-motion data through the Center within a few minutes after a significant event and fully verified data soon afterwards. The records from all ANSS strong-motion networks will be uniformly processed and provided. The new developments at the Center from the time of the September 2007 annual SMIP seminar to now are described briefly in the following.

About CESMD

For users who visit the CESMD web site for the first time, it may be useful to start with the page linked through the front page named “About CESMD” (Figure 7). This page provides a

summary of the CESMD history and background, the Center's functions and features, information such as data formats, contact information, questions about the Center, etc. Also, this page may be useful for the returning users as a reference and one stop page that provides links to all CESMD pages and information about the Center.

Users Notification

The Center notifies registered users when new earthquakes with magnitude 5.0 and larger are posted and when an existing page is significantly updated. Users can register at the CESMD by going to "About CESMD" link through the front page.

Stations and Earthquakes Maps

The Interactive Station Maps provide maps of all network stations. In the time being, the station maps are available for the Northern California and Southern California areas. The maps also include stations that are planned or underway. Each station on the map is color coded to represent its seismic network. Also, users can access all data from different events recorded at any station by clicking on the station button on the map. Figure 8 shows the station map for the Southern California area.

The Interactive Earthquake Event Map (Figure 9) is another new tool using Google Map that shows all the earthquakes with strong-motion records available in the CESMD. The events are color coded to easily distinguish the significant events that have important strong-motion records from smaller events. By clicking on an event a pop-up window will provide a link to the list of all stations that have strong-motion records for that event. Thus all the data recorded and loaded in the CESMD for a station is easily downloadable and viewable through the Interactive Event Map.

Multiple Records Download

Users are able to select multiple files of processed or raw data to download through Internet Quick Report, Internet Data Report, and Search for Data pages. Figure 10 shows an example of a download page. The page summarizes availability of data for download. Data are downloaded in zip files, as shown in Figure 11, with standard identifiers including earthquake name and date, network code and station number/code.

Earthquake Highlight

For earthquakes with significant strong ground motion records in the Center, the earthquake and available records are summarized in an Earthquake Highlight. Figure 12 shows the Highlight for the 17 May, 2009 Inglewood earthquake. For the recent earthquakes, Highlights include a figure that shows variation of peak ground acceleration versus distance that would provide an overview about the records and also attenuation of ground motion with distance.

Data References and Reports

For the major earthquakes in CESMD, there are reports and papers available about strong motion data and processing that are helpful for users to understand recorded data and facilitate data application. In the CESMD Data Reports, the reports and references are available through a link on the upper left side of the major earthquakes pages named “Reports”. Users are recommended to review the reports, when available, before using data in their research or project. Figure 13 shows the reference page for Northridge earthquake of January 17, 1994. It is worth noting that the purpose for the Report page is not to list and give reference to all research papers available about an earthquake, but to highlight points about strong-motion data and processing of data.

Summary of Records in Table

In each earthquake page of the CESMD, there is a link, on the upper left, named “Download Text Table”. This link provides a text table of all stations records with information about station latitude and longitude, maximum recorded ground acceleration, velocity, displacement, and maximum response spectral acceleration at periods 0.3, 1.0 and 3.0 seconds. For structures, the peak ground acceleration at structure is also given in the table. This table is useful for users who need to import the information to a spreadsheet.

Update on Available Data

As of November 2009, 4855 station records from 174 earthquakes in the US and other countries with magnitudes 4.0 and larger have been loaded into the CESMD database. Figure 14 shows number of earthquakes and station records in different magnitude ranges. Each station record consists of 3 components for ground response stations and more, up to over 100 components for some structural stations.

Earthquakes loaded to the CESMD database from the time of SMIP07 seminar, in September 2007 to now are summarized in Table 1. As shown in the table, 61 earthquakes with magnitude 4.0 and larger that were recorded at 1740 stations in the ANSS seismic regions were processed and loaded to the CESMD in this time interval. Among the US earthquakes, M5.4 Alum Rock earthquake of 30 October 2007 has records at 224 stations and M5.4 Chino Hills earthquake that occurred on 29 July 2008 was recorded widely in southern California at over 420 stations.

During the time period of SMIP07 to SMIP09, 5 international earthquakes with magnitude 5.8 to 8.4 were added to the CESMD. The largest one was M8.4 Sumatra earthquake that occurred on 12 September 2007 with 2 aftershocks with magnitudes 7.9 and 7.0. The earthquake and aftershocks were recorded at Caltech Tectonics Observatory (CTO) station PSKI. The records were processed by the USGS National Strong Motion Project (NSMP) staff and are available at the CESMD. Figure 15 shows acceleration, velocity and displacement of the M7.9 aftershock that occurred at distance 164 km from the epicenter on September 12, 2007 with maximum peak ground acceleration of about 13%g and peak ground displacement of about 16

cm. Due to long period contents of ground motion, periods up to 50 seconds were allowed to pass in the processing of this records' data.

An earthquake with magnitude 5.8 ML (6.3 Mw) occurred on April 6, 2009 in Central Italy about 5 km southwest of the city of L'Aquila (about 85 km northeast of Rome), causing extensive damage in the area. The earthquake strong motion was recorded by 55 modern stations of the Italian National Strong Motion Network (RAN) managed by the Department of Civil Protection (DPC). Teams of U.S. earthquake researchers, sponsored by EERI, PEER, and GEER and others visited the area to document scientific and engineering effects of the earthquake, and assisted CESMD in receiving the strong motion data and background information. The largest acceleration, about 65%g, was recorded at about 5 km from the epicenter. The largest velocity, about 42 cm/sec, was obtained at this station. There are 4 strong motion stations within about 6 km of the epicenter, and they all recorded over about 35%g. The peak ground velocity at these stations ranges from 32 to 42 cm/sec.

An earthquake with magnitude 8.0 occurred on 29 September 2009 in Samoa Islands region. Peak ground acceleration of about 10%g was recorded at distance 179 km at station AFI by IRIS/USGS Global Seismograph Network. This record is also among the few records available from very large earthquakes.

Summary

- The Center for Engineering Strong Motion Data, CESMD, is a cooperative effort of the California Geological Survey and the US Geological Survey to establish a unified strong-motion data center for engineering applications.
- Nationwide records with threshold magnitude of 4.5 and peak ground acceleration of 5%g are included in the CESMD. For the ANSS region of Center and East US only, the threshold magnitude is lowered to M4.0
- Users are notified by the Center when new significant earthquakes are loaded to the Center.
- New station maps are available for the southern and northern California regions. Data is viewable and downloadable from the station maps.
- The All Earthquakes Map includes all the earthquakes loaded into the Center's database. Users can access to the Internet Report pages and station maps of earthquakes from the All Earthquakes Map.
- Multiple records can be downloaded in zip files that are named by earthquake date, earthquake time and station name/code. This format allows users to search earthquakes and records and download and organize the files locally on the user's computer.

- Earthquake Highlights provide information about significant earthquakes and plots of recorded acceleration versus distance.
- A new button named “Report” links to the references and reports published about records and data processing of the major earthquakes records.
- Since the SMIP 2007 annual seminar in September 2007, the CESMD has loaded records from over 1760 stations from earthquakes in the US and other countries.

Acknowledgement

We acknowledge and thank the CESMD advisory committee for providing us with their advice to improve the functionality of the Center. The efforts of Jessica Zhang for updating and maintaining the database of the Center are acknowledged.

References

Haddadi, H., A. Shakal, C. Stephens, W. Savage, M. Huang, W. Leith, R. Borchardt and J. Parrish (2008). Center for Engineering Strong-Motion Data (CESMD), 14th World Conference of Earthquake Engineering, Beijing China.

Lin, Kuo-wan, A. Shakal, M. Huang, C. Stephens, and W. Savage (2002). Dissemination of Strong-Motion Data Via the Internet Quick Report and the Internet Data Report at the CISN Engineering Data Center, Proceedings of SMIP2002 Seminar on Utilization of Strong-Motion Data, p. 115-126.

Shakal, A., and C. Scrivner (2000). TriNet Engineering Strong-Motion Data Center, Proceedings of SMIP2000 Seminar on Utilization of Strong-Motion Data, p. 115-124.

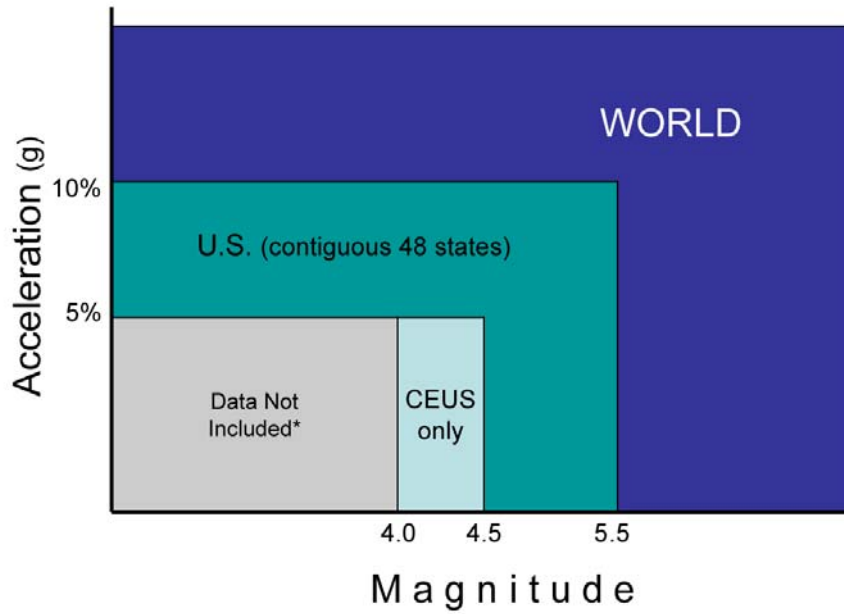


Figure 1. The CESMD thresholds for earthquake magnitude and acceleration.

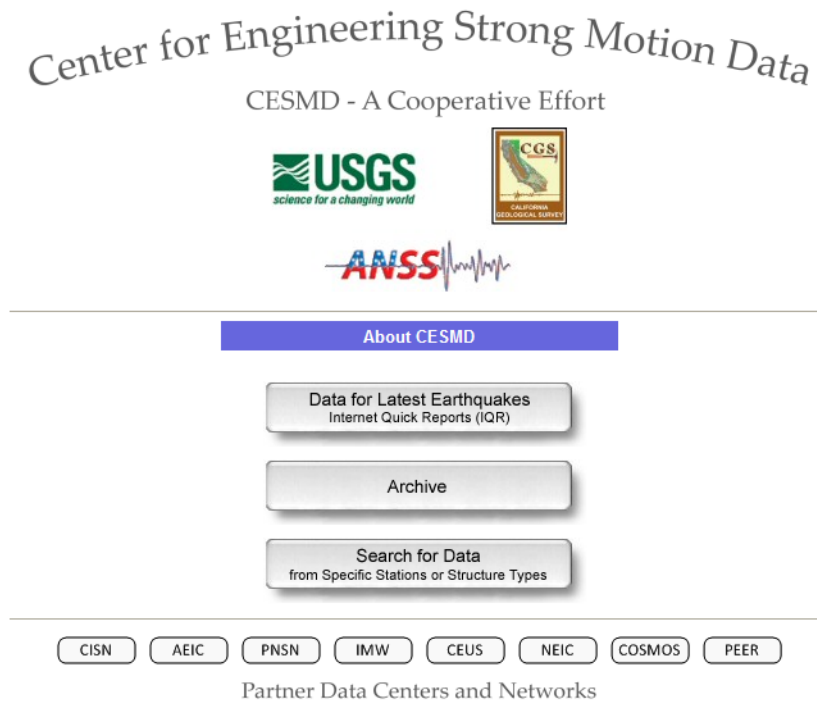


Figure 2. The CESMD web site front page at strongmotioncenter.org

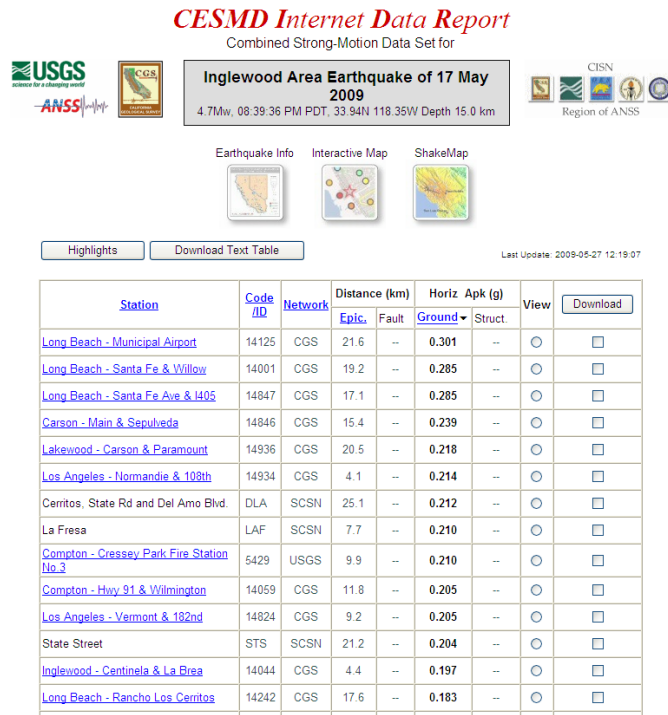


Figure 3. The Internet Data Report web page for the Inglewood earthquake of 17 May 2009.

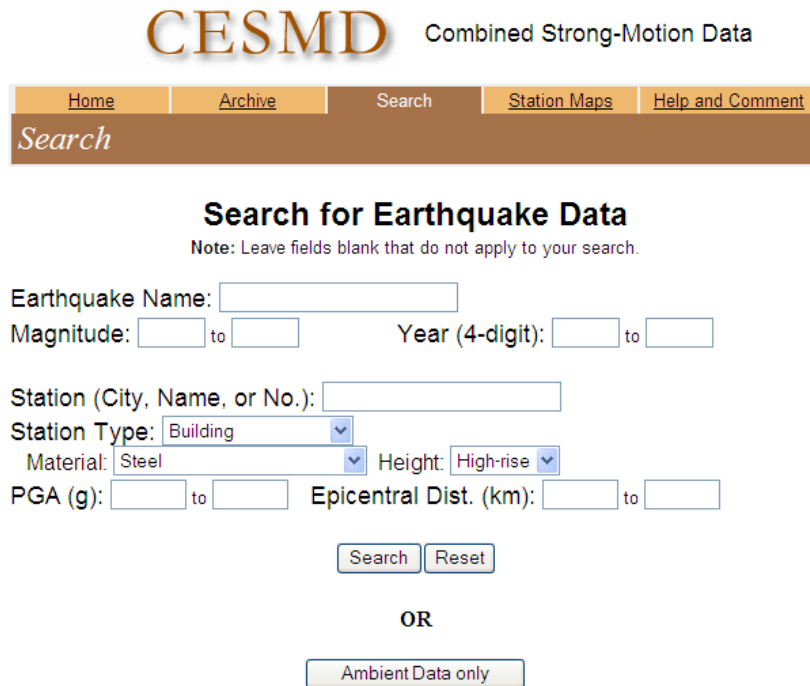


Figure 4. CESMD search page shows a search request for steel high-rise buildings data.

CESMD Combined Strong-Motion Data

Home Archive Search Help and Comment

Search

101 records match the following search parameters

Station (City, Name or No): Any Station type: Building
 Station Material: Steel Station Height: High-rise
 PGA (g): Any Epicentral Dist. (km): Any

StaNo	Station	Network	Epic (Fault) Dist.(km)	Horiz Apc (g)		Earthquake	View	Download
				Ground	Struct.			
14654	El Segundo - 14-story Office Bldg	CGS	4.6(-)	0.047	0.060	Inglewood 17May2009	<input type="radio"/>	<input type="checkbox"/>
58675	Oakland - 18-story City Hall	CGS	7.3(-)	0.017	0.068	Piedmont 20Jul2007	<input type="radio"/>	<input type="checkbox"/>
58312	Oakland - Harris State Building	CGS	7.6(-)	0.016	0.033	Piedmont 20Jul2007	<input type="radio"/>	<input type="checkbox"/>
58638	Concord - 9-story Office Bldg	CGS	9.8(-)	0.044	0.128	Lafayette 01Mar2007	<input type="radio"/>	<input type="checkbox"/>
24713	Los Angeles - 8-story Hospital	CGS	10.8(-)	0.090	--	W/Hollywood 9Sep2001	<input type="radio"/>	<input type="checkbox"/>
58638	Concord - 9-story Office Bldg	CGS	12.5(-)	0.006	0.015	Alamo 05Sep2008	<input type="radio"/>	<input type="checkbox"/>
57318	San Jose - 18-story City Hall	CGS	14.2(-)	0.072	0.152	AlumRock 30Oct2007	<input type="radio"/>	<input type="checkbox"/>
57357	San Jose - 13-story Govt Office Bldg	CGS	14.3(-)	--	0.084	AlumRock 30Oct2007	<input type="radio"/>	<input type="checkbox"/>
24288	Los Angeles - 32-story Residential Bldg	CGS	15.8(-)	0.016	0.011	Inglewood 17May2009	<input type="radio"/>	<input type="checkbox"/>
14654	El Segundo - 14-story Office Bldg	CGS	17.2(-)	0.007	--	W/Hollywood 9Sep2001	<input type="radio"/>	<input type="checkbox"/>
24249	Los Angeles - 8-story County Hospital	CGS	18.4(-)	0.010	0.018	Inglewood 17May2009	<input type="radio"/>	<input type="checkbox"/>
24248	Los Angeles - 9-story County Hospital	CGS	18.5(-)	0.012	0.024	Inglewood 17May2009	<input type="radio"/>	<input type="checkbox"/>

Figure 5. A part of the search result for steel high-rise building data.

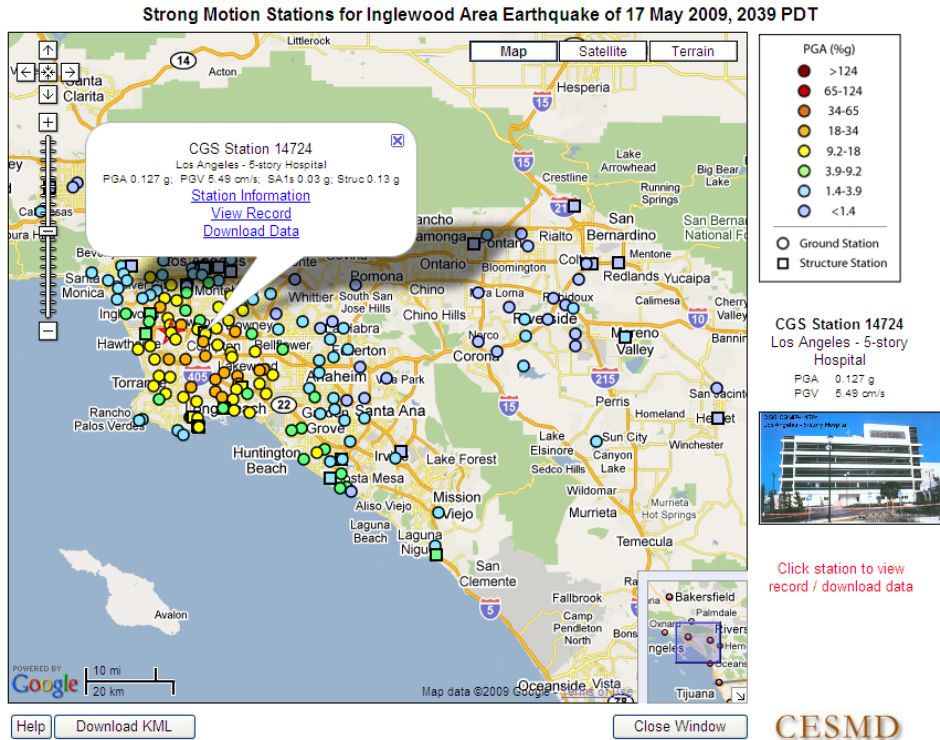


Figure 6. Station map for Inglewood earthquake of May 17, 2009.

About CESMD

Our Products	Data Format
Internet Quick Report Archive Search Engine Stations Map Earthquakes Map Notification	COSMOS Format COSMOS Tables CGS Format SMC Format
CESMD Center	Tools
History CMG & Advisory Committee ANSS Regions	COLUMIZE for input to Excel!
More	
Register at CESMD Contact us Questions and Answers Seismic Networks and Centers	



Figure 7. The “About CESMD” page summarizes the CESMD.

Strong Motion Stations in Southern California

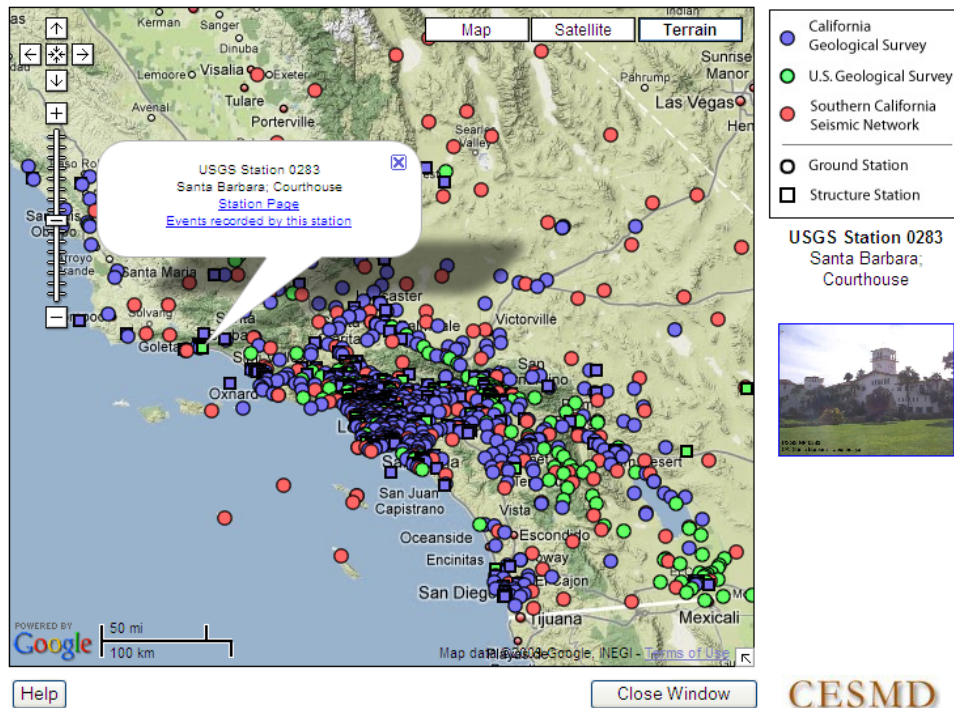


Figure 8. Station map of the Southern California area.

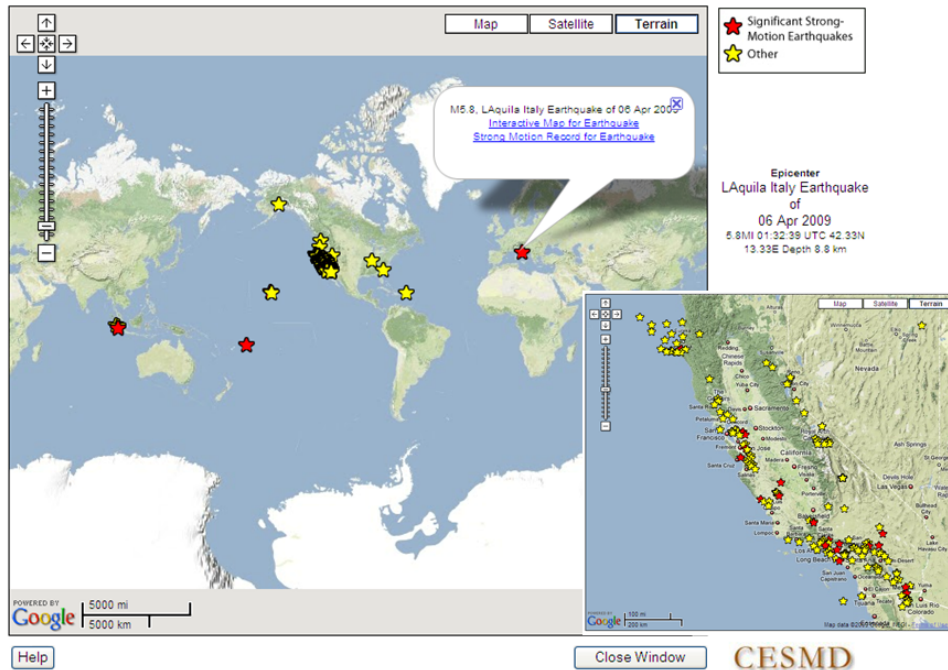


Figure 9. Interactive map of All Earthquakes.



Figure 10. Multiple download of records. Stations are check marked to be downloaded.

Name	Type	Modified	Size	Ratio	Packed	Path
Inglewood_17May2009_CE14001P.ZIP	WinZip File	5/18/2009 2:55 PM	265,216	0%	265,140	
Inglewood_17May2009_CE14044P.ZIP	WinZip File	5/18/2009 11:56 AM	240,356	0%	240,150	
Inglewood_17May2009_CE14059P.ZIP	WinZip File	5/18/2009 11:56 AM	245,632	0%	245,496	
Inglewood_17May2009_CE14125P.ZIP	WinZip File	5/19/2009 4:54 PM	235,158	0%	235,027	
Inglewood_17May2009_CE14824P.ZIP	WinZip File	5/18/2009 2:55 PM	244,576	0%	244,138	
Inglewood_17May2009_CE14846P.ZIP	WinZip File	5/18/2009 2:55 PM	248,294	0%	247,971	
Inglewood_17May2009_CE14847P.ZIP	WinZip File	5/18/2009 11:56 AM	250,367	0%	250,129	
Inglewood_17May2009_CE14934P.ZIP	WinZip File	5/18/2009 11:56 AM	233,891	0%	233,658	
Inglewood_17May2009_CE14936P.ZIP	WinZip File	5/18/2009 2:56 PM	235,763	0%	235,588	
Inglewood_17May2009_CIDLAP.ZIP	WinZip File	5/18/2009 11:59 AM	321,070	0%	320,461	
Inglewood_17May2009_CILAFP.ZIP	WinZip File	5/18/2009 12:00 PM	322,608	0%	322,475	
Inglewood_17May2009_CIST5P.ZIP	WinZip File	5/18/2009 12:00 PM	321,849	0%	321,552	
Inglewood_17May2009_np05429P.ZIP	WinZip File	6/25/2009 6:10 PM	616,822	0%	614,241	

Figure 11. Data downloaded in zip files. The files are named in a standard format of earthquake name_Earthquake date_Network+station number/code+data type (Processed or Raw).

Inglewood Earthquake of 17 May, 2009

The earthquake magnitude 4.7Mw occurred in a densely populated part of Los Angeles area about 2 km south of Inglewood at 8:39 PM PDT, on May 17, 2009. According to the [Southern California Seismic Network](#), it is likely that this earthquake is associated with the Newport-Inglewood fault. The right lateral strike slip focal mechanism of this earthquake is consistent with slip on the Newport-Inglewood fault. The damaging 1933 M 6.4 Long Beach earthquake was located 40 km to the southeast, also on the Newport-Inglewood fault.

The earthquake of 17 May was recorded widely by the strong motion stations of the CISN network. The largest acceleration was about 30% g at Long Beach Municipal Airport, about 22 km south east of the epicenter. The variation of Peak Ground Acceleration (PGA) versus epicentral distance is shown in the following figure. The figure shows significant variation of PGA at distances of 10 to 30 km from the epicenter.

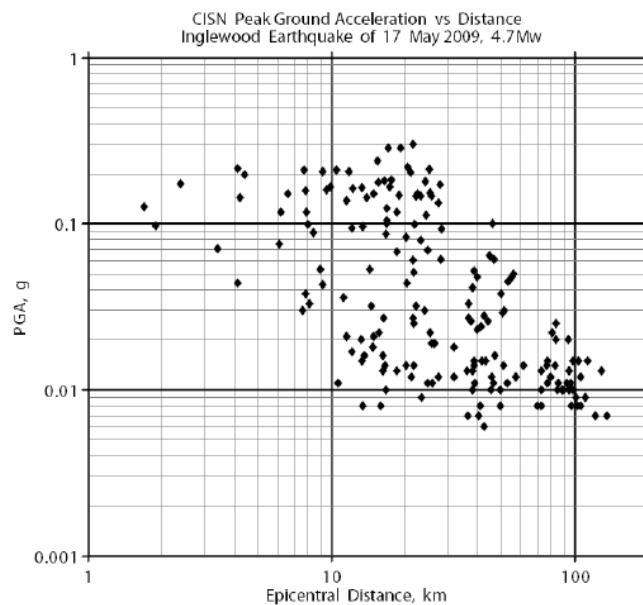


Figure 12. Earthquake highlight page for 17 May 2009, Inglewood earthquake.

References for Northridge Earthquake of January 17, 1994

- General Reports

- [CSMIP Strong-Motion Records from the Northridge Earthquake of January 17, 1994, CGS Publication OSMS 94-07.](#)
- Accelerograms Recorded at USGS National Strong-Motion Network Stations During the Ms=6.6 Northridge California Earthquake of January 17, 1994, R. L. Porcella, E. C. Etheredge, R. P. Maley, and A. V. Acosta, USGS Open File Report 94-141.
- [Interpretation of Significant Ground-response and Structure Strong Motions Recorded During the 1994 Northridge Earthquake, A. F. Shakal, M. J. Huang, and R. B. Darragh, BSSA, vol. 86, pp. S231-S118, 1996.](#)

- Processed Data Reports

- [Processed CSMIP Strong-Motion Data from the Northridge California earthquake of 17 January 1994: Release No. 1, CGS Publication OSMS 94-06B.](#)
- [Processed CSMIP Strong-Motion Data from the Northridge California earthquake of 17 January 1994: Release No. 2, CGS Publication OSMS 94-08.](#)
- [Processed CSMIP Strong-Motion Data from the Northridge California earthquake of 17 January 1994: Release No. 3, CGS Publication OSMS 94-09.](#)
- [Processed CSMIP Strong-Motion Data from the Northridge California earthquake of 17 January 1994: Release No. 4, CGS Publication OSMS 94-10.](#)
- [Processed Data for Pacoima - Upper Left Abutment from the Northridge Earthquake of 17 January 1994, CGS Publication OSMS 94-12A.](#)
- [Preliminary Processed Data for Tarzana - Cedar Hill Nursery A from the Northridge California Earthquake of 17 January 1994, CGS Publication OSMS 94-12B.](#)
- [Processing of the Upper Left Abutment Record from Pacoima Dam for the Northridge Earthquake, CGS Publication OSMS 94-13.](#)
- [Processed CSMIP Strong-Motion Data from the Northridge California earthquake of 17 January 1994: Release No. 9, CGS Publication OSMS 94-16.](#)
- [Los Angeles Code-Instrumented Building Records from the Northridge, California Earthquake of January 17 1994: Processed Release No. 1, CGS Publication OSMS 94-17.](#)

Figure 13. References for Northridge earthquake available from the “Report” button on the Data Report Page of Northridge earthquake.

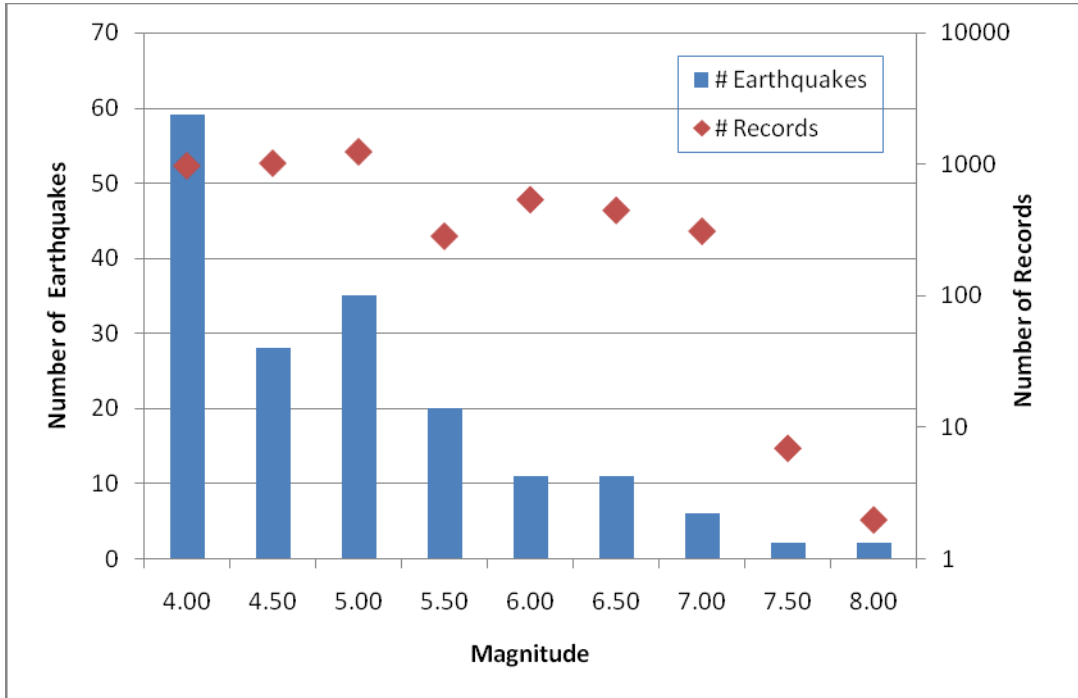


Figure 14: Total number of earthquakes and records in the CESMD database

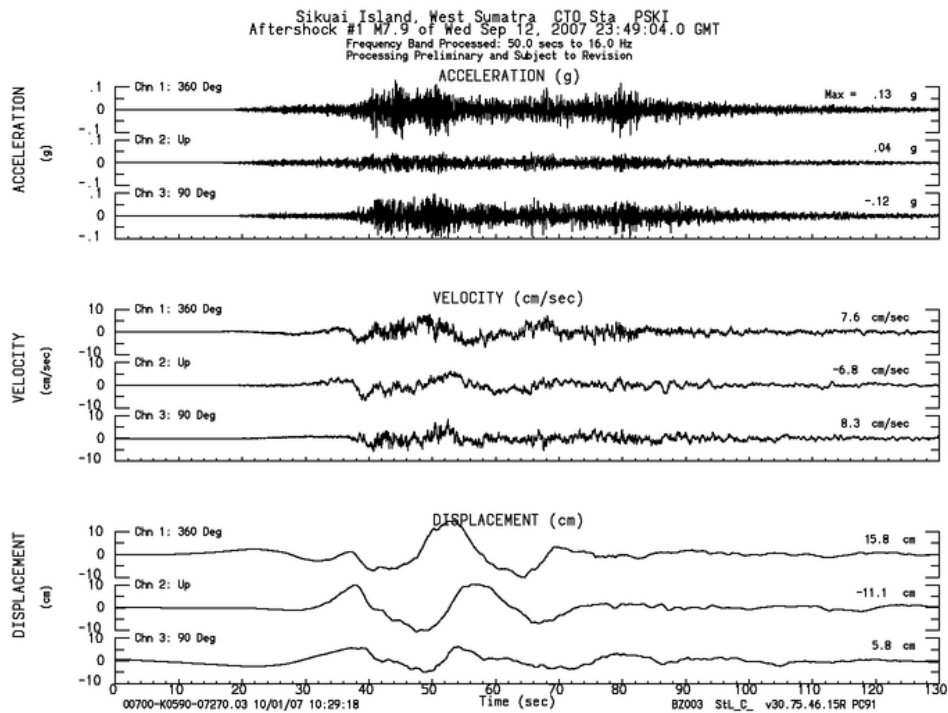


Figure 15. Acceleration, velocity and displacement time histories of the record from M7.9 aftershock of Sumatra earthquake of 12 September 2007 at Caltech Tectonics Observatory (CTO) station PSKI.

Seismic Region	No. of Events	Magnitude	No. Stations
California	53	4.0 - 5.4	1655
Pacific Northwest	1	4.5	14
Inter-Mountain West	3	4.2 – 6.0	31
Mid-America	1	5.2	7
Alaska	1	5.5	15
Hawaii	1	5.0	16
Puerto Rico	1	5.9	2
International	5	5.8 – 8.4	21

Table 1. Update on the records added to the CESMD database since SMIP annual seminar in September 2007.

